

## Characterising Candidate Blazar Counterparts of the Ultra-High-Energy Event KM3-230213A





O. ADRIANI,<sup>1,2</sup> S. AIELLO,<sup>3</sup> A. ALBERT,<sup>4,5</sup> A. R. ALHEBSI,<sup>6</sup> M. ALSHAMSII,<sup>7</sup> S. ALVES GARRE,<sup>8</sup> A. AMBROSONE,<sup>9,10</sup>  
F. AMELI,<sup>11</sup> M. ANDRE,<sup>12</sup> L. APHECETCHE,<sup>13</sup> M. ARDID ,<sup>14</sup> S. ARDID,<sup>14</sup> J. AUBLIN,<sup>15</sup> F. BADARACCO,<sup>16,17</sup>  
L. BAILLY-SALINS,<sup>18</sup> Z. BARDAČOVÁ,<sup>19,20</sup> B. BARET,<sup>15</sup> A. BARIEGO-QUINTANA,<sup>8</sup> Y. BECHERINI,<sup>15</sup> M. BENDAHMAN,<sup>10</sup>  
F. BENFENATI GUALANDI,<sup>21,22</sup> M. BENHASSI,<sup>23,10</sup> M. BENNANI,<sup>18</sup> D. M. BENOIT,<sup>24</sup> E. BERBEE,<sup>25</sup> E. BERTI,<sup>1</sup>  
V. BERTIN,<sup>7</sup> P. BETTI,<sup>1</sup> S. BIAGI,<sup>26</sup> M. BOETTCHER,<sup>27</sup> D. BONANNO,<sup>26</sup> S. BOTTAI,<sup>1</sup> A. B. BOUASLA,<sup>28</sup> J. BOUMAAZA,<sup>29</sup>  
M. BOUTA,<sup>7</sup> M. BOUWHUIS,<sup>25</sup> C. BOZZA,<sup>30,10</sup> R. M. BOZZA,<sup>9,10</sup> H. BRÂNZAŞ,<sup>31</sup> F. BRETAUDEAU,<sup>13</sup> M. BREUHAUS ,<sup>7</sup>  
R. BRUIJN,<sup>32,25</sup> J. BRUNNER,<sup>7</sup> R. BRUNO,<sup>3</sup> E. BUIS,<sup>33,25</sup> R. BUOMPANE,<sup>23,10</sup> S. BUSON,<sup>34,35</sup> J. BUSTO,<sup>7</sup> B. CAIFFI,<sup>16</sup>  
D. CALVO,<sup>8</sup> A. CAPONE,<sup>11,36</sup> F. CARENINI,<sup>21,22</sup> V. CARRETERO,<sup>32,25</sup> T. CARTRAUD,<sup>15</sup> P. CASTALDI,<sup>37,22</sup>  
V. CECCHINI,<sup>8</sup> S. CELLI,<sup>11,36</sup> L. CERISY,<sup>7</sup> M. CHABAB,<sup>38</sup> A. CHEN,<sup>39</sup> S. CHERUBINI,<sup>40,26</sup> T. CHIARUSI,<sup>22</sup>  
M. CIRCELLA,<sup>41</sup> R. CLARK,<sup>42</sup> R. COCIMANO,<sup>26</sup> J. A. B. COELHO,<sup>15</sup> A. COLEIRO,<sup>15</sup> A. CONDORELLI,<sup>15</sup> R. CONIGLIONE,<sup>26</sup>  
P. COYLE,<sup>7</sup> A. CREUSOT,<sup>15</sup> G. CUTTONE,<sup>26</sup> R. DALLIER,<sup>13</sup> A. DE BENEDITTIS,<sup>10</sup> G. DE WASSEIGE,<sup>42</sup> V. DECOENE,<sup>13</sup>  
P. DEGUIRE,<sup>7</sup> I. DEL ROSSO,<sup>21,22</sup> L. S. DI MAURO,<sup>26</sup> I. DI PALMA,<sup>11,36</sup> A. F. DÍAZ,<sup>43</sup> D. DIEGO-TORTOSA,<sup>26</sup>  
C. DISTEFANO,<sup>26</sup> A. DOMI,<sup>44</sup> C. DONZAUD,<sup>15</sup> D. DORNIC,<sup>7</sup> E. DRAKOPOULOU,<sup>45</sup> D. DROUHIN,<sup>4,5</sup> J.-G. DUCCOIN,<sup>7</sup>  
P. DUVERNE,<sup>15</sup> R. DVORNICKÝ,<sup>19</sup> T. EBERL,<sup>44</sup> E. ECKEROVÁ,<sup>19,20</sup> A. EDDYMAOUI,<sup>29</sup> T. VAN EEDEN,<sup>25</sup> M. EFF,<sup>15</sup>  
D. VAN EIJK,<sup>25</sup> I. EL BOJADDAINI,<sup>46</sup> S. EL HEDRI,<sup>15</sup> S. EL MENTAWI,<sup>7</sup> V. ELLAJOSYULA,<sup>16,17</sup> A. ENZENHÖFER,<sup>7</sup>  
G. FERRARA,<sup>40,26</sup> M. D. FILIPOVIĆ,<sup>47</sup> F. FILIPPINI,<sup>22</sup> D. FRANCIOTTI,<sup>26</sup> L. A. FUSCO,<sup>30,10</sup> T. GAL,<sup>44</sup>  
J. GARCÍA MÉNDEZ,<sup>14</sup> A. GARCIA SOTO,<sup>8</sup> C. GATIUS OLIVER,<sup>25</sup> N. GEISSELBRECHT,<sup>44</sup> E. GENTON,<sup>42</sup> H. GHADDARI,<sup>46</sup>  
L. GIALANELLA,<sup>23,10</sup> B. K. GIBSON,<sup>24</sup> E. GIORGIO,<sup>26</sup> I. GOOS,<sup>15</sup> P. GOSWAMI,<sup>15</sup> S. R. GOZZINI,<sup>8</sup> R. GRACIA,<sup>44</sup>  
C. GUIDI,<sup>17,16</sup> B. GUILLON ,<sup>18</sup> M. GUTIÉRREZ,<sup>48</sup> C. HAACK,<sup>44</sup> H. VAN HAREN,<sup>49</sup> A. HEIJBOER,<sup>25</sup> L. HENNIG,<sup>44</sup>  
J. J. HERNÁNDEZ-REY ,<sup>8</sup> A. IDRISI,<sup>26</sup> W. IDRISI IBNSALIH,<sup>10</sup> G. ILLUMINATI,<sup>22</sup> O. JANIK,<sup>44</sup> D. JOLY,<sup>7</sup>  
M. DE JONG,<sup>50,25</sup> P. DE JONG,<sup>32,25</sup> B. J. JUNG,<sup>25</sup> P. KALACZYŃSKI,<sup>51,52</sup> G. KALAITZIDAKIS,<sup>53</sup> J. KEEGANS,<sup>24</sup>  
V. KIKVADZE,<sup>54</sup> G. KISTAURI,<sup>55,54</sup> C. KOPPER,<sup>44</sup> A. KOUCHNER,<sup>56,15</sup> YU. A. KOVALEV ,<sup>57,\*</sup> Y. Y. KOVALEV ,<sup>53</sup>  
L. KRUPA,<sup>20</sup> V. KUEVIAKOE,<sup>25</sup> V. KULIKOVSKIY,<sup>16</sup> R. KVATADZE,<sup>55</sup> M. LABALME,<sup>18</sup> R. LAHMANN,<sup>44</sup> M. LAMOUREUX,<sup>42</sup>  
G. LAROSA,<sup>26</sup> C. LASTORIA,<sup>18</sup> J. LAZAR,<sup>42</sup> A. LAZO,<sup>8</sup> S. LE STUM,<sup>7</sup> G. LEHAUT,<sup>18</sup> V. LEMAÎTRE,<sup>42</sup> E. LEONORA,<sup>3</sup>  
N. LESSING,<sup>8</sup> G. LEVI,<sup>21,22</sup> M. LINCETTO ,<sup>35</sup> M. LINDSEY CLARK,<sup>15</sup> F. LONGHITANO,<sup>3</sup> F. MAGNANI,<sup>7</sup> J. MAJUMDAR,<sup>25</sup>  
L. MALERBA,<sup>16,17</sup> F. MAMEDOV,<sup>20</sup> A. MANFREDA,<sup>10</sup> A. MANOUSAKIS,<sup>58</sup> M. MARCONI,<sup>17,16</sup> A. MARGIOTTA,<sup>21,22</sup>  
A. MARINELLI,<sup>9,10</sup> C. MARKOU,<sup>45</sup> L. MARTIN,<sup>13</sup> M. MASTRODICASA,<sup>36,11</sup> S. MASTROIANNI,<sup>10</sup> J. MAURO,<sup>42</sup>  
K. C. K. MEHTA,<sup>52</sup> A. MESKAR,<sup>59</sup> G. MIELE,<sup>9,10</sup> P. MIGLIOZZI,<sup>10</sup> E. MIGNECO,<sup>26</sup> M. L. MITSOU,<sup>23,10</sup> C. M. MOLLO,<sup>10</sup>  
L. MORALES-GALLEGOS ,<sup>23,10</sup> N. MORI ,<sup>1</sup> A. MOUSSA,<sup>46</sup> I. MOZUN MATEO,<sup>18</sup> R. MULLER,<sup>22</sup> M. R. MUSONE,<sup>23,10</sup>  
M. MUSUMECI,<sup>26</sup> S. NAVAS ,<sup>48</sup> A. NAYERHODA,<sup>41</sup> C. A. NICOLAU,<sup>11</sup> B. NKOSI,<sup>39</sup> B. Ó FEARRAIGH ,<sup>16</sup>  
V. OLIVIERO,<sup>9,10</sup> A. ORLANDO,<sup>26</sup> E. OUKACHA,<sup>15</sup> L. PACINI,<sup>1</sup> D. PAESANI,<sup>26</sup> J. PALACIOS GONZÁLEZ,<sup>8</sup>  
G. PAPALASHVILI,<sup>41,54</sup> P. PAPINI,<sup>1</sup> V. PARISI,<sup>17,16</sup> A. PARMAR,<sup>18</sup> E. J. PASTOR GOMEZ,<sup>8</sup> C. PASTORE,<sup>41</sup> A. M. PĂUN,<sup>31</sup>  
G. E. PÄVÄLAŞ,<sup>31</sup> S. PEÑA MARTÍNEZ,<sup>15</sup> M. PERRIN-TERRIN,<sup>7</sup> V. PESTEL,<sup>18</sup> R. PESTES,<sup>15</sup> M. PETROPALOVA,<sup>20</sup>  
L. PFEIFFER ,<sup>35</sup> P. PIATTELLI,<sup>26</sup> A. PLAVIN ,<sup>53,60</sup> C. POIRÈ,<sup>30,10</sup> V. POPA,<sup>31,†</sup> T. PRADIER,<sup>4</sup> J. PRADO,<sup>8</sup>  
S. PULVIRENTI,<sup>26</sup> C. A. QUIROZ-RANGEL,<sup>14</sup> N. RANDAZZO,<sup>3</sup> A. RATNANI,<sup>61</sup> S. RAZZAQUE,<sup>62</sup> I. C. REA,<sup>10</sup> D. REAL,<sup>8</sup>  
G. RICCOBENE,<sup>26</sup> J. ROBINSON,<sup>27</sup> A. ROMANOV,<sup>17,16,18</sup> E. ROS,<sup>53</sup> A. ŠAINA,<sup>8</sup> F. SALESA GREUS,<sup>8</sup>  
D. F. E. SAMTLEBEN,<sup>50,25</sup> A. SÁNCHEZ LOSA,<sup>8</sup> S. SANFILIPPO ,<sup>26</sup> M. SANGUINETI,<sup>17,16</sup> D. SANTONOCITO,<sup>26</sup>  
P. SAPIENZA,<sup>26</sup> M. SCARINGELLA,<sup>1</sup> M. SCARNERA,<sup>42,15</sup> J. SCHNABEL,<sup>44</sup> J. SCHUMANN,<sup>44</sup> H. M. SCHUTE,<sup>27</sup>  
J. SENECA,<sup>25</sup> N. SENAN,<sup>46</sup> P. A. SEVLE MYHR,<sup>42</sup> I. SGURA,<sup>41</sup> R. SHANIDZE,<sup>54</sup> A. SHARMA,<sup>15</sup> Y. SHITOV,<sup>20</sup>  
F. ŠIMKOVIC,<sup>19</sup> A. SIMONELLI,<sup>10</sup> A. SINOPOULOU,<sup>3</sup> B. SPISSO,<sup>10</sup> M. SPURIO,<sup>21,22</sup> O. STARODUBTSEV,<sup>1</sup>  
D. STAVROPOULOS,<sup>45</sup> I. ŠTEKL,<sup>20</sup> D. STOCCO,<sup>13</sup> M. TAIUTI,<sup>17,16</sup> G. TAKADZE,<sup>54</sup> Y. TAYALATI,<sup>29,61</sup> H. THIERSSEN,<sup>27</sup>  
S. THOUDAM,<sup>6</sup> I. TOSTA E MELO,<sup>3,40</sup> B. TROCME,<sup>15</sup> V. TSOURAPIS,<sup>45</sup> S. V. TROITSKY ,<sup>57,63,\*</sup> E. TZAMARIUDAKI,<sup>45</sup>  
A. UKLEJA,<sup>59,52</sup> A. VACHERET,<sup>18</sup> V. VALSECCHI,<sup>26</sup> V. VAN ELEWYCK,<sup>56,15</sup> G. VANNOYE,<sup>7,16,17</sup> E. VANNUCCIN,<sup>1</sup>  
G. VASILEIADIS,<sup>64</sup> F. VAZQUEZ DE SOLA,<sup>25</sup> A. VEUTRO,<sup>11,36</sup> S. VIOLA,<sup>26</sup> D. VIVOLO,<sup>23,10</sup> A. VAN VLIET,<sup>6</sup>  
E. DE WOLF,<sup>32,25</sup> I. LHENRY-YVON,<sup>15</sup> S. ZAVATARELLI,<sup>16</sup> A. ZEGARELLI,<sup>11,36</sup> D. ZITO,<sup>26</sup> J. D. ZORNOZA,<sup>8</sup> J. ZUÑIGA,<sup>8</sup>  
N. ZYWUCKA,<sup>27</sup>

KM3NET COLLABORATION

Corresponding author: M. Lincetto  
massimiliano.lincetto@uni-wuerzburg.de

Corresponding author: L. Pfeiffer  
leonard.pfeiffer@stud-mail.uni-wuerzburg.de

Corresponding author: A. Plavin  
alexander@plav.in

M. LINCETTO <sup>35</sup> L. PFEIFFER <sup>35</sup> S. BUSON <sup>34, 35</sup> JOSE MARIA SANCHEZ ZABALLA <sup>35</sup> A. AZZOLLINI <sup>35</sup>  
A. BREMER <sup>35</sup>

*MessMapp* GROUP

R. D. BLANDFORD <sup>65</sup> S. BUSON <sup>34, 35</sup> L. PFEIFFER <sup>35</sup>









*Fermi*-LAT COLLABORATION (PROVISIONAL LIST OF AUTHORS)

A. C. S. READHEAD <sup>66</sup> V. PAVLIDOU <sup>67, 68</sup> J. A. ZENSUS <sup>69</sup> M.F. ALLER <sup>70</sup> P. V. DE LA PARRA <sup>71</sup>  
M. HODGES,<sup>66</sup> T. HOVATTA <sup>72, 73</sup> S. KIEHLMANN <sup>68</sup> I. LIODAKIS <sup>68</sup> W. MAX-MOERBECK <sup>74</sup> B. MOLINA <sup>71</sup>  
T. J. PEARSON <sup>66</sup> V. RAVI <sup>66</sup> R.A. REEVES <sup>71</sup> A. SYNANI <sup>67, 68</sup> K. TASSIS <sup>67, 68</sup>

OWENS VALLEY RADIO OBSERVATORY 40-M TELESCOPE GROUP

A. FOISSEAU,<sup>15</sup> A. COLEIRO,<sup>15</sup> F. CANGEMI,<sup>15</sup> D. DORNIC,<sup>7</sup> C. LACHAUD,<sup>15</sup> P. MAGGI,<sup>75</sup> D. GOTZ,<sup>76</sup> L. XIN,<sup>77</sup>  
B. CORDIER,<sup>76</sup> O. GODET,<sup>78</sup> A. GOLDWURM,<sup>79</sup> H. GOTO,<sup>76</sup> X. HAN,<sup>77</sup> N. LEROY,<sup>80</sup> C. PLASSE,<sup>76</sup> Y. QIU,<sup>77</sup>  
J. RODRIGUEZ,<sup>76</sup> J. WANG,<sup>77</sup> J. WEI,<sup>77</sup>

SVOM COLLABORATION

P. BALDINI,<sup>81</sup> J. BUCHNER <sup>81</sup> A. K. ERKENOV,<sup>82, \*</sup> N. GLOBUS <sup>83, 84, 85</sup> A. MERLONI <sup>81</sup> A. PAGGI,<sup>68</sup>  
A. V. POPKOV <sup>86, 57, \*</sup> D. PORQUET <sup>87</sup> M. SALVATO <sup>81</sup> Y. V. SOTNIKOVA <sup>82, 57, 88, \*</sup> P. A. VOITSIK <sup>89</sup>

<sup>1</sup>INFN, Sezione di Firenze, via Sansone 1, Sesto Fiorentino, 50019 Italy

<sup>2</sup>Università di Firenze, Dipartimento di Fisica e Astronomia, via Sansone 1, Sesto Fiorentino, 50019 Italy

<sup>3</sup>INFN, Sezione di Catania, (INFN-CT) Via Santa Sofia 64, Catania, 95123 Italy

<sup>4</sup>Université de Strasbourg, CNRS, IPHC UMR 7178, F-67000 Strasbourg, France

<sup>5</sup>Université de Haute Alsace, rue des Frères Lumière, 68093 Mulhouse Cedex, France

<sup>6</sup>Khalifa University of Science and Technology, Department of Physics, PO Box 127788, Abu Dhabi, United Arab Emirates

<sup>7</sup>Aix Marseille Univ, CNRS/IN2P3, CPPM, Marseille, France

<sup>8</sup>IFIC - Instituto de Física Corpuscular (CSIC - Universitat de València), c/Catedrático José Beltrán, 2, 46980 Paterna, Valencia, Spain

<sup>9</sup>Università di Napoli "Federico II", Dip. Scienze Fisiche "E. Pancini", Complesso Universitario di Monte S. Angelo, Via Cintia ed. G, Napoli, 80126 Italy

<sup>10</sup>INFN, Sezione di Napoli, Complesso Universitario di Monte S. Angelo, Via Cintia ed. G, Napoli, 80126 Italy

<sup>11</sup>INFN, Sezione di Roma, Piazzale Aldo Moro 2, Roma, 00185 Italy

<sup>12</sup>Universitat Politècnica de Catalunya, Laboratori d'Aplicacions Bioacústiques, Centre Tecnològic de Vilanova i la Geltrú, Avda. Rambla Exposició, s/n, Vilanova i la Geltrú, 08800 Spain

<sup>13</sup>Subatech, IMT Atlantique, IN2P3-CNRS, Nantes Université, 4 rue Alfred Kastler - La Chantrerie, Nantes, BP 20722 44307 France

<sup>14</sup>Universitat Politècnica de València, Instituto de Investigación para la Gestión Integrada de las Zonas Costeras, C/ Paranimf, 1, Gandia, 46730 Spain

<sup>15</sup>Université Paris Cité, CNRS, Astroparticule et Cosmologie, F-75013 Paris, France

<sup>16</sup>INFN, Sezione di Genova, Via Dodecaneso 33, Genova, 16146 Italy

<sup>17</sup>Università di Genova, Via Dodecaneso 33, Genova, 16146 Italy

<sup>18</sup>LPC CAEN, Normandie Univ, ENSICAEN, UNICAEN, CNRS/IN2P3, 6 boulevard Maréchal Juin, Caen, 14050 France

<sup>19</sup>Comenius University in Bratislava, Department of Nuclear Physics and Biophysics, Mlynska dolina F1, Bratislava, 842 48 Slovak Republic

<sup>20</sup>Czech Technical University in Prague, Institute of Experimental and Applied Physics, Husova 240/5, Prague, 110 00 Czech Republic

<sup>21</sup>Università di Bologna, Dipartimento di Fisica e Astronomia, v.le C. Bertini-Pichat, 6/2, Bologna, 40127 Italy

<sup>22</sup>INFN, Sezione di Bologna, v.le C. Bertini-Pichat, 6/2, Bologna, 40127 Italy

<sup>23</sup>Università degli Studi della Campania "Luigi Vanvitelli", Dipartimento di Matematica e Fisica, viale Lincoln 5, Caserta, 81100 Italy

<sup>24</sup>E. A. Milne Centre for Astrophysics, University of Hull, Hull, HU6 7RX, United Kingdom

<sup>25</sup>Nikhef, National Institute for Subatomic Physics, PO Box 41882, Amsterdam, 1009 DB Netherlands

<sup>26</sup>INFN, Laboratori Nazionali del Sud, (LNS) Via S. Sofia 62, Catania, 95123 Italy

<sup>27</sup>North-West University, Centre for Space Research, Private Bag X6001, Potchefstroom, 2520 South Africa

<sup>28</sup>Université Badji Mokhtar, Département de Physique, Faculté des Sciences, Laboratoire de Physique des Rayonnements, B. P. 12, Annaba, 23000 Algeria

<sup>29</sup>University Mohammed V in Rabat, Faculty of Sciences, 4 av. Ibn Battouta, B.P. 1014, R.P. 10000 Rabat, Morocco

<sup>30</sup>Università di Salerno e INFN Gruppo Collegato di Salerno, Dipartimento di Fisica, Via Giovanni Paolo II 132, Fisciano, 84084 Italy

<sup>31</sup>Institute of Space Science - INFLPR Subsidiary, 409 Atomistilor Street, Magurele, Ilfov, 077125 Romania

- <sup>32</sup> *University of Amsterdam, Institute of Physics/IHEF, PO Box 94216, Amsterdam, 1090 GE Netherlands*
- <sup>33</sup> *TNO, Technical Sciences, PO Box 155, Delft, 2600 AD Netherlands*
- <sup>34</sup> *Deutsches Elektronen-Synchrotron DESY, Platanenallee 6, 15738 Zeuthen, Germany*
- <sup>35</sup> *Julius-Maximilians-Universität Würzburg, Fakultät für Physik und Astronomie, Institut für Theoretische Physik und Astrophysik, Lehrstuhl für Astronomie, Emil-Fischer-Straße 31, 97074 Würzburg, Germany*
- <sup>36</sup> *Università La Sapienza, Dipartimento di Fisica, Piazzale Aldo Moro 2, Roma, 00185 Italy*
- <sup>37</sup> *Università di Bologna, Dipartimento di Ingegneria dell'Energia Elettrica e dell'Informazione "Guglielmo Marconi", Via dell'Università 50, Cesena, 47521 Italia*
- <sup>38</sup> *Cadi Ayyad University, Physics Department, Faculty of Science Semlalia, Av. My Abdellah, P.O.B. 2390, Marrakech, 40000 Morocco*
- <sup>39</sup> *University of the Witwatersrand, School of Physics, Private Bag 3, Johannesburg, Wits 2050 South Africa*
- <sup>40</sup> *Università di Catania, Dipartimento di Fisica e Astronomia "Ettore Majorana", (INFN-CT) Via Santa Sofia 64, Catania, 95123 Italy*
- <sup>41</sup> *INFN, Sezione di Bari, via Orabona, 4, Bari, 70125 Italy*
- <sup>42</sup> *UCLouvain, Centre for Cosmology, Particle Physics and Phenomenology, Chemin du Cyclotron, 2, Louvain-la-Neuve, 1348 Belgium*
- <sup>43</sup> *University of Granada, Department of Computer Engineering, Automation and Robotics / CITIC, 18071 Granada, Spain*
- <sup>44</sup> *Friedrich-Alexander-Universität Erlangen-Nürnberg (FAU), Erlangen Centre for Astroparticle Physics, Nikolaus-Fiebiger-Straße 2, 91058 Erlangen, Germany*
- <sup>45</sup> *NCSR Demokritos, Institute of Nuclear and Particle Physics, Ag. Paraskevi Attikis, Athens, 15310 Greece*
- <sup>46</sup> *University Mohammed I, Faculty of Sciences, BV Mohammed VI, B.P. 717, R.P. 60000 Oujda, Morocco*
- <sup>47</sup> *Western Sydney University, School of Computing, Engineering and Mathematics, Locked Bag 1797, Penrith, NSW 2751 Australia*
- <sup>48</sup> *University of Granada, Dpto. de Física Teórica y del Cosmos & C.A.F.P.E., 18071 Granada, Spain*
- <sup>49</sup> *NIOZ (Royal Netherlands Institute for Sea Research), PO Box 59, Den Burg, Texel, 1790 AB, the Netherlands*
- <sup>50</sup> *Leiden University, Leiden Institute of Physics, PO Box 9504, Leiden, 2300 RA Netherlands*
- <sup>51</sup> *AstroCeNT, Nicolaus Copernicus Astronomical Center, Polish Academy of Sciences, Rektorska 4, Warsaw, 00-614 Poland*
- <sup>52</sup> *AGH University of Krakow, Al. Mickiewicza 30, 30-059 Krakow, Poland*
- <sup>53</sup> *Max-Planck-Institut für Radioastronomie, Auf dem Hügel 69, 53121 Bonn, Germany*
- <sup>54</sup> *Tbilisi State University, Department of Physics, 3, Chavchavadze Ave., Tbilisi, 0179 Georgia*
- <sup>55</sup> *The University of Georgia, Institute of Physics, Kostava str. 77, Tbilisi, 0171 Georgia*
- <sup>56</sup> *Institut Universitaire de France, 1 rue Descartes, Paris, 75005 France*
- <sup>57</sup> *Institute for Nuclear Research, Russian Academy of Sciences, 60th October Anniversary Prospect 7a, Moscow 117312, Russia*
- <sup>58</sup> *University of Sharjah, Sharjah Academy for Astronomy, Space Sciences, and Technology, University Campus - POB 27272, Sharjah, - United Arab Emirates*
- <sup>59</sup> *National Centre for Nuclear Research, 02-093 Warsaw, Poland*
- <sup>60</sup> *Harvard University, Black Hole Initiative, 20 Garden Street, Cambridge, MA 02138 USA*
- <sup>61</sup> *School of Applied and Engineering Physics, Mohammed VI Polytechnic University, Ben Guerir, 43150, Morocco*
- <sup>62</sup> *University of Johannesburg, Department Physics, PO Box 524, Auckland Park, 2006 South Africa*
- <sup>63</sup> *Lomonosov Moscow State University, 1-2 Leninskie Gory, Moscow 119991, Russia*
- <sup>64</sup> *Laboratoire Univers et Particules de Montpellier, Place Eugène Bataillon - CC 72, Montpellier Cédex 05, 34095 France*
- <sup>65</sup> *Kavli Institute for Particle Astrophysics and Cosmology, Department of Physics, Stanford University, Stanford, CA 94305, USA*
- <sup>66</sup> *Owens Valley Radio Observatory, California Institute of Technology, Pasadena, CA 91125, USA*
- <sup>67</sup> *Department of Physics and Institute of Theoretical and Computational Physics, University of Crete, 71003 Heraklion, Greece*
- <sup>68</sup> *Institute of Astrophysics, Foundation for Research and Technology-Hellas, GR-71110 Heraklion, Greece*
- <sup>69</sup> *Max-Planck-Institut für Radioastronomie, Auf dem Hügel 69, D-53121 Bonn, Germany*
- <sup>70</sup> *Department of Astronomy, University of Michigan, 323 West Hall, 1085 S. University Avenue, Ann Arbor, MI 48109, USA*
- <sup>71</sup> *CePIA, Astronomy Department, Universidad de Concepción, Casilla 160-C, Concepción, Chile*
- <sup>72</sup> *Finnish Centre for Astronomy with ESO (FINCA), University of Turku, FI-20014 University of Turku, Finland*
- <sup>73</sup> *Aalto University Metsähovi Radio Observatory, Metsähovintie 114, 02540 Kylmälä, Finland*
- <sup>74</sup> *Departamento de Astronomía, Universidad de Chile, Camino El Observatorio 1515, Las Condes, Santiago, Chile*
- <sup>75</sup> *Observatoire Astronomique de Strasbourg, Université de Strasbourg, CNRS, 11 rue de l'Université, F-67000 Strasbourg, France*
- <sup>76</sup> *Université Paris-Saclay, Université Paris Cité, CEA, CNRS, AIM, 91191 Gif-sur-Yvette, France*
- <sup>77</sup> *Key Laboratory of Space Astronomy and Technology, National Astronomical Observatories, Chinese Academy of Sciences, Beijing 100101, China*
- <sup>78</sup> *IRAP, Université de Toulouse, CNRS, CNES, UPS, Toulouse, France*
- <sup>79</sup> *Université Paris Cité, CNRS, CEA, Astroparticule et Cosmologie, F-75013 Paris, France*
- <sup>80</sup> *Université Paris-Saclay, CNRS/IN2P3, IJCLab, 91405 Orsay, France*
- <sup>81</sup> *Max-Planck-Institut für extraterrestrische Physik, Giessenbachstrasse 1, 85748 Garching, Germany*
- <sup>82</sup> *Special Astrophysical Observatory of the Russian Academy of Sciences, Nizhny Arkhyz 369167, Russia*
- <sup>83</sup> *Instituto de Astronomía, Universidad Nacional Autónoma de México Campus Ensenada, A.P. 106, Ensenada, BC 22800, México*

<sup>84</sup>*Kavli Institute for Particle Astrophysics and Cosmology, Stanford University, Stanford, CA 94305, USA*

<sup>85</sup>*Astrophysical Big Bang Laboratory, RIKEN, Wako, Saitama, Japan*

<sup>86</sup>*Moscow Center for Advanced Studies, Kulakova str. 20, Moscow, 123592, Russia*

<sup>87</sup>*Aix Marseille Univ, CNRS, CNES, LAM, Marseille, France*

<sup>88</sup>*Kazan Federal University, Institute of Physics, 18 Kremlyovskaya Street, Kazan 420008, Russia*

<sup>89</sup>*Independent researcher*

## ABSTRACT

The KM3NeT experiment reported the detection of an ultra-high-energy neutrino with an energy estimate of  $\sim 220$  PeV, the most energetic yet observed. The neutrino arrival direction has a 99% confidence region of  $3^\circ$  radius centred at RA  $94.3^\circ$ , Dec  $-7.8^\circ$  (J2000). High-energy astrophysical neutrinos are a crucial messenger for understanding hadronic acceleration processes in the Universe and for identifying the origin of ultra-high-energy cosmic rays. Among the most powerful cosmic accelerators, blazars are proposed as promising neutrino sources. A sample of seventeen candidate blazars located in this region is selected through their multiwavelength properties, and studied using archival data and dedicated observations. One of the candidate counterparts exhibits a radio flare coinciding with the neutrino arrival time, with a pre-trial chance probability of 0.26%. Another candidate counterpart exhibits a rising trend in the X-ray flux in a one-year window around the neutrino arrival time. A third candidate undergoes a gamma-ray flare during the same period. While none of these candidates can conclusively be linked to the neutrino, the implications of a possible blazar origin for the KM3NeT event are discussed.

## 1. INTRODUCTION

The detection of an ultra-high-energy (here in the following UHE;  $\sim 50$  PeV – EeV range) neutrino by KM3NeT (Aiello et al. 2025), the deep sea neutrino observatory in the Mediterranean, marks a significant milestone in neutrino astrophysics. This event, far more energetic than any previously observed astrophysical neutrino, challenges the current understanding of the cosmic neutrino spectrum, which exhibits a steep decline at the highest energies (Abbasi et al. 2022). The observation of astrophysical neutrinos in the high-energy range (here in the following HE; TeV – PeV range) and UHE range represents an important progress in unravelling the origins of cosmic rays. As cosmic rays accelerate and propagate through space, they may interact with ambient matter or radiation fields, triggering hadronic processes that produce high-energy neutrinos. These neutrinos serve as unambiguous tracers of cosmic rays acceleration, as their production is exclusively tied to hadronic interactions.

While the detection of an astrophysical diffuse neutrino flux is well established, the nature of the astrophysical sources dominating this emission remains a major open question. Moreover, the detection of KM3-230213A could indicate the existence of a new class of ex-

treme cosmic accelerators, distinct from those responsible for the bulk of the high-energy neutrino flux. It may also represent the first observation of a cosmogenic neutrino (Berezinsky & Zatsepin 1969), produced in interactions between ultra-high-energy cosmic rays (UHECR) and the cosmic radiation background.

With the current angular resolution of neutrino telescopes, the positional coincidence of individual events is in general not sufficient to establish an association with astrophysical counterparts. For this reason, previous research has focused on population studies or variable behaviour of candidate sources, in synergy with multi-wavelength and time-domain astronomical observations, to identify potential associations.

Among the candidate sources of HE and UHE cosmic rays are blazars. Blazars are a subclass of active galactic nuclei (AGN) with highly-collimated jets pointing almost directly towards Earth. They emit across the whole electromagnetic spectrum from radio frequencies to very-high-energy ( $\gtrsim 100$  GeV) gamma rays (Blandford et al. 2019; Böttcher 2019; Jormanainen et al. 2023) and can display strong variability, ranging from minutes to year timescales. The first promising association between a high-energy neutrino event and a blazar was reported in 2017 with the detection of neutrino IceCube-170922A from the direction of the blazar TXS 0506+056, which was flaring in gamma rays (Aartsen et al. 2018). Since then, correlations between blazars and neutrino detections have been examined in many studies. They suggest a potential connection between the extreme

\* The shown author affiliations reflect their job contracts; the KM3NeT collaboration has currently suspended all institutional relations with Russian science organisations.

† Deceased

high-energy processes in or nearby blazars and the production of neutrinos (Krauß et al. 2014; Padovani et al. 2019; Giommi et al. 2020; Franckowiak et al. 2020; Hovatta et al. 2021; Das et al. 2022; Buson et al. 2022, 2023; Plavin et al. 2023; Bellenghi et al. 2023; Abbasi et al. 2023; Garrappa et al. 2024; Kouch et al. 2024; Albert et al. 2024). This evidence supports the hypothesis that blazars play a major role in the production of high-energy cosmic rays and neutrinos. However, definitive proof remains elusive.

Following this motivation, in this paper a possible blazar origin for the KM3NeT event is investigated. The candidate blazar counterparts positionally consistent with KM3-230213A are studied, exploring their multiwavelength and time-domain properties. In [Section 2](#) the properties of the event are briefly presented. In [Section 3](#), the methodology adopted to pinpoint objects of likely blazar nature, found in the region of KM3-230213A, is introduced. Further developing the initial search for counterparts in multiwavelength archival data reported in the previous study (Aiello et al. 2025), a sample of seventeen potential blazar associations in the 99% confidence region of KM3-230213A is presented. The multiwavelength and time-domain properties of the most notable objects are presented in [Section 5](#). Finally in [Section 6](#), the consistency between these observations and the blazar-neutrino association hypothesis is discussed in light of current models of the high-energy emission in blazars. As conclusion, a summary is presented in [Section 7](#).

## 2. THE ULTRA-HIGH-ENERGY EVENT KM3-230213A

The KM3NeT Collaboration is building two large-volume neutrino detectors in the depths of the Mediterranean Sea (Adrian-Martinez et al. 2016; Aiello et al. 2024). The KM3NeT/ORCA detector, located near Toulon (France), will be equipped with 115 detector lines, with a geometry optimised for the detection of GeV-scale neutrinos and the study of atmospheric neutrino oscillations. The KM3NeT/ARCA detector is located near Portopalo di Capo Passero in Sicily (Italy) and will consist of two blocks of 115 detector lines, with larger spacings optimised for TeV–PeV astrophysical neutrinos. Each detection line, anchored on the sea bed, comprises 18 digital optical modules (DOM, Aiello et al. 2022), containing 31 80 mm photomultiplier tubes.

On 2023 February 13, KM3NeT detected an exceptionally high-energy muon, originating most likely in the interaction of a cosmic neutrino. The energy of the detected muon is estimated at  $120_{-60}^{+110}$  PeV. Assuming an

astrophysical  $E^{-2}$  flux, the best fit neutrino energy is  $\sim 220$  PeV with a 90% confidence interval of 72 PeV – 2.6 EeV. The event is designated KM3-230213A (Aiello et al. 2025). This event was detected with the ARCA21 detector configuration (21 active lines). The J2000 equatorial coordinates of KM3-230213A are RA =  $94.3^\circ$ , Dec =  $-7.8^\circ$  ( $06^{\text{h}}17^{\text{m}}12^{\text{s}}, -07^\circ 48' 00''$ ); the UTC date and time of the detection was 2023-02-13T01:16:47.703Z (MJD = 59988.0533299). The directional error region is largely dominated by the current systematic uncertainty in the absolute orientation of the detector. The containment radii for different confidence levels are: R(68%) =  $1.5^\circ$ , R(90%) =  $2.2^\circ$ , and R(99%) =  $3.0^\circ$ . In the near future, a recalibration of the detector elements will provide a significant improvement in the localisation accuracy of KM3-230213A.

## 3. BLAZAR SELECTION

The majority of the electromagnetic emission from blazars is commonly attributed to leptonic processes, such as synchrotron emission of accelerated electrons and inverse Compton scattering. The two processes may be coupled, with emission resulting from a synchrotron self-Compton process. In lepto-hadronic models, accelerated ions interact with photons or protons producing neutral pions, decaying into high-energy gamma rays, and charged pions, decaying into muons and neutrinos (Mannheim & Biermann 1989; Mannheim et al. 1992; Hovatta & Lindfors 2019). Protons can also produce electromagnetic radiation through other means, such as Bethe-Heitler pair production or synchrotron processes. Furthermore, depending on the density of the emission region, gamma rays may cascade down to lower energies, in the MeV and/or X-ray bands. Different electromagnetic signatures can, therefore, be exploited to identify candidate blazar sources.

### 3.1. Methodology

As part of the initial study of KM3-230213A (Aiello et al. 2025), multiwavelength archival data were explored to compile a census of potential blazar companions within the 99% confidence region of the event. In this work, while maintaining the original four selection methods, the sample is expanded from twelve to seventeen candidates thanks to Very Long Baseline Interferometry (VLBI) observations conducted with the Very Long Baseline Array (VLBA) for the purpose of this work (see [Appendix A.1.1](#)). Consistently with the strategy adopted in the initial study, the selection methods are the following:

- Method 1: this strategy relies on the distinctive X-ray, radio and infrared properties of blazars.



By cross matching the first *eROSITA* catalogue (eRASS1; Merloni et al. 2024) with the NRAO VLA Sky Survey catalogue (NVSS, at 1.4 GHz; Condon et al. 1998), eighteen sources with radio fluxes exceeding 10 mJy are identified. The sources are positionally cross-matched with the Wide-field Infrared Survey Explorer (*WISE*; Cutri et al. 2021). The measured *WISE* colours of these objects are used to select those that populate the “*WISE* blazar strip” (Massaro et al. 2012), narrowing the list of likely blazar candidates to seven objects (see Appendix A.2.1). Consistent results are found when cross-matching the eROSITA data set with the DESI Legacy Survey DR10 (Dey et al. 2019) using the Bayesian tool NWay (Salvato et al. 2018) combined with machine learning, as described in Salvato et al. (2022).

- Method 2: radio blazars are selected on the basis of their parsec-scale flux measured by VLBI, as motivated by population studies (Lister et al. 2019) and previous works (e.g. blazars/ANTARES studies; Albert et al. 2024). Following the approach suggested in Plavin et al. (2023), VLBI measurements from the Radio Fundamental Catalog (RFC, version 2024c; Petrov & Kovalev 2025) are used. The catalogue is complete down to a cutoff level of 100 mJy at 8 GHz. Objects above this threshold are selected, resulting in five objects with median VLBI flux density ranging from 0.1 Jy to 2 Jy. In addition to RFC catalogued sources, six objects are pinpointed on the basis of their VLBI properties from the dedicated VLBA observation (see Appendix A.1.1). These are marked with the indication “2a” under “method” in Table 1.
- Method 3: the 5th Roma BZ Catalogue (5BZCAT; Massaro et al. 2015), a compilation of 3561 blazars, has been previously used to investigate the possible neutrino-blazar connection (Aiello et al. 2025; Buson et al. 2022; Buson et al. 2022; Buson et al. 2023). Three objects in this catalogue are located within the 99% confidence region.
- Method 4: The *Fermi*-LAT fourth source catalogue (4FGL-DR4; Ballet et al. 2023) provides the

most recent census of gamma-ray sources in the 50 MeV–1 TeV energy range. Four 4FGL-DR4 objects are found within the 99% confidence region of KM3-230213A.

### 3.2. List of candidate blazar sources

In total, seventeen blazar candidates were pinpointed through the methods described above, with four sources selected through more than one method. The final list of objects is provided in Table 1, which includes their spatial distance from the KM3-230213A best-fit position, redshift (when available), associated electromagnetic counterparts, VLBI radio and X-ray flux measurements. The positions of these sources relative to the KM3-230213A confidence region are shown in Figure 1. With the exception of 4FGL J0616.2-0653 (#2), that is only detected through gamma rays (see also the Appendix A.4.1), all the other sources are detected in radio.

Spectroscopic classifications and redshift determinations are available only for the three sources reported in the 5BZCAT. They are classified as flat spectrum radio quasars (FSRQs) based on the presence of broad emission lines in their optical spectra (Massaro et al. 2015). Object 0605-085 (#6, 5BZQ J0607-0834) is one of the fifty brightest radio blazars in the sky. Observations with the Hobby-Eberley Telescope (HET) detect the  $H\beta$  and Mg II emission lines, enabling a redshift estimate of  $z = 0.870$  (Shaw et al. 2012). PMN J0609-0615 (#7, 5BZQ J0609-0615) is observed with the New Technology Telescope (NTT), revealing a broad C IV emission line corresponding to a redshift of  $z = 2.219$  (Shaw et al. 2012). PMN J0606-0724 (#8, 5BZQ J0606-0724) appears in the Candidate Gamma-Ray Blazar Survey Catalog (CGRaBS, Healey et al. 2008) and has a spectroscopically measured redshift of  $z = 1.227$ .

Some of the candidate sources are recorded in existing catalogues of candidate blazars. A total of three sources is reported in CGRaBS. Three sources appear in WIBRaLS (D’Abrusco et al. 2014), a catalogue of radio-loud candidate gamma-ray emitting blazars selected through the *WISE* mid-infrared colours, with a strategy similar to the blazar strip selection adopted in Method 1 of Section 3. The corresponding identifiers are indicated as associations in Table 1.

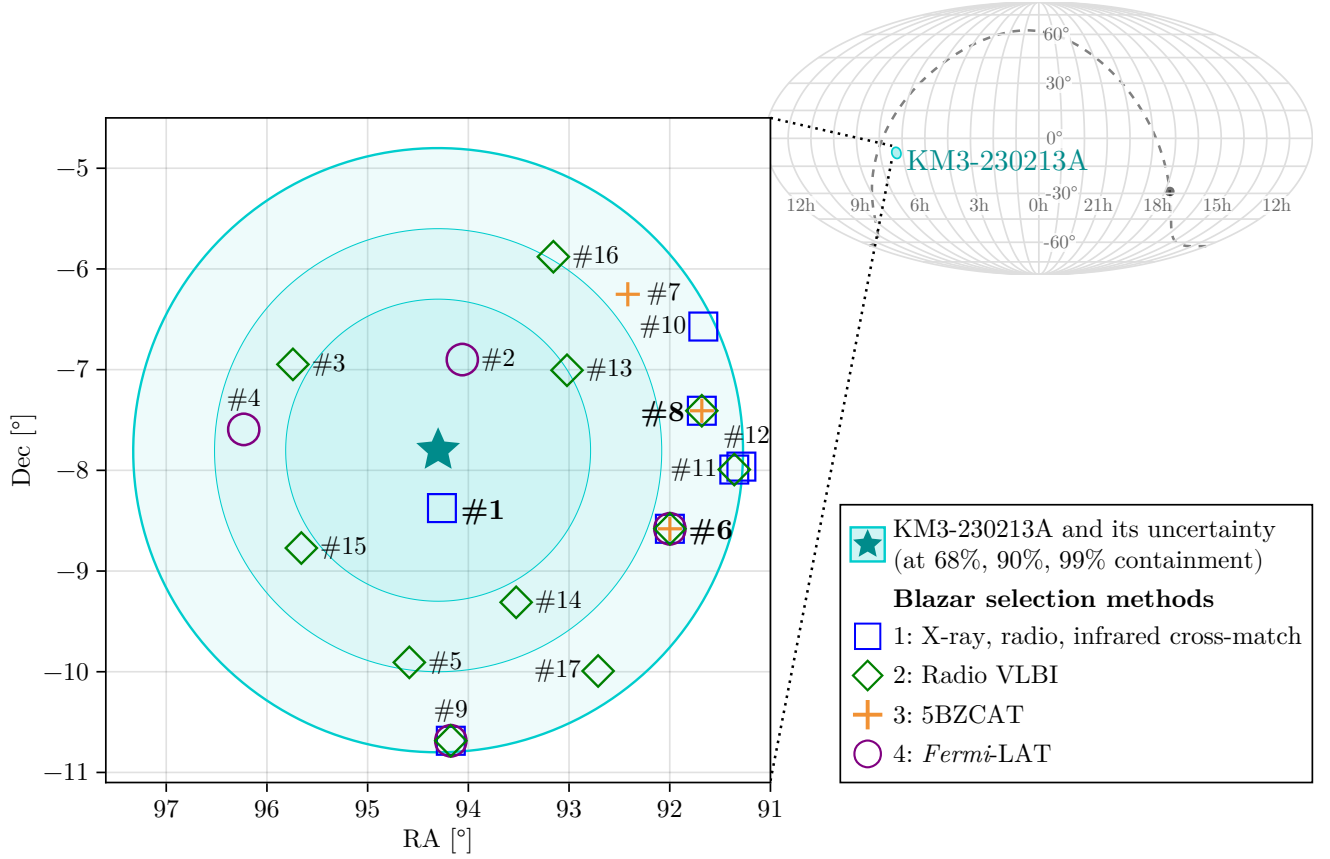


**Figure 1.** Summary of KM3-230213A and its candidate blazar counterparts selected in Section 3. Both the location of the KM3NeT event in equatorial coordinates (J2000) and its uncertainty regions are shown. The markers indicate the criteria used for the inclusion in the list of candidates as presented in Section 3. Source numbers refer to Table 1; the three blazars discussed in Section 6 are labelled in bold here: #1 (MRC 0614-083), #6 (0605-085), #8 (PMN J0606-0724).

**Table 1.** Candidate blazars identified using the methods described in Section 3, located within the 99% confidence region of KM3-230213A.

| Source | Names  | Sep.<br>[°] | RA<br>[°] (J2000) | Dec<br>[°] (J2000) | z | Methods | VLBI<br>mJy | Xray<br>[ $10^{-13} \frac{\text{erg}}{\text{cm}^2 \text{s}}$ ] |
|--------|--|-------------|-------------------|--------------------|---|---------|-------------|--|
|        |  |             |                   |                    |   |         |             |  |
| #1     | <b>MRC 0614-083</b><br>NVSS J061703-082225<br>VLASS1QLCIR J061702.97-082229.2<br>WISE J061702.95-082229.5<br>1eRASS J061702.8-082230<br>WIBRaLS J0617-0822 | 0.6         | 94.2623           | -8.3749            | - | 1       | -           | $5.58_{-0.99}^{+1.16}$<br>(R,e,S)                              |
| #2     | <b>4FGL J0616.2-0653</b>   | 0.9         | 94.06             | -6.90              | - | 4       | -           | $\leq 0.89$<br>(e)   |
| #3     | <b>PMN J0622-0657</b>  | 1.7         | 95.7419           | -6.9478            | - | 2       | $87 \pm 9$  | $0.62_{-0.39}^{+1.48}$   |

Table 1 continued

Table 1 (continued)

| Source | Names                           | Sep. | RA          | Dec         | z     | Methods    | VLBI       | Xray   |
|--------|---------------------------------|------|-------------|-------------|-------|------------|------------|--|
|        |                                 | [°]  | [°] (J2000) | [°] (J2000) |       |            | mJy        | [ $10^{-13} \frac{\text{erg}}{\text{cm}^2 \text{s}}$ ] |
|        | NVSS J062258-065652             |      |             |             |       |            |            | (e)  |
|        | VLASS1QLCIR J062258.04-065651.9 |      |             |             |       |            |            |  |
|        | RFC J0622-0656                  |      |             |             |       |            |            |  |
|        | WISEA J062258.02-065652.0       |      |             |             |       |            |            |  |
|        | eRASSU J062257.8-065654         |      |             |             |       |            |            |  |
| #4     | <b>NVSS J062455-073536</b>      | 1.9  | 96.2306     | -7.5936     | -     | 4          | 50 ± 5     | 0.37 $^{+1.82}_{-0.21}$                                |
|        | VLASS1QLCIR J062455.34-073536.9 |      |             |             |       |            |            | (e)  |
|        | eRASSU J062454.9-073541         |      |             |             |       |            |            |  |
|        | 4FGL J0624.8-0735               |      |             |             |       |            |            |  |
| #5     | <b>PMN J0618-0954</b>           | 2.1  | 94.5861     | -9.9071     | -     | 2          | 100        | ≤ 0.93   |
|        | NVSS J061820-095426             |      |             |             |       |            |            | (e)  |
|        | VLASS1QLCIR J061820.67-095425.3 |      |             |             |       |            |            |  |
|        | RFC J0618-0954                  |      |             |             |       |            |            |  |
| #6     | <b>0605-085</b>                 | 2.4  | 91.9987     | -8.5805     | 0.87  | 1, 2, 3, 4 | 2240 ± 226 | 11.6 $^{+9.25}_{-2.89}$                                |
|        | NVSS J060759-083450             |      |             |             |       |            |            | (R,C,S,e)  |
|        | VLASS1QLCIR J060759.69-083450.3 |      |             |             |       |            |            |  |
|        | RFC J0607-0834                  |      |             |             |       |            |            |  |
|        | WISE J060759.61-083451.6        |      |             |             |       |            |            |  |
|        | 1eRASS J060759.7-083448 (H)     |      |             |             |       |            |            |  |
|        | 4FGL J0608.0-0835               |      |             |             |       |            |            |  |
|        | CGRaBS J0607-0834               |      |             |             |       |            |            |  |
|        | BZQ J0607-0834                  |      |             |             |       |            |            |  |
| #7     | <b>PMN J0609-0615</b>           | 2.4  | 92.41656    | -6.25163    | 2.219 | 3          | 48 ± 5     | ≤ 1.47   |
|        | NVSS J060940-061505             |      |             |             |       |            |            | (e)  |
|        | VLASS1QLCIR J060939.98-061505.6 |      |             |             |       |            |            |  |
|        | RFC J0609-0615                  |      |             |             |       |            |            |  |
|        | WISEA J060939.96-061506.0       |      |             |             |       |            |            |  |
|        | BZQ J0609-0615                  |      |             |             |       |            |            |  |
| #8     | <b>PMN J0606-0724</b>           | 2.6  | 91.68144    | -7.40840    | 1.277 | 1, 2, 3    | 306 ± 31   | 0.09 $^{+0.53}_{-0.06}$                                |
|        | NVSS J060643-072430             |      |             |             |       |            |            | (e)  |
|        | VLASS1QLCIR J060643.54-072430.3 |      |             |             |       |            |            |  |
|        | RFC J0606-0724                  |      |             |             |       |            |            |  |
|        | WISEA J060643.53-072430.1       |      |             |             |       |            |            |  |
|        | 1eRASS J060643.3-072429         |      |             |             |       |            |            |  |
|        | CGRaBS J0606-0724               |      |             |             |       |            |            |  |
|        | BZQ J0606-0724                  |      |             |             |       |            |            |  |
| #9     | <b>PMN J0616-1040</b>           | 2.9  | 94.17420    | -10.68568   | -     | 1, 2, 4    | 248 ± 25   | 2.82 $^{+1.5}_{-0.89}$                                 |
|        | NVSS J061641-104108             |      |             |             |       |            |            | (e)  |
|        | VLASS1QLCIR J061641.80-104108.5 |      |             |             |       |            |            |  |
|        | RFC J0616-1041                  |      |             |             |       |            |            |  |

Table 1 continued



Table 1 (continued)

| Source | Names                           | Sep.<br>[°] | RA<br>[°] (J2000) | Dec<br>[°] (J2000) | z | Methods | VLBI<br>mJy  | Xray<br>[ $10^{-13} \frac{\text{erg}}{\text{cm}^2\text{s}}$ ] |
|--------|---------------------------------|-------------|-------------------|--------------------|---|---------|--------------|---|
|        | WISE J061641.80-104108.4        |             |                   |                    |   |         |              |   |
|        | 1eRASS J061641.5-104107         |             |                   |                    |   |         |              |   |
|        | 4FGL J0616.7-1049               |             |                   |                    |   |         |              |   |
|        | CGRaBS J0616-1041               |             |                   |                    |   |         |              |   |
|        | WIBRaLS J061641.80-104108.4     |             |                   |                    |   |         |              |   |
| #10    | <b>NVSS J060639-063421</b>      | 2.9         | 91.6667           | -6.5721            | – | 1       | –            | $0.23_{-0.09}^{+0.65}$  |
|        | VLASS1QLCIR J060640.01-063419.3 |             |                   |                    |   |         |              | (R, e)  |
|        | WISEA J060640.00-063419.6       |             |                   |                    |   |         |              |   |
|        | 1eRASS J060640.2-063424         |             |                   |                    |   |         |              |   |
| #11    | <b>PMN J0605-0759</b>           | 2.9         | 91.35911          | -7.99216           | – | 1, 2a   | $67 \pm 7$   | $1.99_{-0.67}^{+1.04}$  |
|        | NVSS J060526-075928             |             |                   |                    |   |         |              | (e)   |
|        | VLASS1QLCIR J060526.19-075931.9 |             |                   |                    |   |         |              |   |
|        | RFC J0605-0759                  |             |                   |                    |   |         |              |   |
|        | WISE J060526.16-075931.7        |             |                   |                    |   |         |              |   |
|        | 1eRASS J060527.0-075925         |             |                   |                    |   |         |              |   |
|        | WIBRaLS J0605-0759              |             |                   |                    |   |         |              |   |
| #12    | <b>NVSS J060509-075747</b>      | 3.0         | 91.28843          | -7.96308           | – | 1       | –            | $1.93_{-0.88}^{+1.94}$  |
|        | VLASS1QLCIR J060508.92-075747.4 |             |                   |                    |   |         |              | (e)   |
|        | WISEA J060509.22-075747.1       |             |                   |                    |   |         |              |   |
|        | 1eRASS J060509.0-075739         |             |                   |                    |   |         |              |   |
| #13    | <b>PMN J0612-0700</b>           | 1.5         | 93.02018          | -7.00635           | – | 2a      | $62 \pm 7$   | $\leq 0.98$   |
|        | NVSS J061204-070022             |             |                   |                    |   |         |              | (e)   |
|        | VLASS1QLCIR J061204.84-070022.8 |             |                   |                    |   |         |              |   |
|        | eRASSU J930117.21-070019        |             |                   |                    |   |         |              |   |
| #14    | <b>PMN J0614-0918</b>           | 1.7         | 93.52517          | -9.31053           | – | 2a      | $55 \pm 6$   | $\leq 0.85$   |
|        | NVSS J061406-091837             |             |                   |                    |   |         |              | (e)   |
|        | VLASS1QLCIR J061406.04-091837.8 |             |                   |                    |   |         |              |   |
|        | RFC J0614-0918                  |             |                   |                    |   |         |              |   |
| #15    | <b>PMN J0622-0846</b>           | 1.7         | 95.65833          | -8.77174           | – | 2a      | $109 \pm 12$ | $\leq 1.13$   |
|        | NVSS J062237-084617             |             |                   |                    |   |         |              | (e)   |
|        | VLASS1QLCIR J062238.00-084618.2 |             |                   |                    |   |         |              |   |
|        | RFC J0622-0846                  |             |                   |                    |   |         |              |   |
| #16    | <b>NVSS J061237-055244</b>      | 2.2         | 93.15567          | -5.87900           | – | 2a      | $45 \pm 5$   | $\leq 1.17$   |
|        | VLASS1QLCIR J061237.35-055244.4 |             |                   |                    |   |         |              | (e)   |
|        | RFC J0612-0552                  |             |                   |                    |   |         |              |   |
|        | SSTSL2 J061237.36-055244.4      |             |                   |                    |   |         |              |   |
| #17    | <b>NVSS J061050-095934</b>      | 2.7         | 92.71130          | -9.99277           | – | 2a      | $94 \pm 10$  | $0.19_{-0.09}^{+0.75}$  |
|        | VLASS1QLCIR J061050.71-095933.8 |             |                   |                    |   |         |              | (e)   |
|        | RFC J0610-0959                  |             |                   |                    |   |         |              |   |
|        | WISEA J061050.70-095933.8       |             |                   |                    |   |         |              |   |

Table 1 continued

**Table 1** (*continued*)

| Source                  | Names | Sep. | RA          | Dec         | z | Methods | VLBI | Xray   |
|-------------------------|-------|------|-------------|-------------|---|---------|------|--|
|                         |       | [°]  | [°] (J2000) | [°] (J2000) |   |         | mJy  | [ $10^{-13} \frac{\text{erg}}{\text{cm}^2 \text{s}}$ ] |
| eRASSU J061051.1-095936 |       |      |             |             |   |         |      |  |

NOTE—Positions are provided in equatorial (J2000) coordinates, with the primary name (in bold) of each source corresponding to either a common name or the name in the first survey reporting the object. Associated sources across different wavelengths are reported, emphasising the surveys and catalogues relevant to each selection method. For completeness, the counterparts from catalogues considered in this work are indicated regardless of the selection method. The listed coordinates prioritize counterparts in the following order: Radio Fundamental Catalog (VLBI), infrared surveys, VLASS, and *Fermi*-LAT analysis for the single gamma-ray-only detection. In the Methods column the selection methods are reported (see Section 3): 1 (X-ray, radio, infrared crossmatch), 2 (VLBI from RFC), 2a (VLBI from VLBA observation), 3 (5BZCAT), 4 (4FGL). Radio fluxes (8 GHz) and intrinsic, time-averaged X-ray fluxes in the (0.2 – 2.3) keV band are reported in the respective columns. The X-ray instruments from which the average has been calculated are indicated with a single letter: R (*ROSAT*), e (*eROSITA*), S (*Swift*-XRT), C (*Chandra*). Details on the data origin are provided in Appendix A.1.1 and Appendix A.3. For one object, not detected by WISE, the infrared association in the Spitzer (SEIP) source list (SSTSL2; Spitzer Science Center (SSC) & Infrared Science Archive (IRSA) (2021)) is reported.

#### 4. OBSERVATIONAL DATA SUMMARY

Electromagnetic archival data and multiwavelength observations carried out for the purpose of this work on the seventeen candidate blazars are assembled and investigated. The data collection, reduction and analysis are discussed in Appendix A.

*Radio*—VLBI archival data, complemented by dedicated VLBA observations performed in November 2024 for the purpose of this work, are used to probe the parsec-scale structure of candidate sources (Appendix A.1.1). The time-dependent flare study is based on light curves at 15 GHz obtained from the Owens Valley Radio Observatory (OVRO; Richards et al. 2011) and RATAN-600 observational campaigns (Appendix A.1.2, Appendix A.1.3). The calibrator source catalogue of the Atacama Large Millimeter/submillimeter Array (ALMA<sup>1</sup>) is used for complementary variability information.

*Infrared and optical*—Infrared observations are retrieved from archival data of the *WISE* (Wright et al. 2010) and the Near-Earth Object Wide-field Infrared Survey Explorer (*NEOWISE*; Mainzer et al. 2011) programs. Archival optical data are collected from the Asteroid Terrestrial-impact Last Alert System (ATLAS; Tonry et al. 2018; Smith et al. 2020; Heinze et al. 2018), the Catalina Real-Time Transient Survey (CRTS; Drake et al. 2009), the Zwicky Transient Facility (ZTF Masci et al. 2018) ground-based telescopes and the space-based

*Gaia* mission (Gaia Collaboration et al. 2016, 2023; Babusiaux et al. 2023). See Appendix A.2.

*X-rays*—Public archival data are retrieved from the *Neil Gehrels Swift Observatory* (*Swift*; Burrows et al. 2005), the *Chandra X-ray Observatory* (*Chandra*; Weiskopf et al. 2000), and the *ROentgen SATellite* (*ROSAT*; Chlebowski et al. 1991). Proprietary data from the *eROSITA* instrument onboard of the Spektrum-Roentgen-Gamma Observatory (SRG; Predehl et al. 2021) are used. For the two X-ray brightest sources in the sample, target of opportunity (ToO) observations are conducted with *Swift* in December 2024. The 90% error region of KM3-230213A is observed with the MXT and ECLAIR instruments onboard the *Space Variable Objects Monitor* (*SVOM*; Wei et al. 2016). The X-ray observations are presented in Section 5.3 and Appendix A.3.

*Gamma rays*—Continuous observations in the 0.1 – 1000 GeV range from the Large Area Telescope onboard the *Fermi Gamma-ray Space Telescope* are utilised (*Fermi*-LAT; Atwood et al. 2009). See Appendix A.4.

#### 5. MULTIWAVELENGTH PROPERTIES OF KM3-230213A CANDIDATE COUNTERPARTS

The multiwavelength investigation reported in the following has two main goals. First, to characterise the electromagnetic properties of the seventeen candidate counterparts. Second, to reduce the degeneracy in the potential associations by exploiting multiwavelength and time-domain information. The sample of candidate counterparts does not provide compelling evidence for a specific association due to the number of blazars within the 3° footprint. Brightness, spectrum, and time variability information are used to identify additional ob-

<sup>1</sup> <https://almascience.nrao.edu/alma-data/calibrator-catalogue>

servational signatures that can reasonably be expected from a powerful neutrino source.

The  $3^\circ$  radius localisation region of KM3-230213A contains seventeen astronomical sources that are likely blazars (Section 3). Ten of them show strong radio emission on the parsec and sub-parsec scales (Table 2), indicating strong jet beaming effects.

In addition, the temporal correlation between major flares and the neutrino arrival time has been analysed as a key observable that can help selecting source associations. This observational approach was used in earlier studies, comparing radio flares with neutrino detections from IceCube, ANTARES, and Baikal-GVD (Aartsen et al. 2018; Plavin et al. 2020; Hovatta et al. 2021; Albert et al. 2024; Kouch et al. 2024; Allakhverdyan et al. 2024). There is growing evidence for neutrinos being produced during large electromagnetic flares.

The most important results of the multiwavelength variability study are discussed in the following. While not unequivocal proof, highly variable electromagnetic emission could indicate a higher probability that the neutrino is associated to a specific source. In the following, three sources exhibiting flaring behaviour are examined. Their properties in the electromagnetic band involved are summarised in Figure 2.

#### 5.1. Source 0605-085: brightest in radio, experiences gamma-ray flaring activity

Four known *Fermi*-LAT catalogued objects lie within the 90% confidence region of KM3-230213A. Among these, 0605-085 (#6) exhibits gamma-ray enhanced activity during the time of the detection of KM3-230213A (see Figure 2a). The observed year-long flux enhancement exhibits a gradual increase and decrease in emission. Gamma-ray flaring activity has been previously used to pinpoint promising neutrino counterparts (Aartsen et al. 2018), but it may be not unusual for such trends to coincide with a neutrino event by chance.

The blazar 0605-085 is among the fifty brightest radio objects in the whole sky in terms of the VLBI flux density, indicating a high degree of relativistic beaming. The object’s X-ray activity remains unconstrained due to a sparse observational coverage (see also Appendix A.3). The recent *Swift*-XRT ToO observation measured a flux consistent with historical values. At optical wavelengths, a high flux state is observed, temporally consistent with the gamma-ray flare. However, this has to be interpreted with caution, since the blazar is about  $4''$  away from a foreground star. Although the optical light curve for this blazar was constructed using data from ZTF and *Gaia*, which provide sufficient resolution to disentangle point sources separated by such distances,

the possibility of residual contamination from the star affecting the optical light curve of the blazar should be further investigated.

#### 5.2. Major radio flare from PMN J0606-0724

Among the seventeen candidate blazars there are three radio-bright sources in the OVRO CGRaBS sample with dense uniform radio light curves (OVRO + RATAN; Appendix Fig. A4). One of them, PMN J0606-0724 (#8), experiences a large radio flare very close in time to the KM3-230213A event, with a time difference of five days, see Figure 2b.

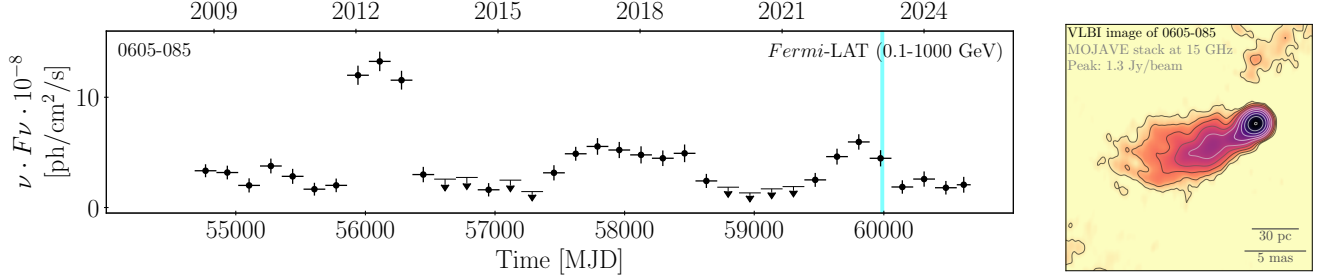
Such a coincidence is relatively uncommon. Thanks to the coverage of monitoring programs at OVRO and RATAN, a statistical evaluation of its chance probability is possible. The analysis is performed in Appendix B, and results in a pre-trial p-value of  $p = 0.26\%$ . This finding can be considered a hint of a possible association, consistent with a number of studies that find such associations in blazars (Plavin et al. 2020; Albert et al. 2024; Hovatta et al. 2021; Kouch et al. 2024; Abbasi et al. 2023). Given the a posteriori nature of this analysis, the exact probability should be interpreted with caution, as discussed in Section 6. This concerns the observed time delay of the radio peak coming five days after the neutrino arrival as well.

Another source, PMN J0616-1040, shows a persistent rapid radio variability in Appendix Fig. A14, indicative of a very compact ( $\sim 10 \mu\text{as}$ ) and bright structure probed by scattering of radio waves (Koay et al. 2019).

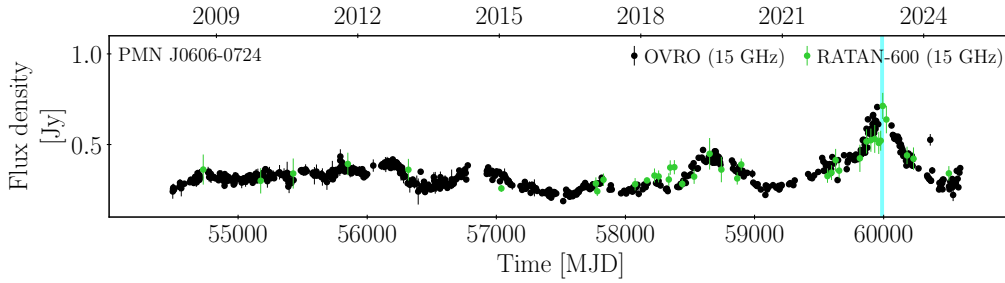
#### 5.3. X-ray flaring activity of MRC 0614-083

The X-ray band represents a valuable tracer of neutrino production in both jetted and non-jetted AGN. Previous studies have proposed an observable connection between neutrinos and X-ray emission in uniform samples of blazars and in individual sources such as TXS 0506+056 and NGC 1068 (Paliya et al. 2020; Plavin et al. 2024; Abbasi et al. 2024; Kun et al. 2024). Likewise, the potential of the X-ray band in revealing hadronic components in the SED of blazars, has been previously shown in the study of the blazar 5BZB J0630-2406 (Fichet de Clairfontaine et al. 2023; Sanchez Zabalza et al. 2025).

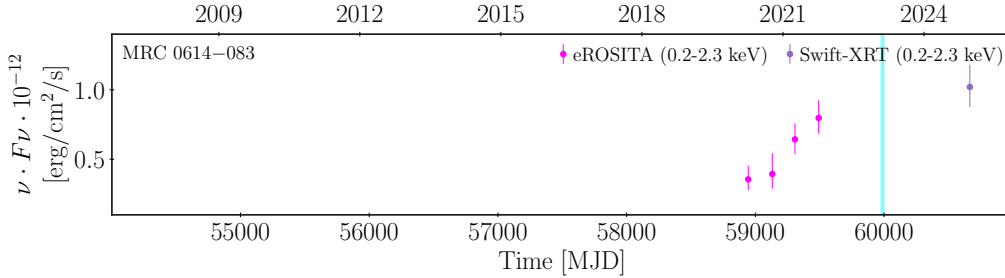
Of the seventeen objects listed in Table 1, nine are detected at X-ray energies. The X-ray fluxes are integrated in the  $0.2 - 2.3$  keV energy band, so that measurements across different facilities can be readily comparable in the light curves. The *eROSITA* observations consist of four epochs in the period MJD 58677–59500 ( $\sim 2$  years). Upon inspection of the *eROSITA* X-ray data for the candidate counterparts, only two objects are found to



(a) The *Fermi*-LAT light curve and a VLBI image of 0605-085: the brightest radio source in the neutrino localisation region that experiences a gamma-ray flaring activity around the neutrino arrival (Section 5.1).



(b) The radio light curve for PMN J0606-0724 that experiences a major flare in close coincidence to the neutrino arrival (Section 5.2).



(c) The X-ray light curve for MRC 0614-083 that indicates a flaring activity around the neutrino arrival (Section 5.3).

**Figure 2.** Summary of observational properties related to the three most promising blazars associated with the KM3-230213A event. The cyan line highlights the arrival time of KM3-230213A in each light curve.

The astronomical coordinates of these blazars are given in Table 1 and shown in Figure 1. Details on the observational data, along with multiwavelength light curves, are reported in Appendix A and Appendix C.

be variable: MRC 0614-083 (#1) and PMN J0616-1040 (#9). In addition, archival *Swift*-XRT observations suggest variability for 0605-085 (#6).

ToO observations with *Swift*-XRT are performed for object #1 and #6, on MJD 60666 and MJD 60669, respectively. The primary goal is to investigate X-ray year-long variability, albeit in a coarse manner, since nearly two years have passed since the observation of KM3-230213A. The choice of the timescale is dictated, in this case, by data availability.

Object #6 and object #9 show no remarkable flux trends in X-ray energies. MRC 0614-083 (#1), which is

the closest to the best fit neutrino localisation, displays X-ray activity that increases steadily in the years leading up to the KM3NeT event (see Figure 2c). The recent *Swift* follow-up indicates that the high X-ray state of the object persists. This suggests the intriguing possibility that KM3-230213A occurs while the object is undergoing an X-ray enhancement. However, the sparse *eROSITA* sample only extends to  $\sim 488$  days before KM3-230213A, leaving a  $\sim 3.2$  year gap between it and the *Swift*-XRT observation.

## 6. DISCUSSION

Due to the size of the neutrino direction uncertainty region, comprising seventeen candidate blazars, it is not possible to conclusively associate the neutrino with a specific source. The temporal correlations reported in Section 5 could arise by chance as well.

Among the examined temporal correlations, only the chance probability for the major radio flare in PMN J0606-0724 is quantifiable in a robust way (Section 5.2). The observed close coincidence of such a flare with the neutrino (within five days) can arise by chance with the probability of  $p = 0.26\%$ . This correlation can be considered a hint of a possible association, especially in light of earlier studies on the blazar flare-neutrino connection. Flaring activity at gamma-ray and X-ray bands is observed in 0605-08 and MRC 0614-083 respectively; these coincidences are more common by chance, and their probabilities are not quantified here. Considering the a posteriori nature of the flare investigation, and the look-elsewhere effect arising from the exploration of time variability across multiple wavelengths, the p-value for the radio flare is interpreted as pre-trial. It serves the purpose of demonstrating that such a close coincidence by chance is rare, but far from impossible. These findings are not claimed as a statistically significant association

The three cases of flaring sources discussed above do not exhibit strong and unequivocal correlations across different electromagnetic bands. However, if the neutrino was associated to one of such flares, the lack of correlated activity in other wavelengths would still be consistent with previous findings. As introduced in Section 3, the multiwavelength signatures of hadronic processes in blazars can be diverse. In the case of TXS 0506+056, while a single neutrino above 100 TeV was detected in the direction of the source while it was flaring in gamma rays, an additional neutrino excess at lower energies was observed during a gamma quiet state (Aartsen et al. 2018; Garrappa et al. 2019). Theoretical efforts have addressed neutrino production under both flaring and non-flaring gamma-ray states (Padovani et al. 2019; Winter et al. 2020; Petropoulou et al. 2020).

From a phenomenological standpoint, the conditions required for a blazar to be the source of a muon neutrino with energy  $E_\nu \sim 100 E_{17} \text{ PeV}$  with  $0.72 \lesssim E_{17} \lesssim 26$  can be evaluated. These neutrinos originate in the collisions of ultrarelativistic ions with protons at rest, or photons of sufficient energy. In both cases, the minimum energy required for a single proton is  $E_p \sim 20E_\nu \gtrsim 1.5 \text{ EeV}$  (Roulet & Vissani 2021). Such an energy is still significantly lower than the highest energies observed for cosmic-ray particles,  $\sim 300 \text{ EeV}$  (Bird et al. 1995; Tele-

scope Array Collaboration et al. 2023), for which AGN jets have already been proposed as possible sources. Assuming a neutrino of this energy is observed from a single source with a rate of  $T^{-1}$ , the luminosity and the minimum jet power can be estimated. The effective area of ARCA with 21 lines at the most likely neutrino energy  $E_\nu \simeq 220 \text{ PeV}$  is  $A_{\text{eff}} \sim 400 \text{ m}^2$  (Aiello et al. 2025). The likely counterparts with known redshift are located at  $z \approx 1$  (Table 1; luminosity distance  $d_L \approx 7 \text{ Gpc}$ ), and these distances are also expected for neutrino associations from pure volume arguments. The emission can be enhanced with beaming effects by  $f_{\text{beam}}$  — the beaming factor. For example,  $f_{\text{beam}} = 1$  for isotropic emission and  $f_{\text{beam}} \approx 10^3$  when the emission is concentrated within  $4^\circ$  around the jet direction. The latter is not atypical for electromagnetic emission (Lister et al. 2019). Together, this implies the source luminosity of

$$L_\nu = \frac{E_\nu \cdot 4\pi d_L^2}{A \cdot T \cdot f_{\text{beam}}} \approx \frac{1.5 \cdot 10^{49} \text{ erg s}^{-1}}{\frac{T}{\text{yr}} \cdot f_{\text{beam}}}. \quad (1)$$

The required power of the jet is at least

$$L_p = 20L_\nu \approx \frac{3 \cdot 10^{50} \text{ erg s}^{-1}}{\frac{T}{\text{yr}} \cdot f_{\text{beam}}}. \quad (2)$$

In general, from the detection of a single event, it is not possible to estimate an event rate, hence the value of  $T$  is not observationally known. Conversely, the maximum rate feasible with the power available in blazar jets can be estimated. Bright blazars are typically associated with the total jet power of  $\sim 10^{45} \text{ erg/s}$ . Assuming  $f_{\text{beam}} = 10^3$ , the required  $L_p$  reaches this value for  $T = 300 \text{ yr}$ . For less pronounced beaming, the minimal  $T$  estimate would be even higher. Note that  $L_p$  here is the bare minimum required power. It only accounts for protons with this specific energy, ignoring the contribution of the remaining spectrum. Furthermore, not every proton at these energy produces a neutrino, as the efficiency depends on the target photon or proton field density. If more neutrinos with these energies are detected from a single source in a time frame of a years or decades, even the minimum power requirements would exceed those normally associated with blazars.

Alternatively, such neutrinos can come from many individual sources over the sky; these sources are likely to be at redshift  $z \sim 1$  by the same volume arguments. The proton luminosity density associated with them can be approximately estimated as

$\mathcal{L}_p \sim 2 \cdot 10^{39} \text{ erg s}^{-1} \text{ Mpc}^{-3} \tau^{-1} (\text{yr})$  where  $\tau^{-1}$  is the total detection rate of neutrinos with these energies at KM3NeT. A single detection within the first years of operation indicates that such events are possible



but rare; assuming  $\tau$  is on the order of decades,  $\mathcal{L}_p \sim 6 \cdot 10^{37} \text{erg s}^{-1} \text{Mpc}^{-3} \sim 10^4 L_\odot \text{Mpc}^{-3}$ . This estimate constitutes a fraction of a percent of the total AGN luminosity density, consistent with blazars being the sources of UHE neutrinos.

Another consideration is whether a blazar can accelerate particles to such high energies at all. A generic argument can be used to place another lower bound on the jet power required to accelerate a proton to an energy  $E_p$  (Blandford 2000, Globus & Blandford, ARAA submitted). Before creating the neutrino, the proton must have traversed a potential difference  $\gtrsim E_p/q = E_p (\text{eV})^{-1} \text{V}$  where  $q$  is its charge. In most models of acceleration, the effective impedance  $Z$  is a fraction of the impedance of vacuum, or  $Z \sim 30\Omega$ . This implies a minimum power requirement of  $L_{\text{jet}} > (E_p/q)^2 Z^{-1}$ ; for the neutrino energy in the hundreds of PeV, the requirement is  $L_{\text{jet}} > 10^{42} \text{erg s}^{-1}$ . Accelerating a small number of protons that can produce UHE neutrinos is not as challenging as accelerating to the highest energy,  $\sim 300 \text{EeV}$  cosmic rays observed.

## 7. SUMMARY

In this paper, a study of blazar candidates as possible associations of the KM3NeT event KM3-230213A (Aiello et al. 2025) is presented. In total, seventeen sources are found within the 99% uncertainty region. Among them, the three most interesting candidates are highlighted in Figure 1 and Figure 2:

1. Object MRC 0614-083 is the closest object, located  $0.6^\circ$  away from the best-fit neutrino position. An indication of an X-ray flare can be noted.
2. Object 0605-085 is one of the fifty brightest blazars on the sky on parsec scales. A long-term gamma-ray flare peaking before the neutrino arrival is observed.
3. Object PMN J0606-0724 has presented the major radio flare, which peaks at 15 GHz within 5 days from the neutrino arrival time. The pre-trial chance coincidence p-value is estimated to be 0.26%.

Based on the findings of this study, the KM3NeT event KM3-230213A can not be conclusively associated with an episode of enhanced multiwavelength emission from a blazar. The hypothesis that the KM3NeT event originates from a blazar is still viable, with several blazar-like catalogued objects reported as potential counterparts in the neutrino field. Additionally, there remains the possibility that the event could be associated with a population of faint and/or remote sources, which are not

individually resolved. Improvements in the calibration of the KM3NeT telescope are expected to decrease the systematic uncertainties in the directional reconstruction of KM3-230213A, thus reducing the degeneracy in the identification of possible counterparts.

## ACKNOWLEDGEMENTS

The authors thank A. Dominguez, G. Principe for reviewing the manuscript within the Fermi-LAT collaboration. This work was supported by the European Research Council, ERC Starting grant *MessMapp*, S.B. Principal Investigator, under contract no. 949555. This work is part of the MuSES project which has received funding from the European Research Council (ERC) under the European Union's Horizon 2020 Research and Innovation Programme (grant agreement No 101142396). The authors acknowledge the financial support of: KM3NeT-INFRADEV2 project, funded by the European Union Horizon Europe Research and Innovation Programme under grant agreement No 101079679; Funds for Scientific Research (FRS-FNRS), Francqui foundation, BAEF foundation. Czech Science Foundation (GAČR 24-12702S); Agence Nationale de la Recherche (contract ANR-15-CE31-0020), Centre National de la Recherche Scientifique (CNRS), Commission Européenne (FEDER fund and Marie Curie Program), LabEx UnivEarthS (ANR-10-LABX-0023 and ANR-18-IDEX-0001), Paris Île-de-France Region, Normandy Region (Alpha, Blue-waves and Neptune), France, The Provence-Alpes-Côte d'Azur Delegation for Research and Innovation (DRARI), the Provence-Alpes-Côte d'Azur region, the Bouches-du-Rhône Departmental Council, the Metropolis of Aix-Marseille Provence and the City of Marseille through the CPER 2021-2027 NEUMED project, The CNRS Institut National de Physique Nucléaire et de Physique des Particules (IN2P3); Shota Rustaveli National Science Foundation of Georgia (SRNSFG, FR-22-13708), Georgia;

The General Secretariat of Research and Innovation (GSRI), Greece; Istituto Nazionale di Fisica Nucleare (INFN) and Ministero dell'Università e della Ricerca (MUR), through PRIN 2022 program (Grant PANTHEON 2022E2J4RK, Next Generation EU) and PON R&I program (Avviso n. 424 del 28 febbraio 2018, Progetto PACK-PIR01 00021), Italy; IDMAR project PoFesr Sicilian Region az. 1.5.1; A. De Benedittis, W. Idrissi Ibsalikh, M. Bendahman, A. Nayerhoda, G. Papalashvili, I. C. Rea, A. Simonelli have been supported by the Italian Ministero dell'Università e della Ricerca (MUR), Progetto CIR01 00021 (Avviso n. 2595 del 24 dicembre 2019); KM3NeT4RR MUR Project National Recovery and Resilience Plan (NRRP), Mission 4 Com-



ponent 2 Investment 3.1, Funded by the European Union – NextGenerationEU, CUP I57G21000040001, Concession Decree MUR No. n. Prot. 123 del 21/06/2022; Ministry of Higher Education, Scientific Research and Innovation, Morocco, and the Arab Fund for Economic and Social Development, Kuwait; Nederlandse organisatie voor Wetenschappelijk Onderzoek (NWO), the Netherlands; The grant “AstroCeNT: Particle Astrophysics Science and Technology Centre”, carried out within the International Research Agendas programme of the Foundation for Polish Science financed by the European Union under the European Regional Development Fund; The program: “Excellence initiative-research university” for the AGH University in Krakow; The ARTIQ project: UMO-2021/01/2/ST6/00004 and ARTIQ/0004/2021; Ministry of Research, Innovation and Digitalisation, Romania; Slovak Research and Development Agency under Contract No. APVV-22-0413; Ministry of Education, Research, Development and Youth of the Slovak Republic; MCIN for PID2021-124591NB-C41, -C42, -C43 and PDC2023-145913-I00 funded by MCIN/AEI/10.13039/501100011033 and by “ERDF A way of making Europe”, for ASFAE/2022/014 and ASFAE/2022 /023 with funding from the EU NextGenerationEU (PRTR-C17.I01) and Generalitat Valenciana, for Grant AST22\_6.2 with funding from Consejería de Universidad, Investigación e Innovación and Gobierno de España and European Union - NextGenerationEU, for CSIC-INFRA23013 and for CNS2023-144099, Generalitat Valenciana for CIDE-GENT/2018/034, /2019/043, /2020/049, /2021/23, for CIDEIG/2023/20, for CIPROM/2023/51 and for GRISOLIAP/2021/192 and EU for MSC/101025085, Spain; Khalifa University internal grants (ESIG-2023-008, RIG-2023-070 and RIG-2024-047), United Arab Emirates; The European Union’s Horizon 2020 Research and Innovation Programme (ChETEC-INFRA - Project no. 101008324).

This work is supported by NSF grants AST2407603 and AST2407604. We thank the California Institute of Technology and the Max Planck Institute for Radio Astronomy for supporting the OVRO 40 m program under extremely difficult circumstances over the last 8 years in the absence of agency funding. Without this private support these observations could not have been made. We also thank all the volunteers who have enabled this work to be carried out. Prior to 2016, the OVRO program was supported by NASA grants NNG06GG1G, NNX08AW31G, NNX11A043G, and NNX13AQ89G from 2006 to 2016 and NSF grants AST-0808050 and AST-1109911 from 2008 to 2014.

K.T. acknowledges support from the European Research

Council (ERC) under the European Unions Horizon 2020 research and innovation programme under grant agreement No. 771282.

I.L, S.K. and AP were funded by the European Union ERC-2022-STG - BOOTES - 101076343. Views and opinions expressed are however those of the author(s) only and do not necessarily reflect those of the European Union or the European Research Council Executive Agency. Neither the European Union nor the granting authority can be held responsible for them.

W.M., R.R., B.M. and P.V.d.l.P. acknowledge support from ANID BASAL FB210003 (CATA). R.R., B.M. and P.V.d.l.P. acknowledge support from Núcleo Milenio TITANs (NCN2023\_002). R.B. and N.G. acknowledge support by a grant from the Simons Foundation (00001470, RB, NG). P.V.d.l.P. also acknowledges support by the National Agency for Research and Development (ANID) / Scholarship Program / Doctorado Nacional/2023-21232103.

T.H. acknowledges support from the Academy of Finland projects 317383, 320085, 322535, and 345899.

The work by A.V. Popkov, Y.A.K., S.V.T., A.K.E, and Y.V.S. is supported in the framework of the State project “Science” by the Ministry of Science and Higher Education of the Russian Federation under the contract 075-15-2024-541.

A.V. Plavin is a postdoctoral fellow at the Black Hole Initiative, which is funded by grants from the John Templeton Foundation (grants 60477, 61479, 62286) and the Gordon and Betty Moore Foundation (grant GBMF-8273).

This research has made use of data and/or software provided by the High Energy Astrophysics Science Archive Research Center (HEASARC), which is a service of the Astrophysics Science Division at NASA/GSFC.

This research has made use of the NASA/IPAC Extragalactic Database, which is funded by the National Aeronautics and Space Administration and operated by the California Institute of Technology. Part of this work is based on archival data, software or online services provided by the Space Science Data Center - ASI.

This work made use of the Swinburne University of Technology software correlator, developed as part of the Australian Major National Research Facilities Programme and operated under license (Deller et al. 2011). This work is partly based on the data obtained with the RATAN-600 radio telescope at the Special Astrophysical Observatory of the Russian Academy of Sciences (SAO RAS).

The National Radio Astronomy Observatory is a facil-

ity of the National Science Foundation operated under cooperative agreement by Associated Universities, Inc. This research has made use of data from the Radio Fundamental Catalog (RFC, [10.25966/dhrk-zh08](https://doi.org/10.25966/dhrk-zh08), [Petrov & Kovalev 2025](#)).

This research has made use of data from the MOJAVE database that is maintained by the MOJAVE team ([Lis-ter et al. 2018](#)). This paper makes use of the following ALMA data: ADS/JAO.ALMA#2011.0.00001.CAL. ALMA is a partnership of ESO (representing its member states), NSF (USA) and NINS (Japan), together with NRC (Canada), NSTC and ASIAA (Taiwan), and KASI (Republic of Korea), in cooperation with the Republic of Chile. The Joint ALMA Observatory is operated by ESO, AUI/NRAO and NAOJ. This publication makes use of data products from the Wide-field Infrared Survey Explorer, which is a joint project of the University of California, Los Angeles, and the Jet Propulsion Laboratory/California Institute of Technology, funded by the National Aeronautics and Space Administration.

This work presents results from the European Space Agency (ESA) space mission Gaia. Gaia data are being processed by the Gaia Data Processing and Analysis Consortium (DPAC). Funding for the DPAC is provided by national institutions, in particular the institutions participating in the Gaia MultiLateral Agreement (MLA). The Gaia mission website is <https://www.cosmos.esa.int/gaia>. The Gaia archive website is <https://archives.esac.esa.int/gaia>.

This work has made use of data from the Asteroid Terrestrial-impact Last Alert System (ATLAS) project. The Asteroid Terrestrial-impact Last Alert System (ATLAS) project is primarily funded to search for near earth asteroids through NASA grants NN12AR55G, 80NSSC18K0284, and 80NSSC18K1575; byproducts of the NEO search include images and catalogs from the survey area. This work was partially funded by Kepler/K2 grant J1944/80NSSC19K0112 and HST GO-15889, and STFC grants ST/T000198/1 and ST/S006109/1. The ATLAS science products have been made possible through the contributions of the University of Hawaii Institute for Astronomy, the Queen's University Belfast, the Space Telescope Science Institute, the South African Astronomical Observatory, and The Millennium Institute of Astrophysics (MAS), Chile. This work is based on observations obtained with the Samuel Oschin Telescope 48-inch and the 60-inch Telescope at the Palomar Observatory as part of the Zwicky Transient Facility project. ZTF is supported by the National Science Foundation under Grant No. AST-2034437 and a collaboration including Caltech, IPAC,

the Weizmann Institute for Science, the Oskar Klein Center at Stockholm University, the University of Maryland, Deutsches Elektronen-Synchrotron and Humboldt University, the TANGO Consortium of Taiwan, the University of Wisconsin at Milwaukee, Trinity College Dublin, Lawrence Livermore National Laboratories, and IN2P3, France. Operations are conducted by COO, IPAC, and UW.

We acknowledge the use of public data from the Catalina Real-Time Transient Survey.

This work is partly based on data from eROSITA, the soft X-ray instrument aboard SRG, a joint Russian-German science mission supported by the Russian Space Agency (Roskosmos), in the interests of the Russian Academy of Sciences represented by its Space Research Institute (IKI), and the Deutsches Zentrum für Luft- und Raumfahrt (DLR). The SRG spacecraft was built by Lavochkin Association (NPOL) and its subcontractors, and is operated by NPOL with support from the Max Planck Institute for Extraterrestrial Physics (MPE). The development and construction of the eROSITA X-ray instrument was led by MPE, with contributions from the Dr. Karl Remeis Observatory Bamberg & ECAP (FAU Erlangen-Nuernberg), the University of Hamburg Observatory, the Leibniz Institute for Astrophysics Potsdam (AIP), and the Institute for Astronomy and Astrophysics of the University of Tübingen, with the support of DLR and the Max Planck Society. The Argelander Institute for Astronomy of the University of Bonn and the Ludwig Maximilians Universität Munich also participated in the science preparation for eROSITA. The eROSITA data shown here were processed using the eSASS software system developed by the German eROSITA consortium.

We thank the Swift PI, the Observation Duty Scientists, and the science planners for promptly approving and executing our Swift observations (Obs ID 18990, Obs ID 36371). We acknowledge the use of public data from the Neil Gehrels Swift Observatory data archive.

This research has made use of data obtained from the Chandra Data Archive and the Chandra Source Catalog, both provided by the Chandra X-ray Center (CXC). We acknowledge the use of public data from the ROSAT survey. The ROSAT project is supported by the German Bundesministerium für Bildung, Wissenschaft, Forschung und Technologie (BMBF/DARA) and the Max-Planck-Society.

This work was supported by CNES, focused on *SVOM*. The Space Variable Objects Monitor (*SVOM*) is a China-France joint mission led by the Chinese National Space Administration (CNSA), French Space Agency (CNES), and the Chinese Academy of Sciences (CAS),

which is dedicated to observing gamma-ray bursts and other transient phenomena in the energetic universe. The *Fermi* LAT Collaboration acknowledges generous ongoing support from a number of agencies and institutes that have supported both the development and the operation of the LAT as well as scientific data analysis. These include the National Aeronautics and Space Administration and the Department of Energy in the United States, the Commissariat à l’Energie Atomique and the Centre National de la Recherche Scientifique / Institut National de Physique Nucléaire et de Physique des Particules in France, the Agenzia Spaziale Italiana and the Istituto Nazionale di Fisica Nucleare in Italy, the Ministry of Education, Culture, Sports, Science and

Technology (MEXT), High Energy Accelerator Research Organization (KEK) and Japan Aerospace Exploration Agency (JAXA) in Japan, and the K. A. Wallenberg Foundation, the Swedish Research Council and the Swedish National Space Board in Sweden. Additional support for science analysis during the operations phase is gratefully acknowledged from the Istituto Nazionale di Astrofisica in Italy and the Centre National d’Études Spatiales in France. This work performed in part under DOE Contract DE-AC02-76SF00515.

*Facilities:* KM3NeT, VLA, VLBA, RATAN-600, OVRO, *Swift*, *Fermi*, SRG/*eROSITA*, *Gaia*, CRTS, ATLAS, ZTF, WISE/NEOWISE, *Chandra*, *ROSAT*.

## APPENDIX

### A. MULTI-WAVELENGTH DATA

In following sections, an overview of the data collected is provided. The data span various energy ranges and are retrieved from public archives, proprietary datasets, and proposed observations. Some implications of the observed data on several sources of the candidate sample are discussed. The corresponding multi-wavelength light curves for each source are displayed in [Figure A6](#) through [Figure A22](#).

#### A.1. Radio data

##### A.1.1. VLBI and parsec-scale AGN jets

This paper utilizes both archival and new dedicated VLBI observations. Archival measurements are used in [Section 3](#) in the form of the RFC ([Petrov & Kovalev 2025](#)) that catalogues a complete uniform all-sky sample of VLBI-bright sources, dominated by blazars. Further, a VLBI image from the MOJAVE (Monitoring Of Jets in Active galactic nuclei with VLBA Experiments; [Lister et al. 2018](#)) is used for illustration of the parsec-scale structure in [Figure 2](#).

A dedicated VLBA observation session was performed to cover a deeper complete sample of sources within the 3° uncertainty region of KM3-230213A. The parsec-scale properties of all sources that are catalogued in the VLA Sky Survey (VLASS; [Lacy et al. 2020](#)) with a (2–4) GHz flux density greater than 50 mJy are investigated. This selection results in forty-two objects. On November 25, 2024, their parsec-scale radio emission was measured by VLBA. Measurements at two centre frequencies of 4.4 GHz and 7.6 GHz were obtained using the wide C-band receiver, with 4 Gbps total bandwidth, 128-MHz-wide frequency channels, and two 6-minute scans per target. In the VLBA archive, this experiment is listed as as BK257.

Source positions for observations and correlations are taken from the RFC catalogue ([Petrov & Kovalev 2025](#)) when available, or from VLASS if no RFC counterpart is present. A priori amplitude, phase, and bandpass calibration are performed in AIPS ([Greisen 2003](#)). For comparison, an independent a priori calibration using rPicard/CASA ([Janssen et al. 2019](#)) is performed, obtaining consistent results, with rPicard-calibrated correlated flux densities being systematically 12% lower. Radio frequency interference partially affects the data in the 7.6 GHz sub-band, which is marked manually in AIPS and automatically in rPicard. The PIMA software ([Petrov et al. 2011](#)) is used to evaluate the probability of false positives and the detection sensitivity. The detection limit is found to be about 6 mJy, which is in agreement with the expectations from thermal noise.

Automated hybrid imaging is performed, applying self-calibration and CLEAN imaging to the AIPS-calibrated data in difmap ([Shepherd 1997](#); [Pearson & Readhead 1984](#)). The phase self-calibration solution interval is limited to 12s to avoid creating a “fake” signal from noise, following [Popkov et al. \(2021\)](#). Most of the sources are slightly resolved, and the properties of their structure are measured by fitting the source structure with two circular Gaussian components directly to the self-calibrated visibility data.

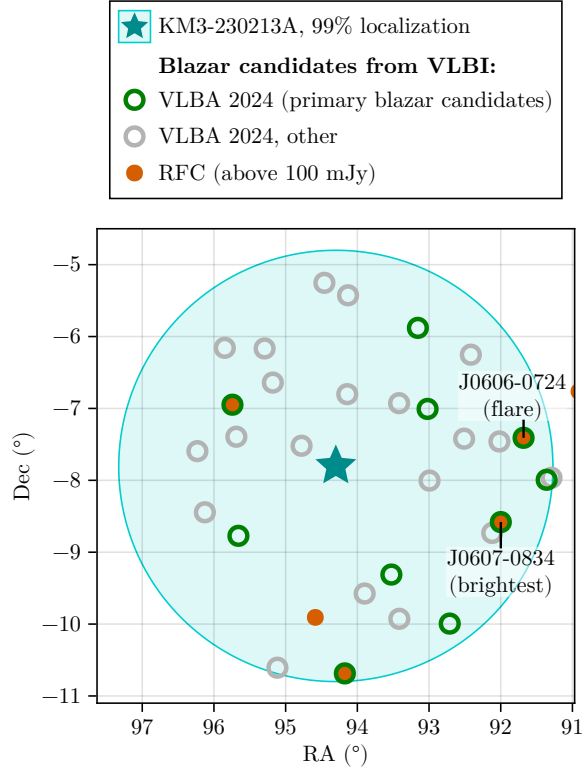


**Figure A1.** Likely blazar candidates within the KM3-230213A 99% localisation area, based on their parsec-scale radio emission properties. See Table 1 and Appendix A.1.1 for details. Two blazars are labelled in the plot: PMN J0606-0724 exhibits the strongest temporal correlation of radio flares to the neutrino arrival (analysed in Appendix B); 0605-085 is the brightest in terms of parsec-scale emission.

Results for sources observed within this VLBA program are presented in Table 2. The calibrated visibility and image FITS files of these observations are published in an electronic format. These measurements allow to select highly-luminous AGN jets with strong beaming. Sources where the parsec-scale radio emission (VLBI) is bright, dominates over larger scales (VLA), and has a flat radio spectrum at parsec scales due to synchrotron opacity are identified as likely blazars, with the radio emission coming from jets aligned with the line of sight.

Sources are marked as primary candidate blazars in Table 2 and highlighted in Figure 1 and Figure A1 when they meet all the following criteria: (i) detected on parsec scales with compactness  $S_{\text{VLBA}}^{5\text{GHz}}/S_{\text{VLASS}} > 0.5$ , (ii) parsec scale (5–8) GHz spectral index  $\alpha_{\text{VLBA}} > -0.5$ , (iii) core brightness temperature  $T_b > 10^{10}$  K at either 5 GHz or 8 GHz. The observed flux densities at the end of 2024 are similar to historical averages (Table 2). In particular, no major flare was detected during this time.

#### A.1.2. OVRO 40 m

The Owens Valley Radio Observatory (OVRO) 40-meter Telescope has been dedicated to monitoring a carefully-selected sample of 1158 blazars on a (3–4)-day cadence since January 2008, using symmetrical off-axis dual-beam optics in double switching mode to minimise atmospheric effects. The details of the observing method, data reduction, and observations are given in Readhead et al. (1989) and Richards et al. (2011). The cryogenic receiver is centred at 15 GHz with a 2 GHz equivalent noise bandwidth.

The quasar 3C 286 is used for absolute flux density calibration, with an assumed value of 3.44 Jy (Baars et al. 1977). Occasionally, the molecular cloud DR 21 is used, calibrated relative to 3C 286 using early OVRO 40 m data. A temperature stabilised noise diode is used to compensate for gain drifts.

The sample of OVRO sources used for the temporal analysis in Appendix B is the Candidate Gamma-Ray Blazar Survey Source (CGRaBS) sample north of declination  $-20^\circ$  (Healey et al. 2008). CGRaBS is a catalogue of AGN with radio and X-ray properties similar to EGRET gamma-ray blazars, selected from a parent population of flat-spectrum

**Table 2.** Properties of sources observed with VLBA within  $3^\circ$  from the KM3-230213A position.

| Blaz<br>(1) | Name<br>(J2000)<br>(2) | Position<br>J2000 RA and Dec.<br>(3) |               | Sep<br>( $^\circ$ )<br>(4) | z<br>(5) | $S_{\text{VLASS}}$      |                            | $S_{\text{VLBA}}$     |                       | $\alpha_{\text{VLBA}}$ | Core $T_b$           |                      |                     |
|-------------|------------------------|--------------------------------------|---------------|----------------------------|----------|-------------------------|----------------------------|-----------------------|-----------------------|------------------------|----------------------|----------------------|---------------------|
|             |                        |                                      |               |                            |          | 2-4 GHz<br>(mJy)<br>(6) | Hist 8 GHz<br>(mJy)<br>(7) | 5 GHz<br>(mJy)<br>(8) | 8 GHz<br>(mJy)<br>(9) | 5-8 GHz<br>(10)        | 5 GHz<br>(K)<br>(11) | 8 GHz<br>(K)<br>(12) |                     |
| x           | J0607-0834             | 06:07:59.699                         | -08:34:49.978 | *                          | 2.4      | 0.87                    | 3100                       | 2067                  | $2176 \pm 220$        | $2240 \pm 226$         | $0.05 \pm 0.26$      | $10^{11.9 \pm 0.1}$  | $10^{11.3 \pm 0.1}$ |
| x           | J0606-0724             | 06:06:43.546                         | -07:24:30.231 | *                          | 2.6      | 1.227                   | 461                        | 309                   | $379 \pm 38$          | $306 \pm 31$           | $-0.38 \pm 0.26$     | $> 10^{12.0}$        | $10^{10.4 \pm 0.1}$ |
| x           | J0616-1041             | 06:16:41.808                         | -10:41:08.456 | *                          | 2.9      |                         | 197                        | 185                   | $215 \pm 22$          | $248 \pm 25$           | $0.26 \pm 0.26$      | $> 10^{10.4}$        | $> 10^{12.1}$       |
| x           | J0622-0656             | 06:22:58.046                         | -06:56:51.971 | *                          | 1.7      |                         | 101                        | 103                   | $111 \pm 11$          | $87 \pm 9$             | $-0.42 \pm 0.26$     | $> 10^{12.1}$        | $> 10^{10.9}$       |
| x           | J0610-0959             | 06:10:50.711                         | -09:59:33.958 | *                          | 2.7      |                         | 97                         | 78                    | $100 \pm 10$          | $94 \pm 10$            | $-0.11 \pm 0.26$     | $> 10^{12.1}$        | $> 10^{11.4}$       |
| x           | J0622-0846             | 06:22:37.999                         | -08:46:18.263 | *                          | 1.7      |                         | 61                         | 74                    | $93 \pm 10$           | $109 \pm 12$           | $0.28 \pm 0.27$      | $> 10^{12.2}$        | $> 10^{12.0}$       |
| x           | J0605-0759             | 06:05:26.187                         | -07:59:31.786 | *                          | 2.9      |                         | 149                        | 74                    | $76 \pm 8$            | $67 \pm 7$             | $-0.24 \pm 0.27$     | $10^{9.9 \pm 0.1}$   | $10^{10.2 \pm 0.1}$ |
| x           | J0614-0918             | 06:14:06.042                         | -09:18:37.911 | *                          | 1.7      |                         | 95                         | 63                    | $72 \pm 7$            | $55 \pm 6$             | $-0.46 \pm 0.27$     | $10^{10.5 \pm 0.2}$  | $> 10^{9.8}$        |
| x           | J0612-0700             | 06:12:04.843                         | -07:00:22.853 |                            | 1.5      |                         | 63                         |                       | $54 \pm 6$            | $62 \pm 7$             | $0.24 \pm 0.27$      | $10^{10.2 \pm 0.1}$  | $> 10^{11.0}$       |
| x           | J0612-0552             | 06:12:37.360                         | -05:52:44.418 | *                          | 2.2      |                         | 65                         | 62                    | $53 \pm 6$            | $45 \pm 5$             | $-0.29 \pm 0.27$     | $10^{10.5 \pm 0.3}$  | $> 10^{10.0}$       |
|             | J0609-0615             | 06:09:39.974                         | -06:15:05.858 | *                          | 2.4      | 2.219                   | 83                         | 39                    | $70 \pm 7$            | $48 \pm 5$             | $-0.66 \pm 0.27$     | $10^{9.8 \pm 0.1}$   | $10^{9.5 \pm 0.1}$  |
|             | J0615-0934             | 06:15:35.497                         | -09:34:27.996 | *                          | 1.8      |                         | 105                        | 30                    | $67 \pm 7$            | $39 \pm 4$             | $-0.97 \pm 0.27$     | $10^{9.9 \pm 0.1}$   | $10^{9.0 \pm 0.1}$  |
|             | J0620-1036             | 06:20:27.542                         | -10:36:22.106 | *                          | 2.9      |                         | 172                        | 39                    | $63 \pm 7$            | $43 \pm 5$             | $-0.66 \pm 0.27$     | $10^{9.6 \pm 0.1}$   | $10^{9.2 \pm 0.1}$  |
|             | J0624-0735             | 06:24:55.342                         | -07:35:37.194 |                            | 1.9      |                         | 110                        |                       | $58 \pm 6$            | $50 \pm 5$             | $-0.25 \pm 0.27$     | $10^{9.9 \pm 0.1}$   | $10^{9.2 \pm 0.1}$  |
|             | J0622-0723             | 06:22:44.911                         | -07:23:34.839 |                            | 1.4      |                         | 94                         |                       | $53 \pm 6$            | $32 \pm 4$             | $-0.86 \pm 0.28$     | $10^{9.1 \pm 0.1}$   | $> 10^{9.8}$        |
|             | J0621-0609             | 06:21:10.364                         | -06:09:54.206 | *                          | 1.9      |                         | 132                        | 65                    | $49 \pm 7$            | $44 \pm 5$             | $-0.18 \pm 0.31$     | $> 10^{9.9}$         | $> 10^{10.6}$       |
|             | J0620-0638             | 06:20:42.818                         | -06:38:24.334 | *                          | 1.5      |                         | 101                        | $26^c$                | $25 \pm 3$            | $18 \pm 2$             | $-0.55 \pm 0.30$     | $> 10^{10.4}$        | $> 10^{9.8}$        |
|             | J0608-0727             | 06:08:04.370                         | -07:27:32.822 | *                          | 2.3      |                         | 356                        | 19                    | $23 \pm 3$            | $22 \pm 3$             | $-0.09 \pm 0.30$     | $> 10^{10.9}$        | $> 10^{10.6}$       |
|             | J0623-0609             | 06:23:23.723                         | -06:09:22.673 |                            | 2.3      |                         | 53                         |                       | $20 \pm 2$            | $23 \pm 3$             | $0.23 \pm 0.31$      | $> 10^{10.7}$        | $> 10^{10.3}$       |
|             | J0616-0648             | 06:16:33.667                         | -06:48:03.289 |                            | 1.0      |                         | 52                         |                       | $19 \pm 2$            | $18 \pm 2$             | $-0.04 \pm 0.31$     | $> 10^{9.7}$         | $> 10^{9.9}$        |
|             | J0611-0800             | 06:11:58.357                         | -08:00:11.217 | *                          | 1.3      |                         | 88                         | 14                    | $17 \pm 2$            | $18 \pm 2$             | $0.14 \pm 0.28$      | $> 10^{10.3}$        | $> 10^{10.1}$       |
|             | J0624-0826             | 06:24:30.354                         | -08:26:38.949 |                            | 1.9      |                         | 56                         |                       | $13 \pm 2$            | $17 \pm 2$             | $0.41 \pm 0.37$      | $> 10^{9.5}$         | $> 10^{8.4}$        |
|             | J0617-0515             | 06:17:50.307                         | -05:15:07.396 |                            | 2.6      |                         | 98                         |                       | $28 \pm 3$            | $> 16$                 |                      | $10^{7.6 \pm 0.1}$   | $10^{6.7 \pm 0.4}$  |
|             | J0605-0757             | 06:05:10.018                         | -07:57:50.331 |                            | 3.0      |                         | 53                         |                       | $> 26$                |                        |                      | $> 10^{6.7}$         |                     |
|             | J0616-0525             | 06:16:31.146                         | -05:25:32.225 |                            | 2.4      |                         | 77                         |                       | $> 9$                 | $> 9$                  |                      | $> 10^{8.6}$         | $> 10^{7.3}$        |
|             | J0610-0725             | 06:10:02.513                         | -07:25:12.715 |                            | 1.8      |                         | 57                         |                       | $> 7$                 | $> 10$                 |                      | $> 10^{6.6}$         | $> 10^{7.6}$        |
|             | J0613-0955             | 06:13:39.450                         | -09:55:34.713 |                            | 2.3      |                         | 75                         |                       |                       | $> 9$                  |                      |                      | $> 10^{7.7}$        |
|             | J0608-0843             | 06:08:28.480                         | -08:43:53.539 |                            | 2.4      |                         | 69                         |                       |                       | $< 6$                  |                      |                      |                     |
|             | J0613-0655             | 06:13:40.138                         | -06:55:34.607 |                            | 1.2      |                         | 123                        | $< 12$                |                       | $< 6$                  |                      |                      |                     |
|             | J0619-0731             | 06:19:06.739                         | -07:31:07.183 |                            | 0.6      |                         | 51                         |                       |                       | $< 6$                  |                      |                      |                     |
|             | J0605-0716             | 06:05:27.091                         | -07:16:23.639 |                            | 3.0      |                         | 50                         |                       |                       | $< 6$                  |                      |                      |                     |
|             | J0607-0610             | 06:07:16.721                         | -06:10:29.815 |                            | 2.9      |                         | 71                         | $< 20$                |                       | $< 6$                  |                      |                      |                     |
|             | J0608-0738             | 06:08:03.661                         | -07:38:31.374 |                            | 2.3      |                         | 192                        | $< 12$                |                       | $< 6$                  |                      |                      |                     |
|             | J0608-0700             | 06:08:36.934                         | -07:00:01.723 |                            | 2.3      |                         | 93                         | $< 20$                |                       | $< 6$                  |                      |                      |                     |
|             | J0610-0559             | 06:10:09.582                         | -05:59:51.932 |                            | 2.5      |                         | 67                         | $< 20$                |                       | $< 6$                  |                      |                      |                     |
|             | J0610-0611             | 06:10:50.604                         | -06:11:49.999 |                            | 2.2      |                         | 111                        | $< 20$                |                       | $< 6$                  |                      |                      |                     |
|             | J0614-1038             | 06:14:45.393                         | -10:38:04.475 |                            | 2.9      |                         | 81                         |                       |                       | $< 6$                  |                      |                      |                     |
|             | J0615-0644             | 06:15:47.557                         | -06:44:47.652 |                            | 1.1      |                         | 78                         |                       |                       | $< 6$                  |                      |                      |                     |
|             | J0618-0719             | 06:18:47.839                         | -07:19:15.503 |                            | 0.6      |                         | 59                         |                       |                       | $< 6$                  |                      |                      |                     |
|             | J0624-0721             | 06:24:14.681                         | -07:21:05.721 |                            | 1.8      |                         | 57                         |                       |                       | $< 6$                  |                      |                      |                     |
|             | J0625-0904             | 06:25:18.204                         | -09:04:35.619 |                            | 2.4      |                         | 64                         |                       |                       | $< 6$                  |                      |                      |                     |
|             | J0625-0703             | 06:25:29.624                         | -07:03:37.547 |                            | 2.2      |                         | 60                         |                       |                       | $< 6$                  |                      |                      |                     |

Note: (1) – Primary blazar candidate mark, see details in [Appendix A.1.1](#); (2) – J2000 source name; (3) – J2000 source positions, Right Ascension and Declination; asterisk “\*” denotes VLBI-astrometry positions from RFC, the rest of coordinates are taken from the VLASS; (4) – Separation between the KM3-230213A position and the source position in degrees; (5) – Redshift as reported by the NASA Extragalactic Database; (6) – Flux density at (2–4) GHz measured within the VLASS; (7) – Historic total VLBI flux density from the RFC database at 8 GHz; in case the 5 GHz VLBI flux density is available instead, it is marked by the note “ $c$ ”; (8) and (9) – Total VLBI flux density at 5 GHz and 8 GHz with its  $1\sigma$  uncertainty, measured by the VLBA observations on 25 November 2024, respectively; (10) – VLBA total spectral index between 5 GHz and 8 GHz  $\alpha$  ( $S \propto \nu^\alpha$ ); (11) and (12) – brightness temperature of the core at 5 GHz and 8 GHz with its  $1\sigma$  uncertainty, respectively. Uncertainties of the VLBI flux scale are about or less than 10%; this uncertainty is accounted for in the measurements presented in this table.

radio sources ( $\alpha > -0.5$ ) with 4.8 GHz flux density  $> 65$  mJy. After removing J1310+3233, a faint target that suffers from confusion with a bright nearby source, the sample used in this paper is reduced to 1157 objects.



### A.1.3. RATAN-600

The RATAN-600<sup>2</sup> observations of broadband radio spectra in the meridian transit mode are used. They cover six frequency bands: 0.96/1.2, 2.3, 4.7, 7.7/8.2, 11, and 22 GHz, quasi-simultaneously across the different bands, within 3–5 minutes (Parijskij 1993). Ten flux density calibrators are used to construct multi-frequency calibration curves covering the declination range between  $-35^\circ$  and  $+45^\circ$ : J0025–26, J0137+33, J0240–23, J0521+16, J0627–05, J1154–35, J1331+30 (3C 286), J1347+12, J2039+42 (DR 21), and J2107+42 (NGC 2027) (Baars et al. 1977; Ott et al. 1994; Aliakberov et al. 1985; Perley & Butler 2013, 2017). Details of the RATAN-600 antenna, radiometers and data reduction are presented in Kovalev et al. (1999); Tsybulev (2011); Udovitskiy et al. (2016); Tsybulev et al. (2018); Sotnikova (2020). RATAN-600 performs long-term monitoring of a complete sample of about 600 AGN with VLBI correlated flux density  $> 400$  mJy at 8 GHz from the RFC catalog at a cadence of about 3 months.

In this work, the quasi-simultaneous multi-frequency RATAN-600 data are interpolated to 15 GHz for use in the time dependent analysis together with OVRO 15 GHz measurements. The interpolation uses a power law between 22 GHz and the nearest of the lower RATAN-600 frequencies (11 GHz, 8 GHz or 5 GHz) for each observation epoch. The correction for different amplitude scales between telescopes is performed by normalising the interpolated RATAN-600 fluxes by their median ratio to the OVRO measurements. The correction factor is within  $\sim 10\%$  for all sources. For use in the analysis, we restrict the RATAN-600 data to the time period from January 2008 to be consistent with the OVRO lightcurve coverage (Appendix A.1.2).

### A.1.4. ALMA

The calibrator source catalogue of the Atacama Large Millimeter/submillimeter Array (ALMA) is a comprehensive database of astronomical measurements of calibrator sources frequently observed for calibration purposes. The catalogue includes observations for three sources, with data available across three receiver bands (Band 3, 6 and 7, corresponding to 84 – 116 GHz, 211 – 275 GHz, 275 – 373 GHz), providing additional variability information.

### A.1.5. UMRAO

Data from the University of Michigan Radio Astronomy Observatory (UMRAO; Aller et al. 1985; Aller et al. 2014) are provided by M. Aller (private communication), supplementary to the 15 GHz data for 0605-085 (#6) from OVRO and RATAN-600.

## A.2. Infrared and optical data

Archival data in optical and infrared (IR) wavelengths are collected for the sources highlighted in Table 1. In IR, observations performed with (*WISE*; Wright et al. 2010) and the reactivated mission *Near-Earth Object Wide-field Infrared Survey Explore* (*NEOWISE*; Mainzer et al. 2011) between 2009 and 2024 are used. Both missions observe magnitudes in the W1 (3.4  $\mu\text{m}$ ) and W2 (4.6  $\mu\text{m}$ ) bands for all sources with *WISE* counterparts in Table 1. As some sources are observed multiple times per day, the weighted mean of the magnitudes is taken for further processing in each observation day. Magnitudes are then transformed to flux units using the corresponding filter curves and zero points (Jarrett et al. 2011). Similarly, optical light curves are gathered for multiple sources using publicly available data from various facilities. The Asteroid Terrestrial-impact Last Alert System (ATLAS; Tonry et al. 2018; Smith et al. 2020; Heinze et al. 2018), observes the cyan (c) and orange (o) filter bands. The  $5\sigma$  limiting magnitudes are at  $m = 19.7$ . The filter specifications and zero points are provided by the Spanish Virtual Observatory Filter Profile Service (SVO; Rodrigo et al. 2012; Rodrigo & Solano 2020), in addition to the mission publications. The Catalina Realtime Transient Survey (CRTS; Drake et al. 2009) observed the sky region at this declination with two out of three telescopes, CSS and SSS. Both provide magnitudes close to the V-band (UBV photometric system) with magnitude limits of  $m = 19.5$  (CSS) and  $m = 19.0$  (SSS). For times between 2014 and 2017, *Gaia* (Gaia Collaboration et al. 2016, 2023; Babusiaux et al. 2023) provides observations in three custom filters. The filter information and zero points for the G,  $G_{BP}$  and  $G_{RP}$  band is available in Riello et al. (2021). Lastly, observations taken with the Zwicky Transient Facility (ZTF; Masci et al. 2018) are available in the red (r) and the green (g) band with filter information available in SVO. Note that all magnitudes are corrected for galactic extinction using the source dependent  $E(B - V)$  value from Schlafly & Finkbeiner (2011) and following the extinction law of Fitzpatrick (1999) before the conversion to flux units.

<sup>2</sup> in Russian, РАТАН-600 - радиоастрономический телескоп Академии наук, Radio Telescope of the Academy of Sciences



### A.2.1. WISE "blazar strip" selection

The population of gamma-ray blazars has been shown to follow a specific distribution in its infrared observable properties (Massaro et al. 2012). In particular, the infrared colour-colour diagrams evaluated from all four *WISE* observation bands are used to build a selection of blazar-like candidates. Given  $W1$ ,  $W2$ ,  $W3$  and  $W4$  the *WISE* bands at 3.4, 4.6, 12 and 22  $\mu\text{m}$ , respectively, the selection is performed in the three dimensional space where the axes are defined by the colours:  $W1 - W2$ ,  $W2 - W3$ ,  $W3 - W4$ . This classification is statistical in nature. Since the selection adopted in this work is enhanced by the detection of an X-ray counterpart, a 40% extension of the contours area has been applied to select the candidates reported in Table 1.

### A.3. X-ray observations

Publicly available archival data for the sources in the sample are collected. Of the seventeen candidate sources, five (sources #1, #6, #7, #10, and #17) have archival data from the *Neil Gehrels Swift Observatory* (*Swift*), *Chandra X-ray Observatory* (*Chandra*), and/or the *ROentgen SATellite* (*ROSAT*). In particular, 0605-085 #6 has been observed most extensively, with data from 1990 to 2008 from all of the above instruments. In addition, proprietary data from the Spektrum-Roentgen-Gamma Observatory (SRG), in particular from the *eROSITA* instrument, are collected and analysed for the available sources. In addition to the archival observations, a Target of Opportunity (ToO) request with *Swift* was submitted to observe sources #1 and #6. The *Space Variable Objects Monitor* (*SVOM*) satellite has been used to observe the 90% uncertainty region using a tiling pattern. The procedures used to estimate the flux for each instrument, as well as the pipeline used for data analysis, are illustrated in the following. For all observations, the intrinsic flux is calculated assuming a power-law model with galactic absorption, unless stated differently. The estimated fluxes are shown in Table 3.

#### A.3.1. ROSAT

*ROSAT* performed the first imaging X-ray survey of the entire sky between 1990 and 1991. In the following years, until 1999, *ROSAT* entered the pointed observing phase, during which more than 100 000 sources were catalogued (Voges et al. 1999). Among the sample of seventeen blazar-like candidate sources, NVSS J061703–082225 (1RXS J061702.4–08222; 8.2'' offset from optical coordinates) and RFC J0607–0834 (1RXS J060758.7–08344; 14.9'' offset from optical coordinates) have been included in the *ROSAT* All-Sky Survey Faint Source Catalog (Voges et al. 2000). With count rates of  $(1.16 \pm 0.57) \times 10^{-2} \text{ s}^{-1}$  and  $(1.71 \pm 0.68) \times 10^{-2} \text{ s}^{-1}$ , and hardness ratios of  $0.68 \pm 0.73$  and  $1.00 \pm 0.44$ , for NVSS J061703–082225 and RFC J0607–0834, respectively, the intrinsic flux in the (0.1–2.0) keV band is estimated. This is done using the count rate-to-energy flux conversion formula presented in the literature (Schmitt et al. 1995).

NVSS J060639-063421 (#10) has been catalogued in WGACAT, a comprehensive catalog derived from all *ROSAT* PSPC (Position Sensitive Proportional Counter) pointed observations (White et al. 2000). The source is designated 1WGA J0606.6–0633, located at 28.9'' from the optical coordinates, with a count rate of  $(2.99 \pm 0.76) \times 10^{-2} \text{ s}^{-1}$ . WGACAT provides a variety of processed data products for each source, including smoothed intensity images, timing images, light-curve plots, and both source and background spectra. For this object, the available source spectrum is extracted using an optimised box size, along with an additional response file generated using the *pcarf* software (Blackburn 1995). The corresponding response matrix, background spectrum, and ancillary response file are processed with *XSPEC* to estimate the flux in the (0.2 – 2.3) keV band.

#### A.3.2. Swift-XRT

As mentioned above, some of the candidates were previously observed with the *Swift* observatory (Gehrels et al. 2004) in addition to the requested observations. The X-ray data from *Swift*-XRT (Burrows et al. 2005) are processed using *FTOOLS*, part of the *HEASoft* package (v6.33) designed for manipulating and analyzing FITS files. For this analysis, all *Swift*-XRT observations were performed in photon counting (PC) mode. The event files are cleaned and calibrated using standard filtering criteria via the *xrtpipeline* task, using the latest files from the *Swift* CALDB provided by HEASARC.

The spectral extraction for events in the (0.3 – 10.0) keV energy range is performed using the *XSELECT* tool. The source signal was extracted from a circular region with a radius of 20 pixels (47''), corresponding to about 90% of the XRT point spread function (PSF), after visually centring the extraction region at the coordinates of the radio counterpart. The background spectrum was derived from an annular region centred on the optical coordinates of

the source, with an inner radius of 40 pixels ( $\sim 1.5'$ ) and an outer radius of 80 pixels ( $\sim 3.1'$ ). For proper spectral modeling, the binning is set to at least one count per spectral channel, which allows the use of C-statistics (Cash 1979) in XSPEC.

### A.3.3. eROSITA

The SRG observatory (Sunyaev et al. 2021) is equipped with two main instruments: *eROSITA* and ART-XC. *eROSITA* is a groundbreaking instrument for surveying the entire sky in soft X-rays, operating at energies below 3–5 keV. It offers significant advancements compared to earlier facilities like *ROSAT*, with improvements in parameters such as effective area, vignetting function, and point spread function (Predehl et al. 2021).

Using the SRG/*eROSITA* all-sky survey, an investigation was conducted within a  $6 \times 6 \text{ deg}^2$  error box around KM3-230213A, focusing only on X-ray point sources. By analysing the list of potential high-energy counterparts to the neutrino event and matching them to within  $15''$  of the *eROSITA* positions, eleven out of seventeen sources align.

For these sources, spectra are extracted from the pipeline-processed *eROSITA* eventfiles (version 020). Events from all seven telescope modules of eROSITA and from all four completed *eROSITA* All Sky Survey iterations (eRASS:4) are combined. The SRCTOOL task of the *eROSITA* Science Analysis Software System (eSASS) is used to produce source and background spectra, ancillary response files (ARFs) and response matrix files (RMFs). This is done by extracting source counts from circular regions with radii of  $60''$  and background counts from large and nearby regions. For the remaining counterparts to the neutrino event that did not match a point source with *eROSITA*, the upper limits were extracted from Tubín-Arenas et al. (2024).

The eRASS:4 spectra were analysed with the Bayesian X-ray Analysis software (BXA) version 4.1.2 (Buchner et al. (2014)), which connects the nested sampling algorithm UltraNest (Buchner 2019, 2021) with the fitting environment CIAO/Sherpa (Fruscione et al. 2006). Spectra were fit using an unbinned approach and the C-statistic. The fitting procedure included a principal component analysis based background model (Simmonds et al. 2018) derived from a large sample of *eROSITA* background spectra. For all spectra, a power-law model (POWERLAW) is fitted, including the contribution of Galactic absorption through the component TBABS, using the Galactic column density estimated by the HI4PI collaboration (HI4PI Collaboration et al. (2016)).

Variability across different *eROSITA* epochs is examined by comparing the catalogued (0.2–2.3) keV flux values of the individual eRASS surveys (eRASS1 to 4 Merloni et al. 2024). To identify variable sources, the maximum amplitude variability and its significance are evaluated following the definitions of Boller et al. (2016). Two sources are identified as variable between eRASS surveys with a significance  $> 2\sigma$  (MRC 0614-083 and PMN J0616-1040). For these, a time-resolved spectral analysis is performed by applying the same prescriptions as above to the individual eRASS surveys.

### A.3.4. Chandra

From the sample of candidates, the blazar 0605-085 (#6) stands out for its three observations with *Chandra*. These were made with the Advanced CCD Imaging Spectrometer (ACIS-S) spectroscopic array between 2001 and 2009 (Weisskopf et al. 2000). These observations are analysed using the `chandra_repro` script within the CIAO data analysis system (Fruscione et al. 2006), version 4.16, along with the *Chandra* CALDB version 4.11.5. The spectra are extracted using the `specextract` tool provided in the CIAO software suite. In particular, a visual analysis of the reprocessed imaging event file was done to select the region for both the source and the background. For the background, an annular area was utilised, centred on the given coordinates, with an inner radius of  $6''$  and an outer radius of  $20''$ . Conversely, a circular region of approximately  $5''$  was selected for the source, deliberately positioned to exclude the nearby foreground star from being included in the selection. As with the rest of the observations, the spectra are binned to ensure one count per bin to be further modelled with XSPEC.

### A.3.5. SVOM

The Space Variable Objects Monitor (*SVOM*, Wei et al. 2016) was launched on June 22, 2024. At the time of the observations, between 2024-12-16T16:52:25.535Z UTC and 2024-12-17T13:53:34.693Z UTC (spanning fourteen orbits), *SVOM* was in the commissioning and verification phase. *SVOM* observed the 90% neutrino error region using a Multi-Messenger Target of Opportunity (ToO-MM) program. ToO-MM allowed the narrow field-of-view (FoV) instruments onboard *SVOM*, the MXT (Microchannel X-ray Telescope; Götz et al. 2023), operating in the soft 0.5–10 keV X-ray band with a  $58 \times 58$  arcmin sq. FoV, and the VT (Visible Telescope; Fan et al. 2020), operating in the  $VT_B$  (400–650 nm) and  $VT_R$  (650–1000 nm) bands, with a FoV of  $26'$  diameter, to perform tiled observations of the error region

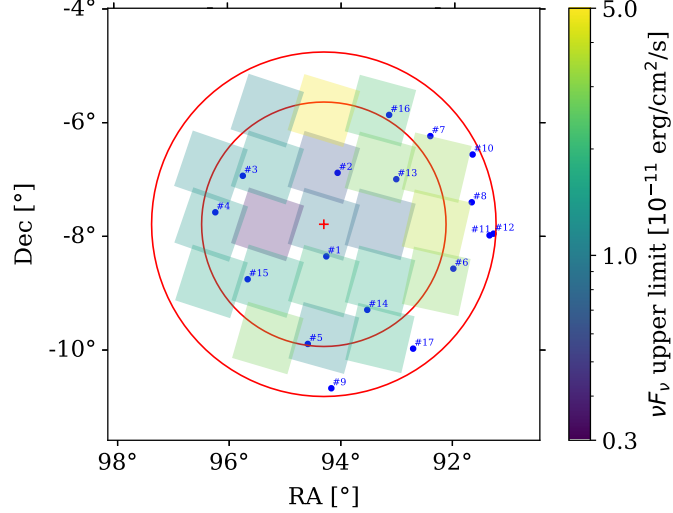


**Figure A2.**  $3\sigma$  upper limits derived from the tiling of the neutrino error region with *SVOM*-MXT over the 0.5–10 keV energy band. The concentric red circles indicate the 90% and 99% error regions of KM3-230213A, respectively. The numbers refer to the candidate blazars listed in Table 1.

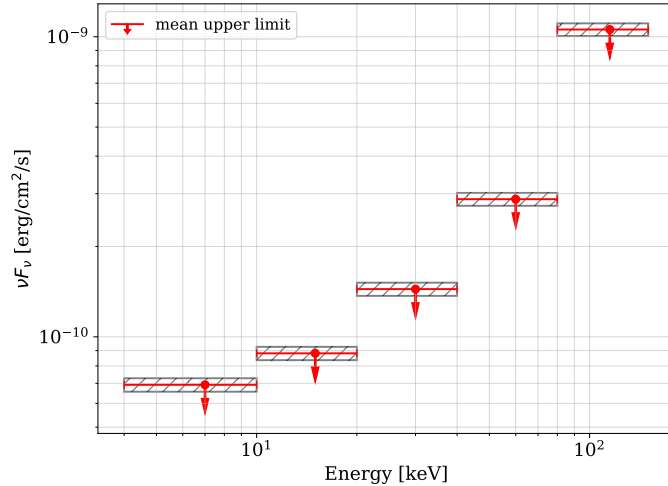


**Figure A3.** *SVOM*-ECLAIRs  $3\sigma$  upper limits on the energy flux in different energy ranges for the candidate blazars listed in Table 1. The average upper limits for the seventeen targets are shown with red markers. The horizontal hatched bands cover the interval between the minimum and maximum upper limits for the candidate sample.

with exposure times ranging from 400 to 2350 s. A total of 21 tiles were observed with an average exposure time of 1218.9 s. *SVOM*-MXT data were processed with its dedicated analysis pipeline. No soft X-ray source was detected in the 90% neutrino error region. Consequently,  $3\sigma$  upper limits on the 0.5–10 keV energy flux were computed at the center of each tile following Kraft et al. (1991). The variability of upper limit across the tiled region is primarily driven by differences in exposure time for each tile. The tiling pattern and the corresponding MXT energy flux upper limits for each tile are shown in Figure A2. None of the candidate blazars listed in Table 1 and lying in the 90% neutrino error region were located in the VT FoV.

In addition, the coded-mask instrument *SVOM*-ECLAIRs (Godet et al. 2014), with its wide FoV of 2 sr, observed the entire error region over the 4–150 keV energy range during the total ToO exposure of 25.6 ks. No source was detected. For each of the seventeen blazars listed in Table 1,  $3\sigma$  upper limits over different energy bands were derived from the ECLAIRs variance maps produced by the ECPI data processing pipeline v1.14.4 and assuming a power law spectral model with  $\Gamma = 2$ . They are summarised in Figure A3.

**Table 3.** Fluxes derived from the available X-ray data in the (0.2-2.3) keV band, given in units of  $10^{-13}$  erg cm $^{-2}$  s $^{-1}$ . Uncertainties are reported at the  $1\sigma$  confidence level. The following notes are used: <sup>a</sup>, derived flux in the (0.1-2.4) keV energy range; <sup>b</sup>, derived flux in the (0.2-2.0) keV energy range. Those marked with a † symbol denote upper limits.

| Source                  | Instrument                | MJD                    | Flux                       |
|-------------------------|---------------------------|------------------------|----------------------------|
| #1 MRC 0614-083         | <i>ROSAT</i> <sup>a</sup> | 47893                  | $1.39^{+0.47}_{-0.48}$     |
|                         | <i>eROSITA</i>            | 58945                  | $3.56^{+0.98}_{-0.79}$     |
|                         | <i>eROSITA</i>            | 59132                  | $3.94^{+1.49}_{-1.06}$     |
|                         | <i>eROSITA</i>            | 59308                  | $6.43^{+1.15}_{-1.95}$     |
|                         | <i>eROSITA</i>            | 59492                  | $7.97^{+1.27}_{-1.11}$     |
|                         | <i>Swift-XRT</i>          | 60666                  | $10.2^{+1.61}_{-1.43}$     |
| #3 PMN J0622-0657       | <i>eROSITA</i>            | 58945                  | $\leq 0.69^{\dagger}$      |
|                         | <i>eROSITA</i>            | 59132                  | $1.02^{+1.94}_{-0.75}$     |
|                         | <i>eROSITA</i>            | 59308                  | $1.46^{+2.62}_{-0.79}$     |
|                         | <i>eROSITA</i>            | 59492                  | $\leq 0.65^{\dagger}$      |
| #4 NVSS J062455-073536  | <i>eROSITA</i>            | 58945                  | $\leq 2.50^{\dagger}$      |
|                         | <i>eROSITA</i>            | 59132                  | $1.49^{+1.98}_{-0.82}$     |
|                         | <i>eROSITA</i>            | 59308                  | $\leq 2.00^{\dagger}$      |
|                         | <i>eROSITA</i>            | 59492                  | $\leq 0.81^{\dagger}$      |
| #6 0605-085             | <i>ROSAT</i> <sup>b</sup> | 47893                  | $2.42^{+0.95}_{-0.95}$     |
|                         | <i>Chandra-ACIS-S</i>     | 52031                  | $9.04^{+0.70}_{-0.64}$     |
|                         | <i>Swift-XRT</i>          | 54214                  | $8.32^{+13.52}_{-7.26}$    |
|                         | <i>Swift-XRT</i>          | 54235                  | $10.40^{+3.02}_{-1.85}$    |
|                         | <i>Swift-XRT</i>          | 54321                  | $12.50^{+5.10}_{-3.26}$    |
|                         | <i>Swift-XRT</i>          | 54323                  | $24.60^{+102.13}_{-13.90}$ |
|                         | <i>Swift-XRT</i>          | 54682                  | $16.30^{+8.80}_{-5.44}$    |
|                         | <i>Swift-XRT</i>          | 54684                  | $19.00^{+9.50}_{-3.90}$    |
|                         | <i>Swift-XRT</i>          | 54687                  | $17.40^{+2.01}_{-1.73}$    |
|                         | <i>Swift-XRT</i>          | 54787                  | $16.10^{+7.81}_{-4.42}$    |
|                         | <i>Chandra-ACIS-S</i>     | 55179                  | $18.70^{+0.72}_{-0.63}$    |
|                         | <i>Chandra-ACIS-S</i>     | 55182                  | $18.20^{+0.70}_{-0.63}$    |
|                         | <i>eROSITA</i>            | 58945                  | $5.20^{+1.26}_{-1.06}$     |
|                         | <i>eROSITA</i>            | 59132                  | $4.24^{+1.12}_{-0.97}$     |
| <i>eROSITA</i>          | 59308                     | $2.82^{+1.17}_{-0.83}$ |                            |
| <i>eROSITA</i>          | 59492                     | $4.97^{+1.24}_{-1.07}$ |                            |
| <i>Swift-XRT</i>        | 60670                     | $7.52^{+1.39}_{-1.19}$ |                            |
| #7 PMN J0609-0615       | <i>Swift-XRT</i>          | 55571                  | $\leq 25.00^{\dagger}$     |
| #8 PMN J0606-0724       | <i>eROSITA</i>            | 58945                  | $\leq 0.71^{\dagger}$      |
|                         | <i>eROSITA</i>            | 59132                  | $\leq 0.63^{\dagger}$      |
|                         | <i>eROSITA</i>            | 59308                  | $0.36^{+0.43}_{-0.24}$     |
|                         | <i>eROSITA</i>            | 59492                  | $\leq 0.35^{\dagger}$      |
| #9 PMN J0616-1040       | <i>eROSITA</i>            | 58945                  | $4.40^{+1.09}_{-0.93}$     |
|                         | <i>eROSITA</i>            | 59132                  | $1.68^{+0.64}_{-0.51}$     |
|                         | <i>eROSITA</i>            | 59308                  | $5.18^{+4.02}_{-2.14}$     |
|                         | <i>eROSITA</i>            | 59492                  | $\leq 0.26^{\dagger}$      |
| #10 NVSS J060639-063421 | <i>ROSAT</i>              | 49244                  | $0.77^{+0.23}_{-0.18}$     |
|                         | <i>eROSITA</i>            | 58945                  | $\leq 0.72^{\dagger}$      |
|                         | <i>eROSITA</i>            | 59132                  | $0.36^{+0.34}_{-0.26}$     |
|                         | <i>eROSITA</i>            | 59308                  | $\leq 1.32^{\dagger}$      |
|                         | <i>eROSITA</i>            | 59492                  | $\leq 0.65^{\dagger}$      |
| #11 PMN J0605-0759      | <i>eROSITA</i>            | 58945                  | $1.47^{+1.22}_{-0.66}$     |
|                         | <i>eROSITA</i>            | 59132                  | $0.75^{+0.77}_{-0.40}$     |
|                         | <i>eROSITA</i>            | 59308                  | $2.13^{+0.86}_{-0.68}$     |
|                         | <i>eROSITA</i>            | 59492                  | $3.62^{+1.33}_{-0.95}$     |
| #12 NVSS J060509-075747 | <i>eROSITA</i>            | 58945                  | $3.11^{+3.48}_{-1.48}$     |
|                         | <i>eROSITA</i>            | 59132                  | $0.92^{+1.55}_{-0.58}$     |
|                         | <i>eROSITA</i>            | 59308                  | $1.29^{+1.62}_{-0.72}$     |
|                         | <i>eROSITA</i>            | 59492                  | $2.38^{+1.13}_{-0.75}$     |
| #13 PMN J0612-0700      | <i>eROSITA</i>            | 58945                  | $\leq 0.29^{\dagger}$      |
|                         | <i>eROSITA</i>            | 59132                  | $\leq 0.72^{\dagger}$      |
|                         | <i>eROSITA</i>            | 59308                  | $\leq 1.81^{\dagger}$      |
|                         | <i>eROSITA</i>            | 59492                  | $\leq 1.10^{\dagger}$      |
| #17 NVSS J061050-095934 | <i>eROSITA</i>            | 58945                  | $\leq 1.35^{\dagger}$      |
|                         | <i>eROSITA</i>            | 59132                  | $\leq 0.25^{\dagger}$      |
|                         | <i>eROSITA</i>            | 59308                  | $\leq 0.76^{\dagger}$      |
|                         | <i>eROSITA</i>            | 59492                  | $0.77^{+0.64}_{-0.38}$     |

#### A.4. Gamma-ray data from Fermi-LAT

Available *Fermi*-LAT data are analysed using the Python package `fermipy` (Wood et al. 2017). The region of interest (RoI) is centred at the best-fit position of KM3-230213A and selected photons from the `Pass 8 SOURCE` class (Atwood et al. 2013; Bruel et al. 2018) within a  $10^\circ \times 10^\circ$  square RoI. The analysis covered the period from 2008 August 04 to 2025 January 11 (MJD 54682 – 60357).

To minimise contamination from gamma rays produced in the Earth’s upper atmosphere, a zenith angle cut of  $\theta < 90^\circ$  is applied. The standard data quality cuts (`DATA_QUAL > 0`)&&(LAT\_CONFIG == 1) are applied, periods coinciding with solar flares and gamma-ray bursts detected by *Fermi*-LAT are excluded. The RoI model included all 4FGL Data Release 4 catalog sources (4FGL-DR4; Ballet et al. 2023) located within  $15^\circ$  of the RoI center, as well as galactic and isotropic diffuse emission models<sup>3</sup> (`gll_iem_v07.fits` and `iso_P8R3_SOURCE_V2_v1.txt`).

A binned likelihood analysis over the (0.1–1000) GeV energy range is performed, using 10 bins per decade in energy and  $0.1^\circ$  spatial bins. The `P8R3_SOURCE_V3` instrumental response functions (IRFs) are adopted.

To model a putative point source at the KM3-230213A best-fit position, a power-law spectrum with a fixed index of 2.0 is used. In the fit, the spectral shapes and parameters reported in the 4FGL-DR4 catalogue for all sources in the RoI are adopted. First, a fit of the ROI is performed by means of the *fermipy* method “optimize” to ensure that all spectral parameters are close to their global likelihood maxima. This is done by iteratively optimizing the components of the ROI model in sequential steps, starting from the largest components.<sup>4</sup>

To check for previously undetected sources, an iterative procedure using a test statistic (TS) map is applied. The TS is defined as  $2 \log(L/L_0)$ , where  $L$  is the likelihood of the model with a point source at a given position and  $L_0$  is the likelihood without the source. A TS value of 25 corresponds to a statistical significance of  $\gtrsim 4.0\sigma$  (as adopted in Abdollahi et al. 2020; Mattox et al. 1996). A TS map is generated by inserting a putative point source at each pixel and evaluating its significance relative to the current best-fit model. The test source is modelled with a power-law spectrum, allowing only the normalization to vary while keeping the photon index fixed at 2.0. A search for peaks with  $TS > 25$  and a minimum separation of  $0.5^\circ$  from existing sources is performed. When a significant peak is found, a new point source is added to the model at that position, re-fitting the RoI, and generating a new TS map. This process is iterated until no more significant excesses are found.

To search for transient and variable gamma-ray emission on intermediate timescales in the LAT data, the same method is applied to 1-day and 1-month intervals prior to the detection of KM3-230213A. No significant ( $> 5\sigma$ ) excess emission is found within the 90% confidence localisation of KM3-230213A. A 95% confidence upper limit for the 0.1 GeV flux is determined at the neutrino position:  $< 6.7 \times 10^{-10}$   $\text{ph cm}^{-2} \text{ s}^{-1}$  for the  $\sim 16$ -year integration, and  $< 6.7 \times 10^{-9}$  ( $< 3.0 \times 10^{-8}$ )  $\text{ph cm}^{-2} \text{ s}^{-1}$  for the 1-month (1-day) integration time. Over these timescales, none of the candidate objects exhibit significant flux enhancements that would suggest flaring behaviour or spectral change at gamma rays.

Since the target is close to the Galactic Plane, the analysis is repeated using a more restrictive lower energy threshold of  $\geq 1$  GeV to reduce contamination from bright galactic emission. This approach also takes advantage of the improved LAT point spread function at higher energies. The results remain consistent with those obtained from the full energy range analysis.

##### A.4.1. The nature of 4FGL J0616.2-0653: point-like source or extended diffuse emission?

The unidentified, catalogued object 4FGL J0616.2-0653 (#2) lacks a confident counterpart at other wavelengths. The *Fermi*-LAT analysis of the region reveals other mild excess gamma-ray emission, most of which appears to be extended and diffuse. The best fit coordinates of 4FGL J0616.2-0653 are RA =  $94.06^\circ$ , Dec =  $-6.90^\circ$  (J2000). Within the 95% gamma-ray error region of  $0.09^\circ$ , no counterparts are found. The closest radio source, NVSS J061633-064804, is  $0.12^\circ$  from the best-fit position of the *Fermi*-LAT object, outside of the 95% error region. While the radio object is one of the targets of the VLBA observation (J0616-0648, Table 2), with indication of a blazar nature, it is not included in our selection of candidates due to its relatively low radio flux density and low estimate of the lower limit of the brightness temperature. The 4FGL-DR4 catalog reports a tentative association of 4FGL J0616.2-0653 with an object that appears in the third EGRET catalog (Hartman et al. 1999). The EGRET source, 3EG J0616–0720, is located at RA, Dec = (94.16, -7.35), with a positional uncertainty of  $0.91^\circ$  (95% positional error). With a separation of  $0.46^\circ$ , 3EG J0616-

<sup>3</sup> LAT Background Models

<sup>4</sup> <https://fermipy.readthedocs.io/en/latest/fitting.html>

0720, classified as an unidentified object, is positionally consistent with 4FGL J0616.2-0653. Casandjian & Grenier (2008) excluded 3EG J0616-0720 from the EGRET Revised (EGR) source list due to additional structure observed in the interstellar medium. The lack of convincing counterparts at different wavelengths (radio, infrared, optical and X-ray) does not support the hypothesis of a point-like origin for 4FGL J0616.2-0653. Furthermore, the excess emission does not appear to be isolated, but rather part of a larger continuous region with an arc-like morphology associated with the Orion molecular clouds (Ackermann et al. 2012). Based on these results, mismodelled diffuse emission may explain the observed gamma-ray excess.

#### A.4.2. *Gamma-ray analysis of KM3-230213A candidate counterparts*

For each object listed in Table 1, the analysis described in the previous section is performed. In addition, to characterise their variability properties, *Fermi*-LAT light curves are generated with 6-month bins. For the likelihood fits of the time bins, the best-fit ROI model obtained from the full time interval analysis is adopted.

First, a fit is attempted by allowing variations in the normalization of the target source, all sources within the inner  $3^\circ$  of the ROI, and the diffuse components. If the fit does not converge, the number of free parameters is iteratively restricted until a successful fit is obtained. This procedure begins by fixing the sources in the ROI that are most weakly detected, starting at  $TS < 4$ . Next, sources with  $TS < 9$  are fixed, followed by sources up to  $1^\circ$  from the ROI centre and those with  $TS < 25$ . Finally, all parameters except the normalization of the target source are fixed.

The target source is considered as detected if  $TS > 9$  in the corresponding time bin. If this condition is not met, a 95% confidence limit is reported, denoted by down pointing arrows in the gamma rays light curves.



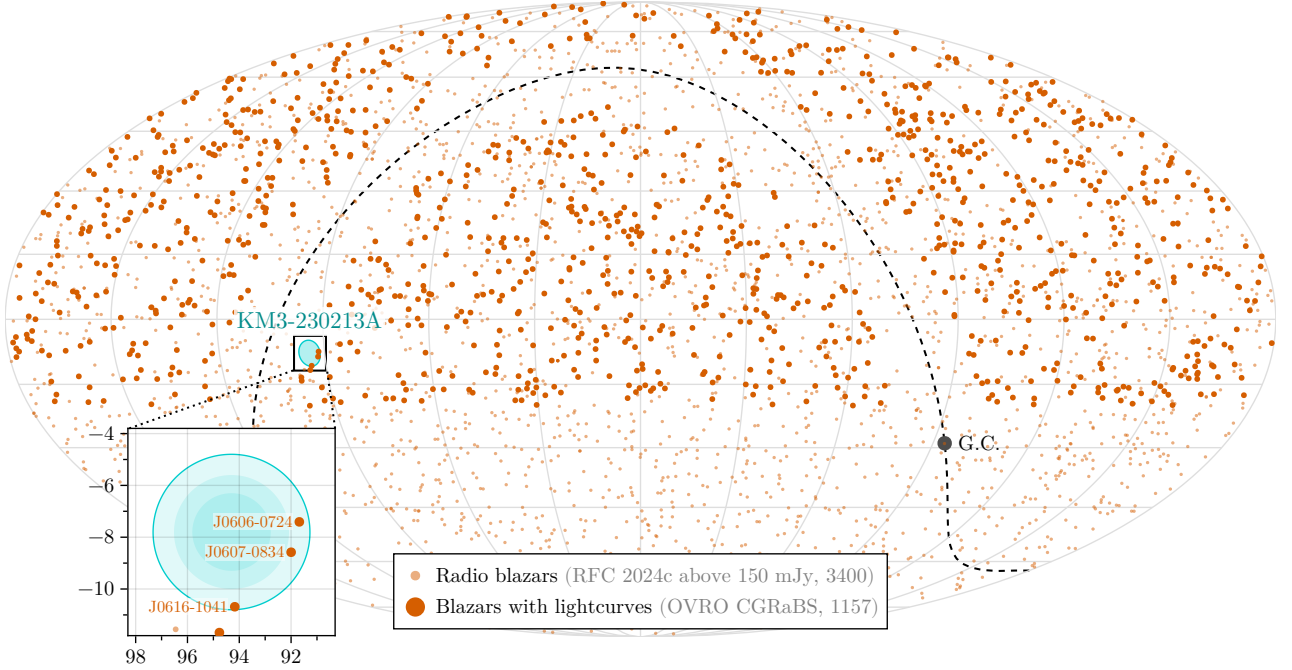


**Figure A4.** The KM3-230213A localisation in the sky (68%, 90% and 99% containment areas shaded in cyan) together with the RFC bright (above 150 mJy) sources (Appendix A.1.1), displayed along with the sources monitored by the OVRO program (Appendix A.1.2). The direction of the event is close to the boundary of the OVRO monitoring area,  $\pm 10^\circ$  from the Galactic Plane (dashed black line). All bright radio blazars in this region are in the CGRaBS sample and have radio light curves available.

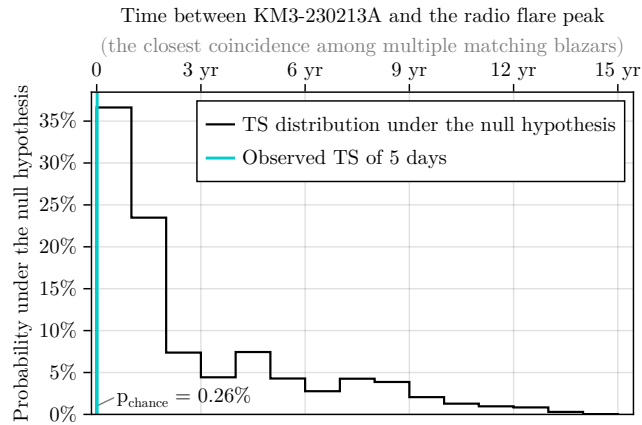


**Figure A5.** The visualisation of the statistical test evaluating the temporal correlation between a radio flare and neutrino arrival for the PMN J0606-0724 blazar. As discussed in Section 5.2, it exhibits the strongest major flare exactly during the neutrino arrival time. The time delay between the neutrino and the flare peak is just 5 days, making the coincidence remarkable even given the  $3^\circ$  angular uncertainty of the neutrino event. Here, the observed value of the test statistic – the neutrino-radio flare delay – is shown in comparison with its distribution under the null hypothesis of no association.

## B. NEUTRINO-RADIO FLARE ASSOCIATION PROBABILITY

A statistical analysis to test the association between neutrino arrival times and major blazar radio flares is performed in this section. This consists of an evaluation of the chance probability of finding, in a  $3^\circ$  circular region, a blazar with a time correlation as strong as the one observed in the data (Section 5.2). For this purpose, only blazars in the

OVRO CGRaBS monitoring programs are considered: for them, a dense continuous radio coverage is available. As seen in [Figure A4](#), the KM3NeT event is relatively close to the Galactic Plane ( $11^\circ$ ), at the edge of the CGRaBS coverage. Still, all bright (above 150 mJy) radio blazars within the neutrino localisation region are covered by the OVRO monitoring program as seen from the lack of other radio sources from the RFC there. Combined OVRO + RATAN light curves are used, see [Appendix A.1.2](#) and [Appendix A.1.3](#) for details.

The aim of the statistical test is to evaluate two hypotheses:

- null hypothesis: the neutrino is unrelated to major blazar flares, either not connected to blazars entirely or not preferring times of major flares;
- alternative hypothesis: the neutrino arrival time is connected to a major radio flare.

*Simulation*—To compute the p-value, Monte Carlo simulations under the null hypothesis are used. In order to simulate the observations using minimal assumptions,  $N = 3$  light curves for random blazars are selected from the full CGRaBS sample. This way, every realization represents the most conservative scenario where the number of coincident blazars is always equal to the observed one.

At each of  $10^6$  simulation steps, the following procedure is repeated:

1. draw  $N = 3$  random blazars from the CGRaBS sample;
2. compute  $TS$  for their light curves according to the  $TS$  definition below.

In this procedure, the arrival time of the neutrino is fixed and individual light curves are not modified in any way.

As the result, the distribution of the test statistic under the null hypothesis is obtained. Comparing the observed  $TS$  value with this distribution leads to the p-value.

*Test statistic*—The test statistic adopted for the purpose of this test is the time difference between the neutrino arrival and the maximum in the radio light curve of a blazar. For multiple blazars, the shortest time difference is taken. Here, only the global all-time maximum of each light curve is considered. This is a conservative choice: there is always one flare selected for each blazar and no minimum flux threshold. A corresponding benefit is that no free parameters need to be determined or set beforehand.

The full length of the available light curves, about 17 years ([Section A.1.2](#)), is used for the test statistic calculation. It is to be noted that this approach makes the test statistic values dependent on the length of the radio monitoring program: the earlier the starting date, the more chances for the all-time maximum to coincide with more extreme historical flares instead of more recent ones closer to the neutrino arrival. This effect fundamentally influences both the observed and simulated coincidences in the same way, ensuring that the analysis is valid. A similar approach using the all-time normalised activity index was used for the same sample of blazars in [Kouch et al. \(2024\)](#). A potential alternative would be restricting the radio light curves to the operation time frame of KM3NeT. Such a restriction would involve more design choices, such as the proper accounting for the time-varying exposure of the detector. For the purpose of this work, a simple approach most similar to earlier studies was chosen in light of the *a posteriori* nature of the analysis.

The calculation of this test statistic goes as follows:

- for a single blazar,  $TS_i$  = difference between the neutrino arrival time and the time of the maximum in the radio light curve;
- for multiple blazars,  $TS = \min(TS_i)$ , where the index  $i$  runs over all the blazars.

*Results*—The performed analysis yields the following results:

- Observed  $TS = 5$  days, for the blazar PMN J0606-0724 ([Figure 2](#));
- the null distribution from the simulation is shown in [Figure A5](#);
- a p-value of  $p = 0.26\%$  is obtained, indicating a 1 in 385 chance to observe a time difference of 5 days or less between the neutrino arrival time and the highest radio peak purely by random chance.

A discussion of the potential interpretation of this radio flare is given in [Section 5.2](#). It should be noted that this analysis is fundamentally *a posteriori* and not trial-free; in particular, it focuses solely on flares in the radio band. The band choice is not completely arbitrary, but these considerations make determining the proper correction factor for the chance probability challenging, and this correction is not attempted here.

## C. MULTIWAVELENGTH LIGHT CURVES

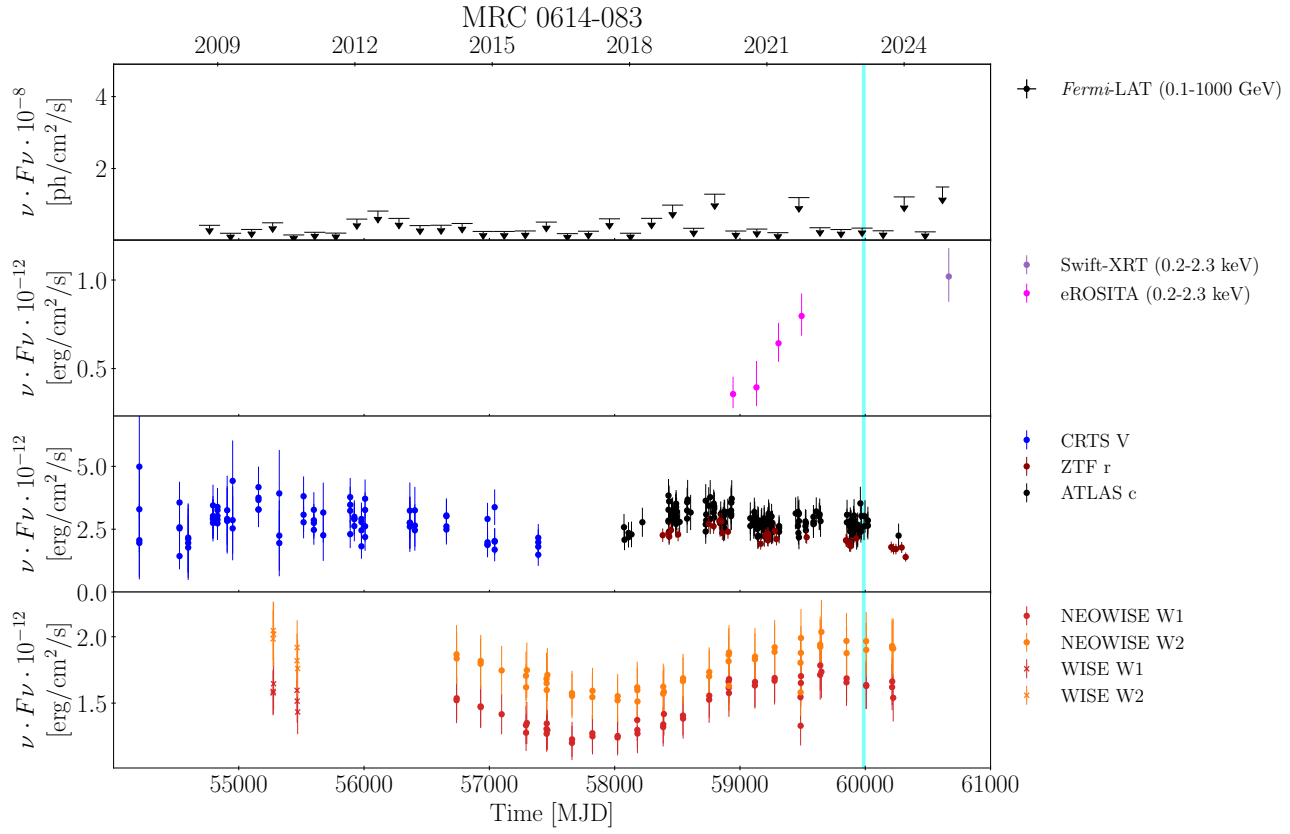


**Figure A6.** Multi-wavelength light curves of MRC 0614-083 (#1). The panels display from top to bottom: *Fermi*-LAT gamma-ray light curves integrated over a 6-months time bin; X-ray data from *Swift*-XRT and *eROSITA*; optical data from CRTS, ZTF and ATLAS; IR data from WISE/NEOWISE. The cyan stripe highlights the arrival time of KM3-230213A.

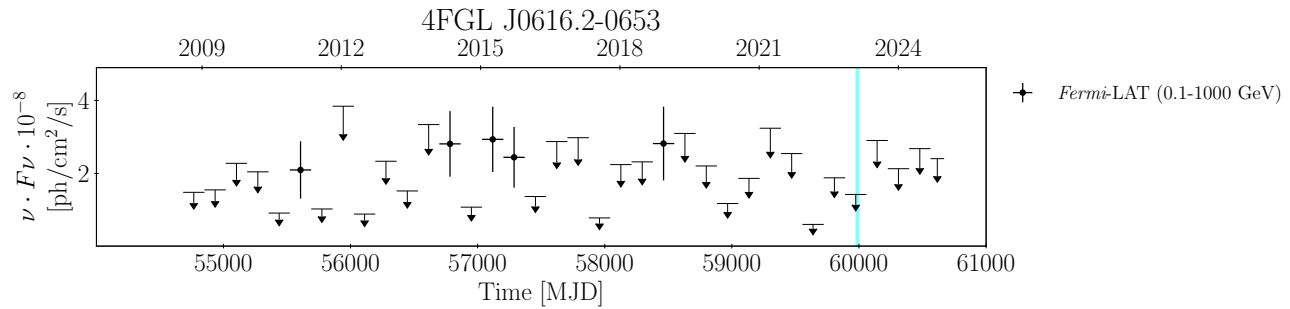


**Figure A7.** *Fermi*-LAT lightcurve of 4FGL J0616.2-0653 (#2), integrated over a 6-months time bin. The cyan stripe highlights the arrival time of KM3-230213A.

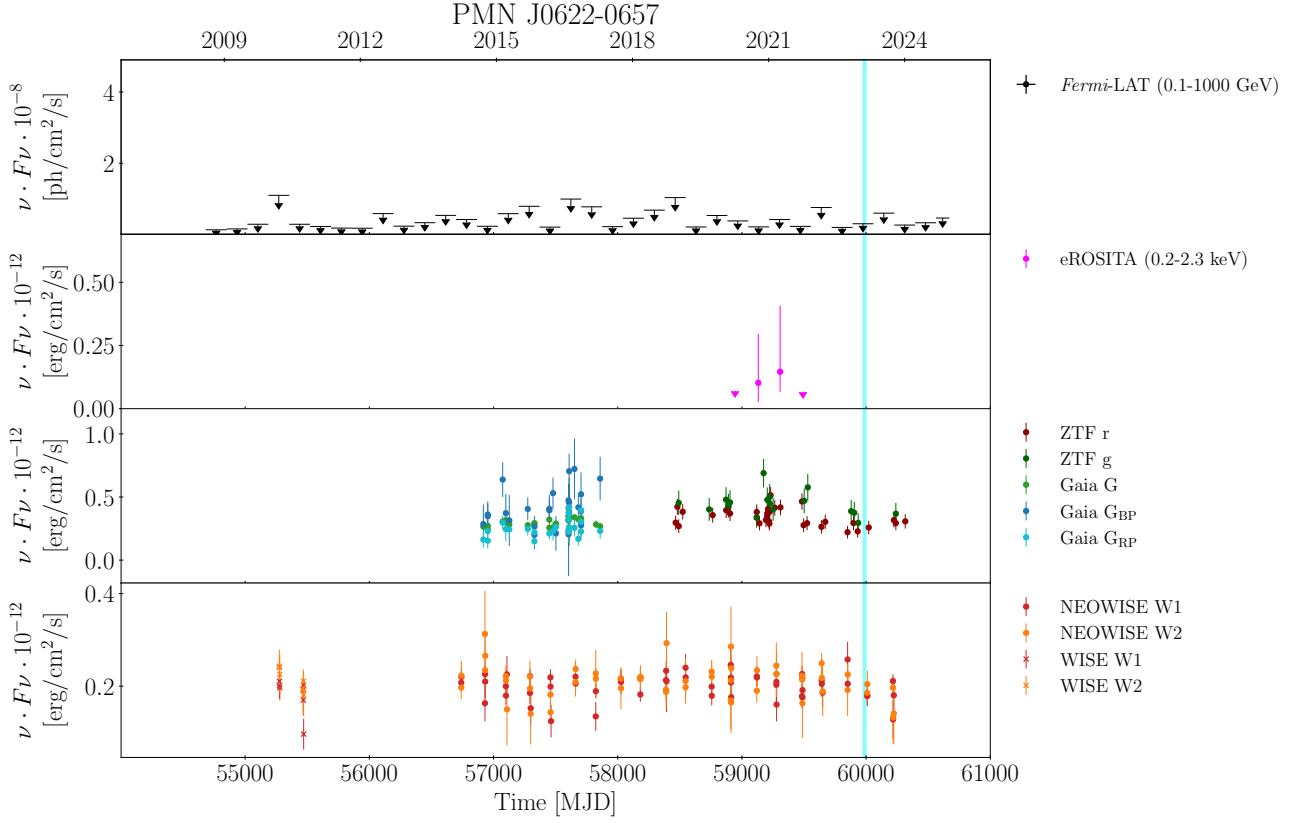


**Figure A8.** Multi-wavelength light curves of PMN J0622-0657 (#3). The panels display from top to bottom: *Fermi*-LAT gamma-ray light curves integrated over 6-months; X-ray data from *eROSITA*; optical data from ZTF and *Gaia*; IR data from WISE/NEOWISE. The cyan stripe highlights the arrival time of KM3-230213A.

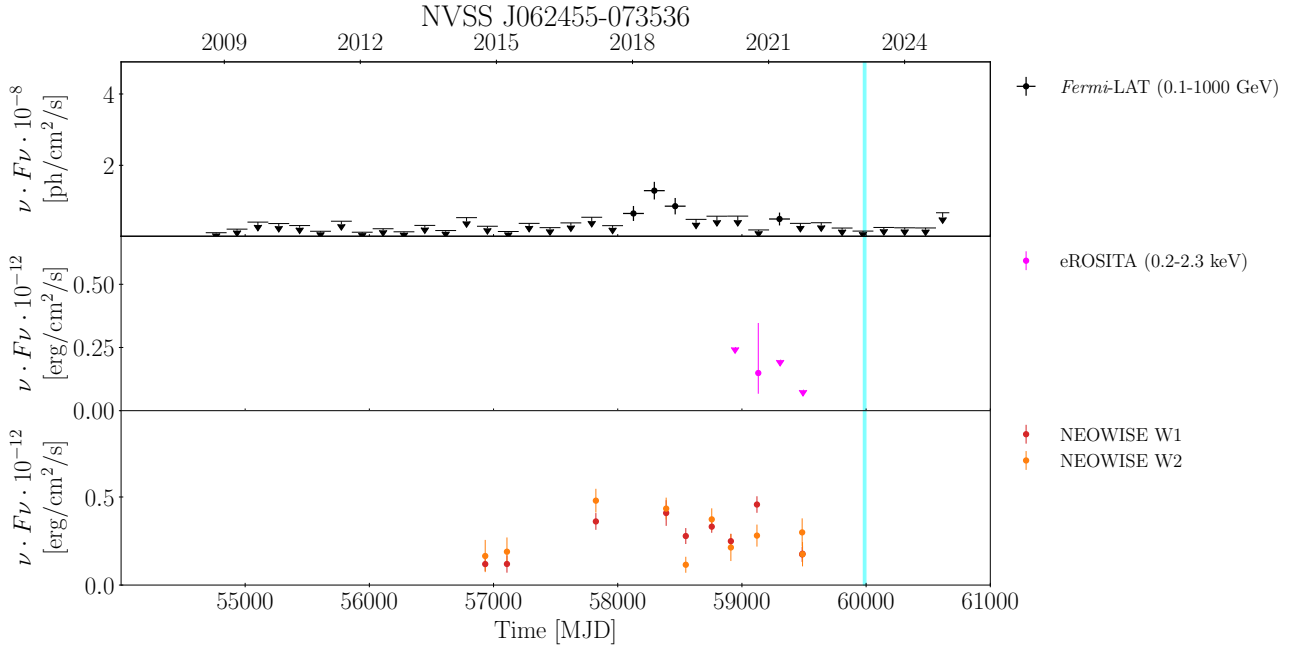


**Figure A9.** Multi-wavelength light curves of NVSS J062455-073536 (#4). The panels display from top to bottom: *Fermi*-LAT gamma-ray light curves integrated over 6-months; X-ray data from *eROSITA*; IR data from WISE/NEOWISE. The cyan stripe highlights the arrival time of KM3-230213A.

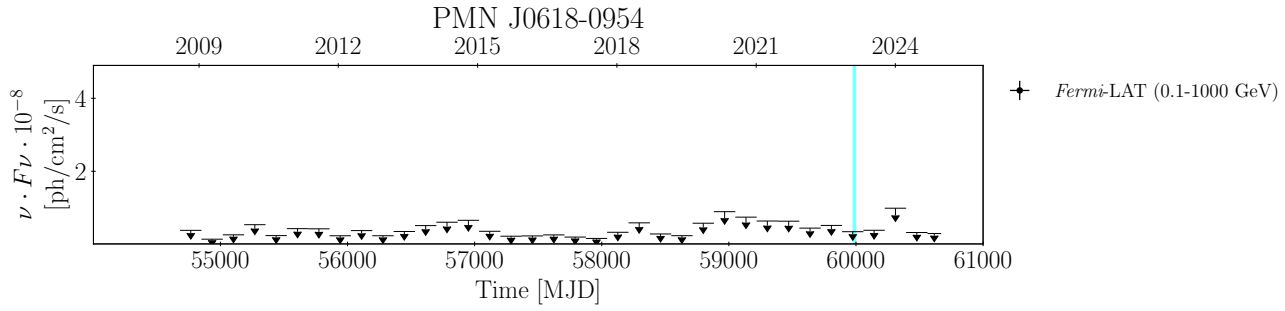


**Figure A10.** *Fermi*-LAT lightcurve of PMN J0618-0954 (#5), integrated over a 6-months time bin. The cyan stripe highlights the arrival time of KM3-230213A.

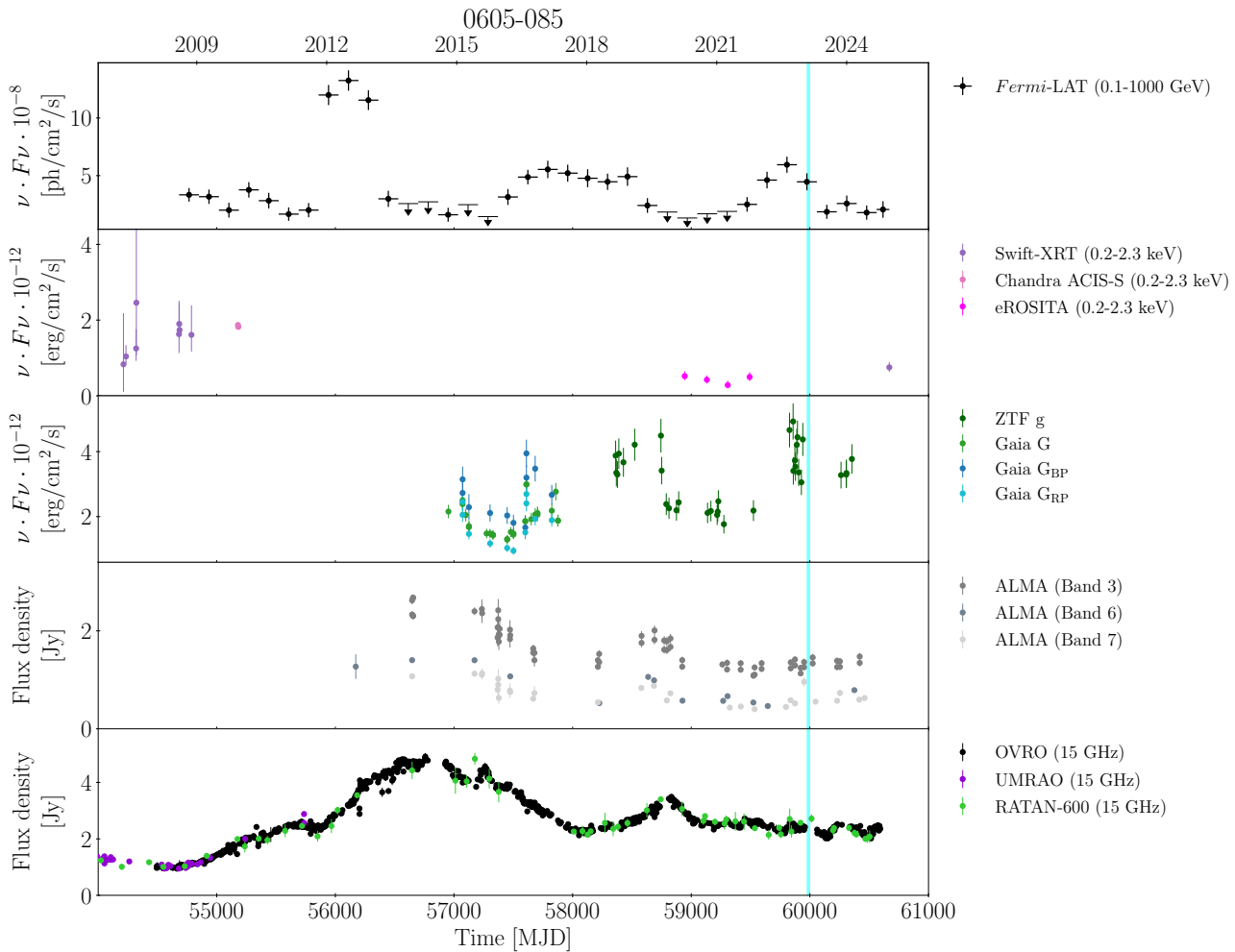


**Figure A11.** Multi-wavelength light curves of 0605-085 (#6). The panels display from top to bottom: *Fermi*-LAT gamma-ray light curves integrated over 6-months; X-ray data from *Swift*-XRT, *Chandra* and *eROSITA*; optical data from ZTF and *Gaia*; radio data from ALMA, OVRO, UMRAO and RATAN-600. The cyan stripe highlights the arrival time of KM3-230213A.



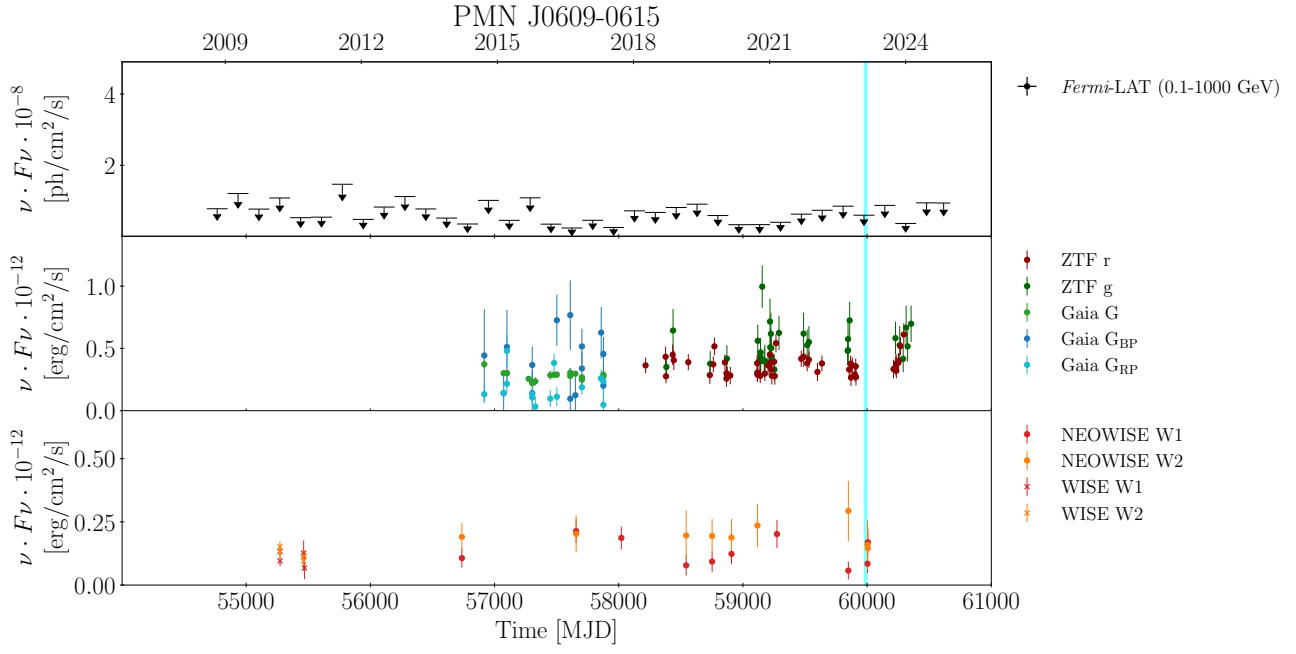


**Figure A12.** Multi-wavelength light curves of PMN J0609-0615 (#7). The panels display from top to bottom: *Fermi*-LAT gamma-ray light curves integrated over 6-months; optical data from ZTF and *Gaia*; IR data from WISE/NEOWISE. The cyan stripe highlights the arrival time of KM3-230213A.



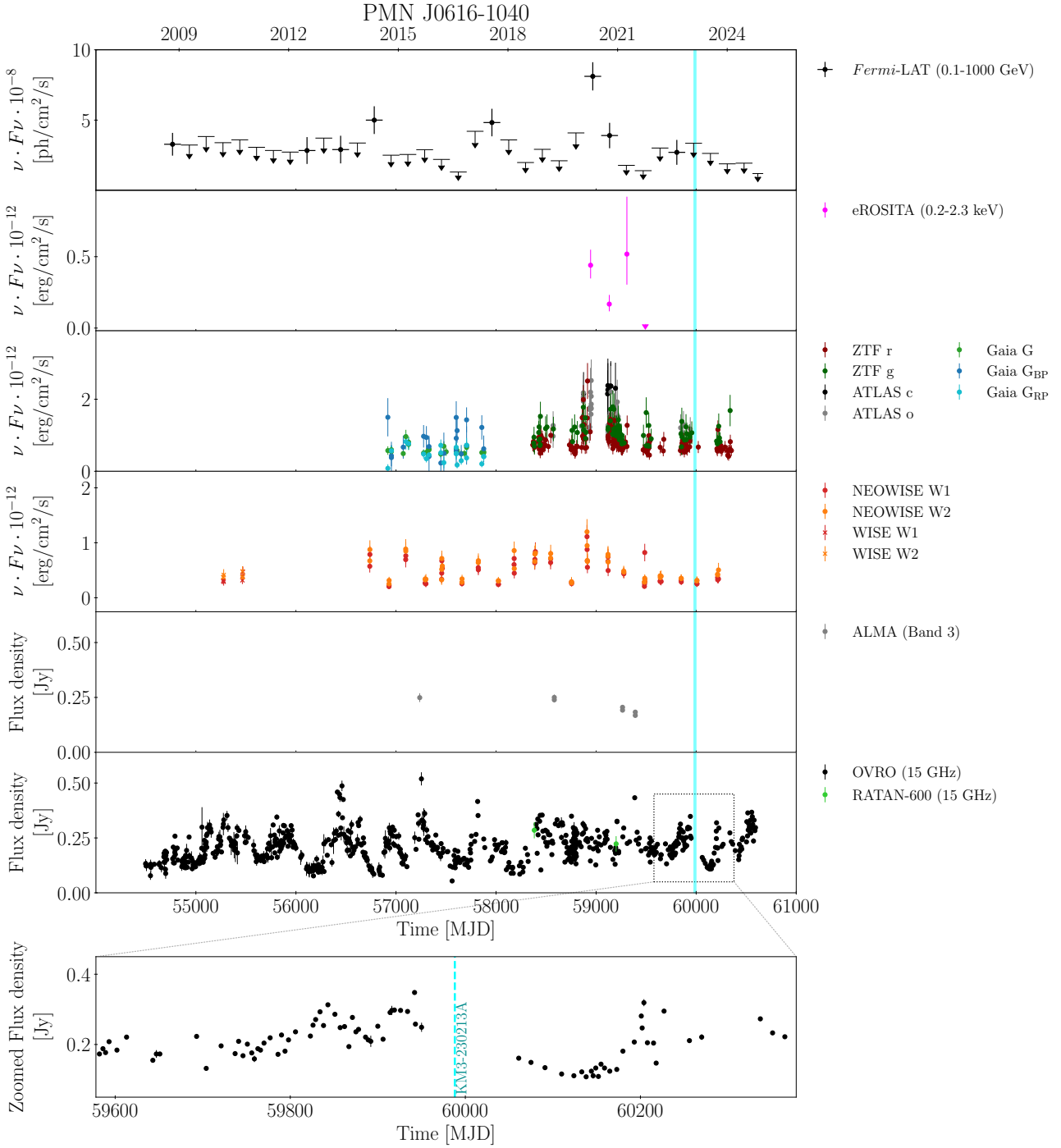


**Figure A14.** Multi-wavelength light curves of PMN J0616-1040 (#9). The panels display from top to bottom: *Fermi*-LAT gamma-ray light curves integrated over 6-months; X-ray data from *eROSITA*; optical data from ZTF, ATLAS and *Gaia*; IR data from WISE/NEOWISE; radio data from ALMA, OVRO and RATAN-600. The last panel displays the zoomed radio light curve centered on the neutrino arrival time. The cyan stripe highlights the arrival time of KM3-230213A.

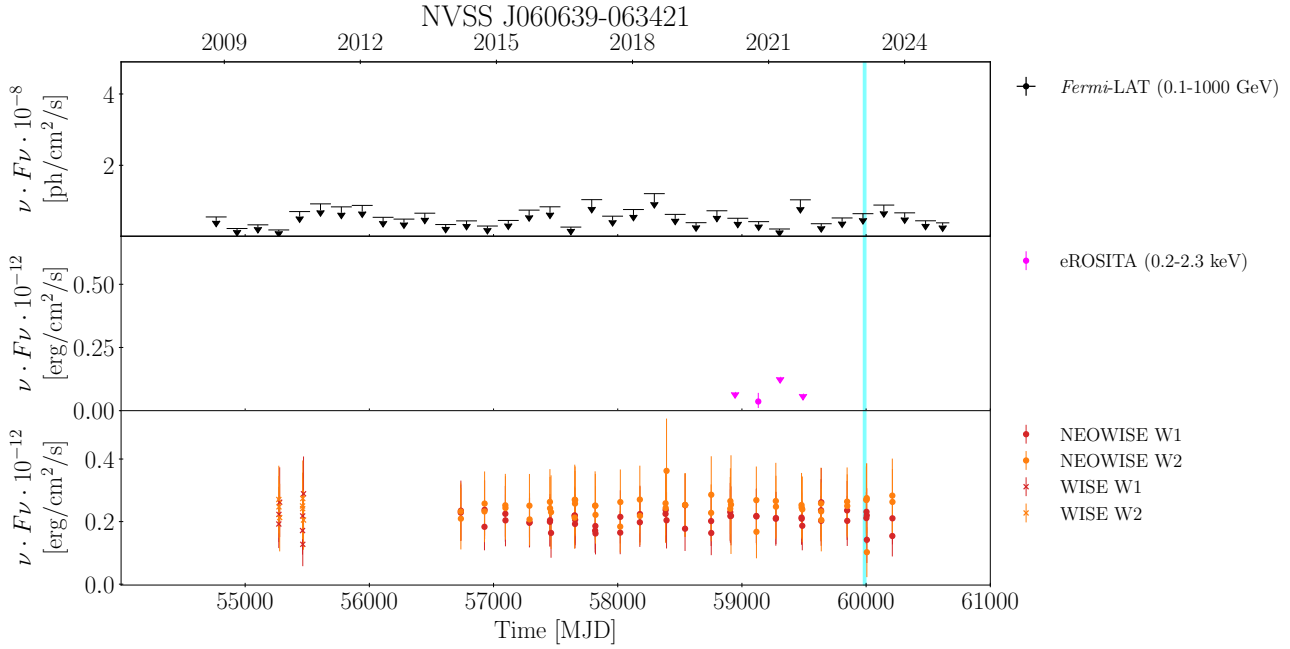


**Figure A15.** Multi-wavelength light curves of NVSS J060639-063421 (#10). The panels display from top to bottom: *Fermi*-LAT gamma-ray light curves integrated over 6-months; X-ray data from *eROSITA*; IR data from WISE/NEOWISE. The cyan stripe highlights the arrival time of KM3-230213A.

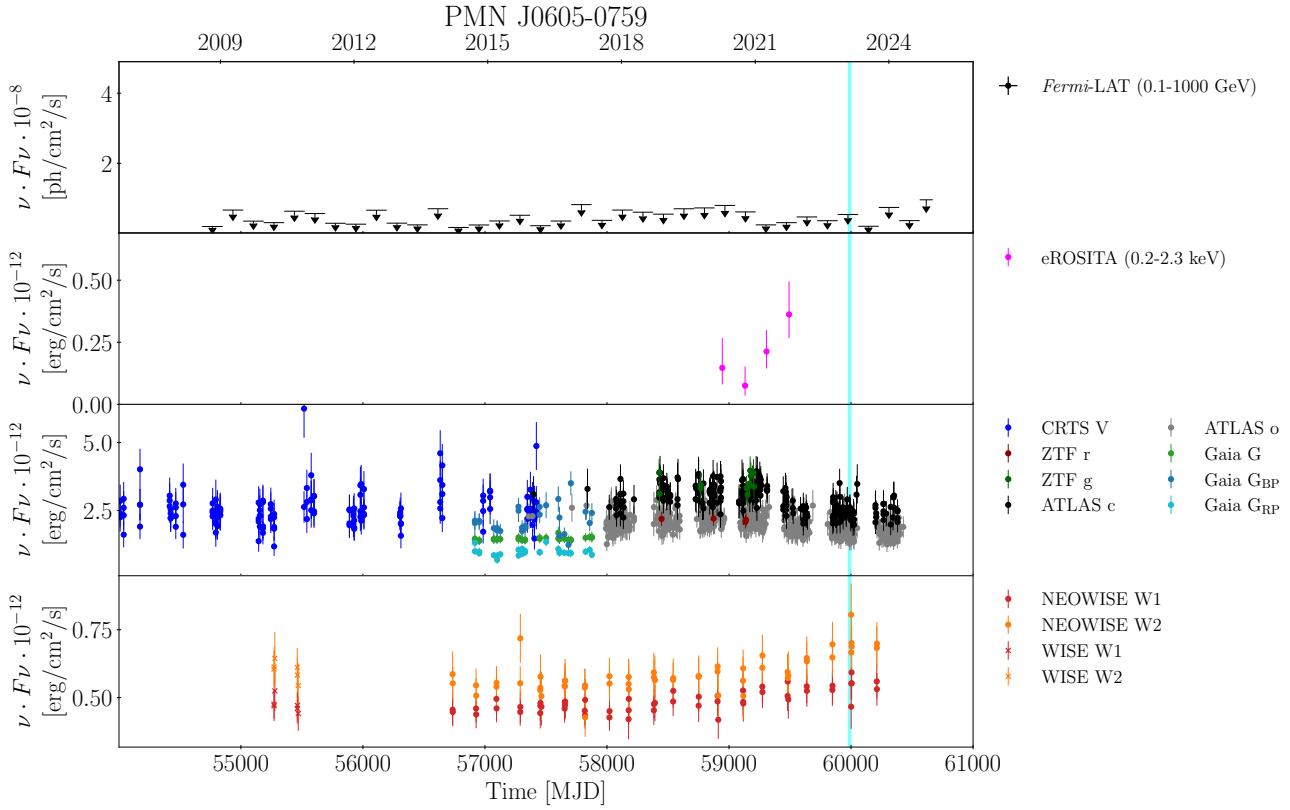


**Figure A16.** Multi-wavelength light curves of PMN J0605-0759 (#11). The panels display from top to bottom: *Fermi*-LAT gamma-ray light curves integrated over 6-months; X-ray data from *eROSITA*; optical data from CRTS, ZTF, ATLAS and *Gaia*; IR data from WISE/NEOWISE. The cyan stripe highlights the arrival time of KM3-230213A.

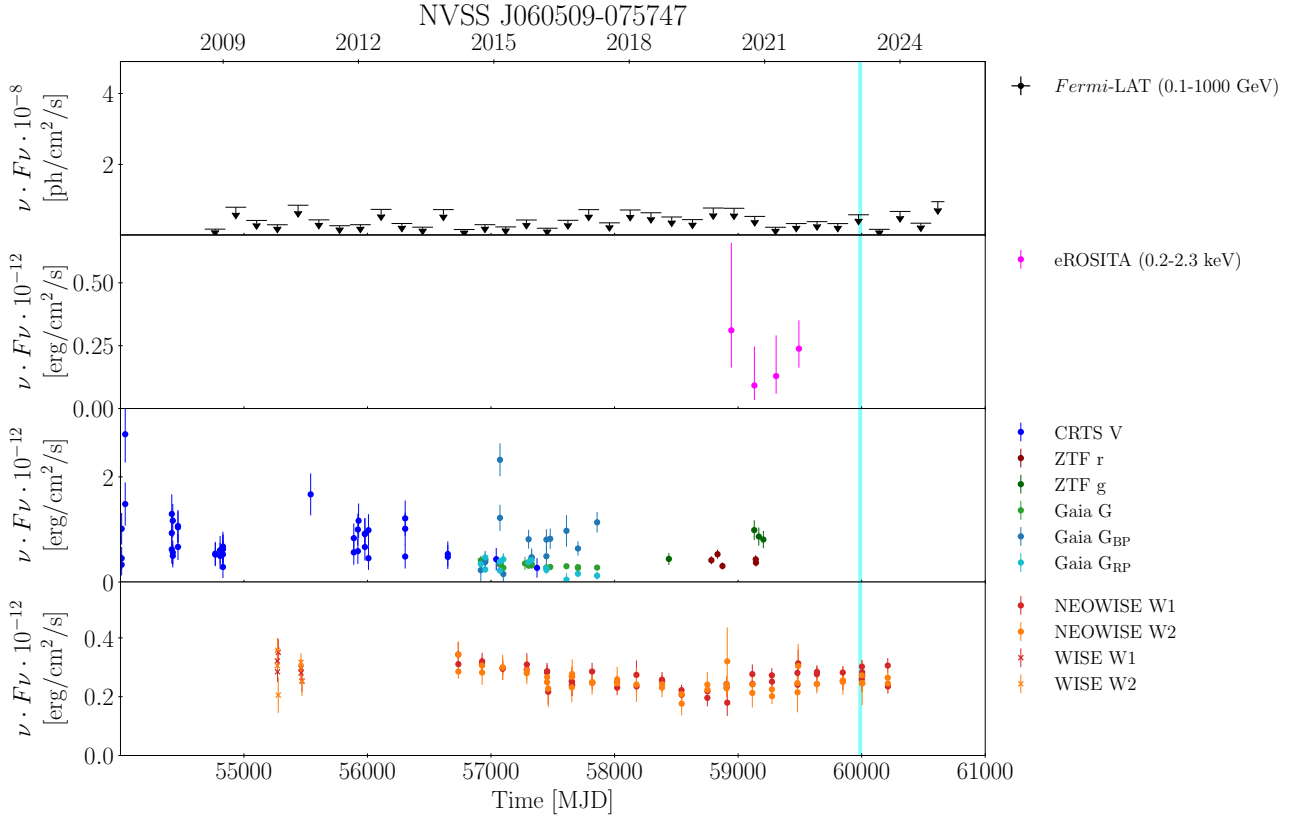


**Figure A17.** Multi-wavelength light curves of NVSS J060509-075747 (#12). The panels display from top to bottom: *Fermi*-LAT gamma-ray light curves integrated over 6-months; X-ray data from *eROSITA*; optical data from CRTS, ZTF and *Gaia*; IR data from WISE/NEOWISE. The cyan stripe highlights the arrival time of KM3-230213A.

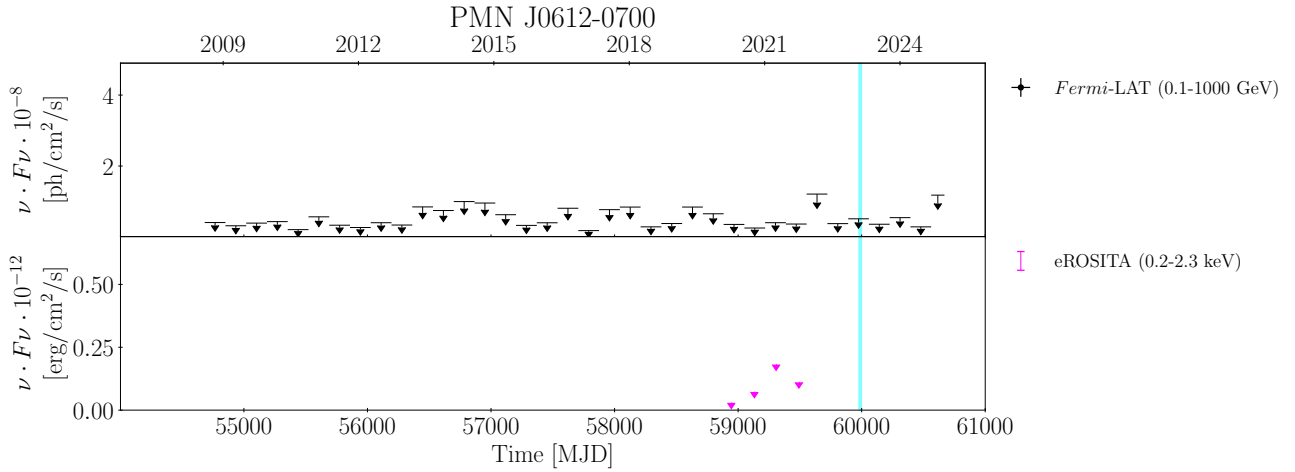


**Figure A18.** Multi-wavelength light curves of PMN J0612-0700 (#13). The panels display from top to bottom: *Fermi*-LAT gamma-ray light curves integrated over 6-months; X-ray data from *eROSITA*. The cyan stripe highlights the arrival time of KM3-230213A.



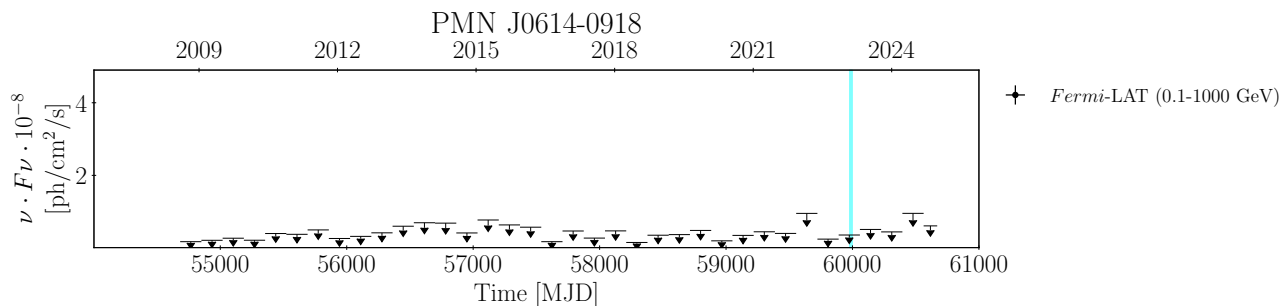


**Figure A19.** *Fermi*-LAT lightcurve of PMN J0614-0918 (#14), integrated over a 6-months time bin. The cyan stripe highlights the arrival time of KM3-230213A.

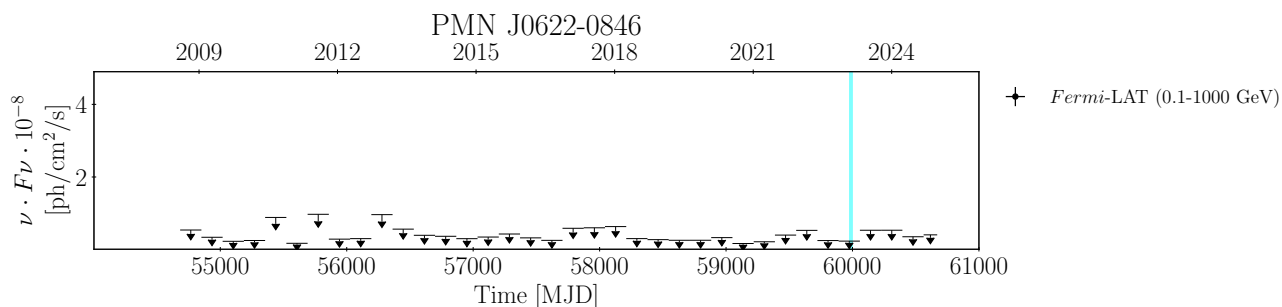


**Figure A20.** *Fermi*-LAT lightcurve of PMN J0622-0846 (#15), integrated over a 6-months time bin. The cyan stripe highlights the arrival time of KM3-230213A.

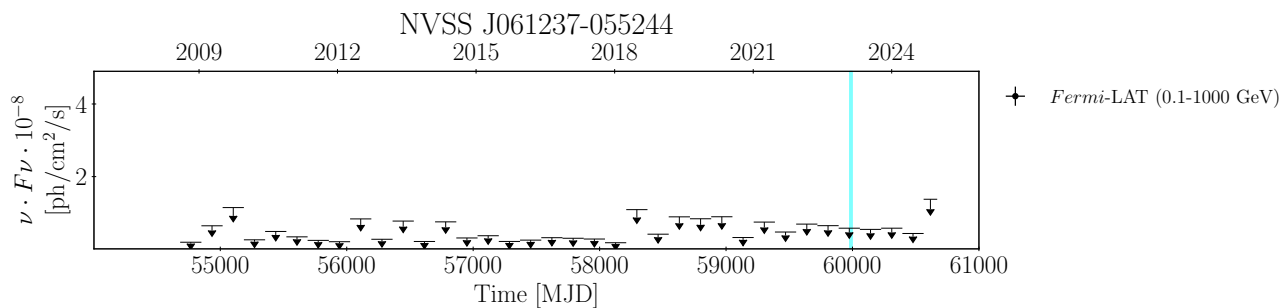


**Figure A21.** *Fermi*-LAT lightcurve of NVSS J061237-055244 (#16), integrated over a 6-months time bin. The cyan stripe highlights the arrival time of KM3-230213A.

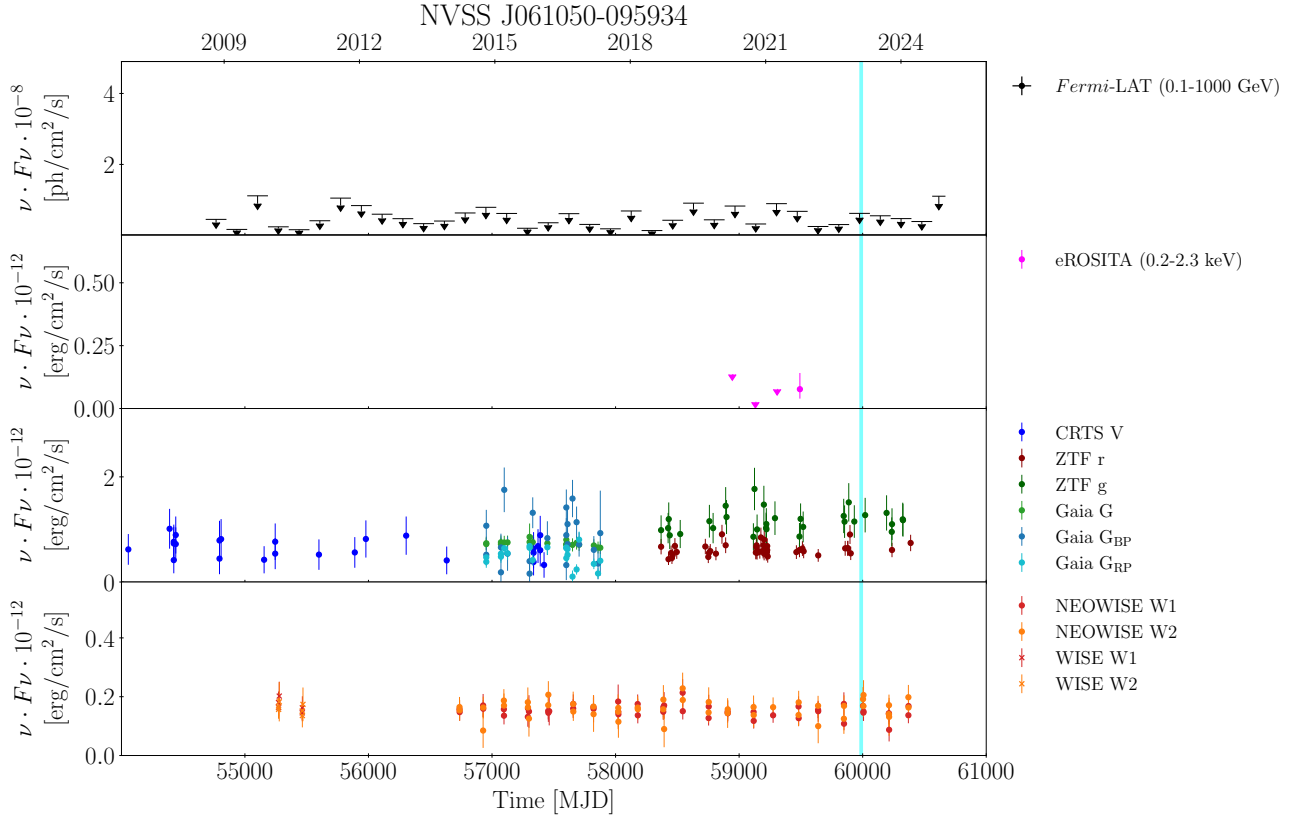


**Figure A22.** Multi-wavelength light curves of NVSS J061050-095934 (#17). The panels display from top to bottom: *Fermi*-LAT gamma-ray light curves integrated over 6-months; X-ray data from *eROSITA*; optical data from CRTS, ZTF and *Gaia*; IR data from WISE/NEOWISE. The cyan stripe highlights the arrival time of KM3-230213A.

## REFERENCES

- Aartsen, M. G., et al. 2018, *Science*, 361, 147, doi: [10.1126/science.aat2890](https://doi.org/10.1126/science.aat2890)
- Abbasi, R., Ackermann, M., Adams, J., et al. 2022, *ApJ*, 928, 50, doi: [10.3847/1538-4357/ac4d29](https://doi.org/10.3847/1538-4357/ac4d29)
- Abbasi, R., et al. 2023, *ApJ*, 954, 75, doi: [10.3847/1538-4357/acdfcb](https://doi.org/10.3847/1538-4357/acdfcb)
- Abbasi, R., Ackermann, M., Adams, J., et al. 2024, arXiv e-prints, arXiv:2406.06684, doi: [10.48550/arXiv.2406.06684](https://doi.org/10.48550/arXiv.2406.06684)
- Abdollahi, S., Acero, F., Ackermann, M., et al. 2020, *ApJS*, 247, 33, doi: [10.3847/1538-4365/ab6bcb](https://doi.org/10.3847/1538-4365/ab6bcb)
- Ackermann, M., Ajello, M., Allafort, A., et al. 2012, *ApJ*, 756, 4, doi: [10.1088/0004-637X/756/1/4](https://doi.org/10.1088/0004-637X/756/1/4)
- Adrian-Martinez, S., et al. 2016, *J. Phys. G*, 43, 084001, doi: [10.1088/0954-3899/43/8/084001](https://doi.org/10.1088/0954-3899/43/8/084001)
- Aiello, S., et al. 2022, *JINST*, 17, P07038, doi: [10.1088/1748-0221/17/07/P07038](https://doi.org/10.1088/1748-0221/17/07/P07038)
- . 2024, *Eur. Phys. J. C*, 84, 885, doi: [10.1140/epjc/s10052-024-13137-2](https://doi.org/10.1140/epjc/s10052-024-13137-2)
- . 2025, *Nature*, doi: [10.1038/s41586-024-08543-1](https://doi.org/10.1038/s41586-024-08543-1)
- Albert, A., Alves, S., André, M., et al. 2024, *ApJ*, 964, 3, doi: [10.3847/1538-4357/ad1f5b](https://doi.org/10.3847/1538-4357/ad1f5b)
- Aliakberov, K. D., Mingaliev, M. G., Naugolnaya, M. N., et al. 1985, *Astrofizicheskie Issledovaniia Izvestiya Spetsial'noj Astrofizicheskoi Observatorii*, 19, 60
- Allakhverdyan, V. A., Avrorin, A. D., Avrorin, A. V., et al. 2024, *MNRAS*, 527, 8784, doi: [10.1093/mnras/stad3653](https://doi.org/10.1093/mnras/stad3653)
- Aller, H. D., Aller, M. F., Latimer, G. E., & Hodge, P. E. 1985, *ApJS*, 59, 513, doi: [10.1086/191083](https://doi.org/10.1086/191083)
- Aller, M. F., Hughes, P. A., Aller, H. D., Latimer, G. E., & Hovatta, T. 2014, *The Astrophysical Journal*, 791, 53, doi: [10.1088/0004-637X/791/1/53](https://doi.org/10.1088/0004-637X/791/1/53)
- Atwood, W., Albert, A., Baldini, L., et al. 2013, arXiv e-prints, arXiv:1303.3514, <https://arxiv.org/abs/1303.3514>
- Atwood, W. B., et al. 2009, *ApJ*, 697, 1071, doi: [10.1088/0004-637X/697/2/1071](https://doi.org/10.1088/0004-637X/697/2/1071)
- Baars, J. W. M., Genzel, R., Pauliny-Toth, I. I. K., & Witzel, A. 1977, *A&A*, 500, 135
- Babusiaux, C., Fabricius, C., Khanna, S., et al. 2023, *A&A*, 674, A32, doi: [10.1051/0004-6361/202243790](https://doi.org/10.1051/0004-6361/202243790)
- Ballet, J., Bruel, P., Burnett, T. H., Lott, B., & The Fermi-LAT collaboration. 2023, arXiv e-prints, arXiv:2307.12546, doi: [10.48550/arXiv.2307.12546](https://doi.org/10.48550/arXiv.2307.12546)
- Bellenghi, C., Padovani, P., Resconi, E., & Giommi, P. 2023, *ApJL*, 955, L32, doi: [10.3847/2041-8213/acf711](https://doi.org/10.3847/2041-8213/acf711)
- Berezinsky, V. S., & Zatsepin, G. T. 1969, *Phys. Lett. B*, 28, 423, doi: [10.1016/0370-2693\(69\)90341-4](https://doi.org/10.1016/0370-2693(69)90341-4)
- Bird, D. J., Corbato, S. C., Dai, H. Y., et al. 1995, *ApJ*, 441, 144, doi: [10.1086/175344](https://doi.org/10.1086/175344)
- Blackburn, J. K. 1995, in *Astronomical Society of the Pacific Conference Series*, Vol. 77, *Astronomical Data Analysis Software and Systems IV*, ed. R. A. Shaw, H. E. Payne, & J. J. E. Hayes, 367
- Blandford, R., Meier, D., & Readhead, A. 2019, *ARA&A*, 57, 467, doi: [10.1146/annurev-astro-081817-051948](https://doi.org/10.1146/annurev-astro-081817-051948)
- Blandford, R. D. 2000, *Physica Scripta Volume T*, 85, 191, doi: [10.1238/Physica.Topical.085a00191](https://doi.org/10.1238/Physica.Topical.085a00191)
- Boller, T., Freyberg, M. J., Trümper, J., et al. 2016, *A&A*, 588, A103, doi: [10.1051/0004-6361/201525648](https://doi.org/10.1051/0004-6361/201525648)
- Böttcher, M. 2019, *Galaxies*, 7, 20, doi: [10.3390/galaxies7010020](https://doi.org/10.3390/galaxies7010020)
- Bruel, P., Burnett, T. H., Digel, S. W., et al. 2018, arXiv e-prints, arXiv:1810.11394, <https://arxiv.org/abs/1810.11394>
- Buchner, J. 2019, *PASP*, 131, 108005, doi: [10.1088/1538-3873/aae7fc](https://doi.org/10.1088/1538-3873/aae7fc)
- . 2021, *The Journal of Open Source Software*, 6, 3001, doi: [10.21105/joss.03001](https://doi.org/10.21105/joss.03001)
- Buchner, J., Georgakakis, A., Nandra, K., et al. 2014, *A&A*, 564, A125, doi: [10.1051/0004-6361/201322971](https://doi.org/10.1051/0004-6361/201322971)
- Burrows, D. N., Hill, J. E., Nousek, J. A., et al. 2005, *SSRv*, 120, 165, doi: [10.1007/s11214-005-5097-2](https://doi.org/10.1007/s11214-005-5097-2)
- Buson, S., Tramacere, A., Pfeiffer, L., et al. 2022, *ApJL*, 934, L38, doi: [10.3847/2041-8213/ac83a2](https://doi.org/10.3847/2041-8213/ac83a2)
- Buson, S., et al. 2022, *ApJL*, 933, L43, doi: [10.3847/2041-8213/ac7d5b](https://doi.org/10.3847/2041-8213/ac7d5b)
- Buson, S., Tramacere, A., Oswald, L., et al. 2023, <https://arxiv.org/abs/2305.11263>
- Casandjian, J. M., & Grenier, I. A. 2008, *A&A*, 489, 849, doi: [10.1051/0004-6361:200809685](https://doi.org/10.1051/0004-6361:200809685)
- Cash, W. 1979, *ApJ*, 228, 939, doi: [10.1086/156922](https://doi.org/10.1086/156922)
- Chlebowski, T., Hughes, J. P., & Siemiginowska, A. 1991, *Postepy Astronomii Krakow*, 39, 15
- Condon, J. J., Cotton, W. D., Greisen, E. W., et al. 1998, *AJ*, 115, 1693, doi: [10.1086/300337](https://doi.org/10.1086/300337)
- Cutri, R. M., Wright, E. L., Conrow, T., et al. 2021, *VizieR Online Data Catalog: AllWISE Data Release (Cutri+2013)*, *VizieR On-line Data Catalog: II/328*. Originally published in: *IPAC/Caltech (2013)*
- D'Abrusco, R., Massaro, F., Paggi, A., et al. 2014, *Astrophys. J. Suppl.*, 215, 14, doi: [10.1088/0067-0049/215/1/14](https://doi.org/10.1088/0067-0049/215/1/14)
- Das, S., Razzaque, S., & Gupta, N. 2022, *A&A*, 658, L6, doi: [10.1051/0004-6361/202142123](https://doi.org/10.1051/0004-6361/202142123)
- Deller, A. T., Brisken, W. F., Phillips, C. J., et al. 2011, *PASP*, 123, 275, doi: [10.1086/658907](https://doi.org/10.1086/658907)

- Dey, A., et al. 2019, *Astron. J.*, 157, 168, doi: [10.3847/1538-3881/ab089d](https://doi.org/10.3847/1538-3881/ab089d)
- Drake, A. J., Djorgovski, S. G., Mahabal, A., et al. 2009, *ApJ*, 696, 870, doi: [10.1088/0004-637X/696/1/870](https://doi.org/10.1088/0004-637X/696/1/870)
- Fan, X., Zou, G., Wei, J., et al. 2020, in *Society of Photo-Optical Instrumentation Engineers (SPIE) Conference Series*, Vol. 11443, *Space Telescopes and Instrumentation 2020: Optical, Infrared, and Millimeter Wave*, ed. M. Lystrup & M. D. Perrin, 114430Q, doi: [10.1117/12.2561854](https://doi.org/10.1117/12.2561854)
- Fichet de Clairfontaine, G., Buson, S., Pfeiffer, L., et al. 2023, *ApJL*, 958, L2, doi: [10.3847/2041-8213/ad0644](https://doi.org/10.3847/2041-8213/ad0644)
- Fitzpatrick, E. L. 1999, *PASP*, 111, 63, doi: [10.1086/316293](https://doi.org/10.1086/316293)
- Franckowiak, A., et al. 2020, *ApJ*, 893, 162, doi: [10.3847/1538-4357/ab8307](https://doi.org/10.3847/1538-4357/ab8307)
- Fruscione, A., McDowell, J. C., Allen, G. E., et al. 2006, in *Society of Photo-Optical Instrumentation Engineers (SPIE) Conference Series*, Vol. 6270, *Observatory Operations: Strategies, Processes, and Systems*, ed. D. R. Silva & R. E. Doxsey, 62701V, doi: [10.1117/12.671760](https://doi.org/10.1117/12.671760)
- Gaia Collaboration, Prusti, T., de Bruijne, J. H. J., et al. 2016, *A&A*, 595, A1, doi: [10.1051/0004-6361/201629272](https://doi.org/10.1051/0004-6361/201629272)
- Gaia Collaboration, Vallenari, A., Brown, A. G. A., et al. 2023, *A&A*, 674, A1, doi: [10.1051/0004-6361/202243940](https://doi.org/10.1051/0004-6361/202243940)
- Garrappa, S., et al. 2019, *ApJ*, 880, 880:103, doi: [10.3847/1538-4357/ab2ada](https://doi.org/10.3847/1538-4357/ab2ada)
- Garrappa, S., Buson, S., Sinapius, J., et al. 2024, *A&A*, 687, A59, doi: [10.1051/0004-6361/202449221](https://doi.org/10.1051/0004-6361/202449221)
- Gehrels, N., Chincarini, G., Giommi, P., et al. 2004, *ApJ*, 611, 1005, doi: [10.1086/422091](https://doi.org/10.1086/422091)
- Giommi, P., Glauch, T., Padovani, P., et al. 2020, *MNRAS*, 497, 865, doi: [10.1093/mnras/staa2082](https://doi.org/10.1093/mnras/staa2082)
- Godet, O., Nasser, G., Atteia, J. ., et al. 2014, in *Society of Photo-Optical Instrumentation Engineers (SPIE) Conference Series*, Vol. 9144, *Space Telescopes and Instrumentation 2014: Ultraviolet to Gamma Ray*, ed. T. Takahashi, J.-W. A. den Herder, & M. Bautz, 914424, doi: [10.1117/12.2055507](https://doi.org/10.1117/12.2055507)
- Götz, D., Boutelier, M., Burwitz, V., et al. 2023, *Experimental Astronomy*, 55, 487, doi: [10.1007/s10686-022-09881-6](https://doi.org/10.1007/s10686-022-09881-6)
- Greisen, E. W. 2003, in *Astrophysics and Space Science Library*, Vol. 285, *Information Handling in Astronomy - Historical Vistas*, ed. A. Heck, 109, doi: [10.1007/0-306-48080-8\\_7](https://doi.org/10.1007/0-306-48080-8_7)
- Hartman, R. C., Bertsch, D. L., Bloom, S. D., et al. 1999, *ApJS*, 123, 79, doi: [10.1086/313231](https://doi.org/10.1086/313231)
- Healey, S. E., Romani, R. W., Cotter, G., et al. 2008, *ApJS*, 175, 97, doi: [10.1086/523302](https://doi.org/10.1086/523302)
- Heinze, A. N., Tonry, J. L., Denneau, L., et al. 2018, *AJ*, 156, 241, doi: [10.3847/1538-3881/aae47f](https://doi.org/10.3847/1538-3881/aae47f)
- HI4PI Collaboration, Ben Bekhti, N., Flöer, L., et al. 2016, *A&A*, 594, A116, doi: [10.1051/0004-6361/201629178](https://doi.org/10.1051/0004-6361/201629178)
- Hovatta, T., & Lindfors, E. 2019, *New Astron. Rev.*, 87, 101541, doi: [10.1016/j.newar.2020.101541](https://doi.org/10.1016/j.newar.2020.101541)
- Hovatta, T., Lindfors, E., Kiehlmann, S., et al. 2021, *A&A*, 650, A83, doi: [10.1051/0004-6361/202039481](https://doi.org/10.1051/0004-6361/202039481)
- Janssen, M., Goddi, C., van Bemmell, I. M., et al. 2019, arXiv e-prints, arXiv:1902.01749, doi: [10.48550/arXiv.1902.01749](https://doi.org/10.48550/arXiv.1902.01749)
- Jarrett, T. H., Cohen, M., Masci, F., et al. 2011, *ApJ*, 735, 112, doi: [10.1088/0004-637X/735/2/112](https://doi.org/10.1088/0004-637X/735/2/112)
- Jormanainen, J., Hovatta, T., Christie, I. M., et al. 2023, *A&A*, 678, A140, doi: [10.1051/0004-6361/202346286](https://doi.org/10.1051/0004-6361/202346286)
- Koay, J. Y., Jauncey, D. L., Hovatta, T., et al. 2019, *MNRAS*, 489, 5365, doi: [10.1093/mnras/stz2488](https://doi.org/10.1093/mnras/stz2488)
- Kouch, P. M., Lindfors, E., Hovatta, T., et al. 2024, arXiv e-prints, arXiv:2407.07153, doi: [10.48550/arXiv.2407.07153](https://doi.org/10.48550/arXiv.2407.07153)
- Kovalev, Y. Y., Nizhelsky, N. A., Kovalev, Y. A., et al. 1999, *A&AS*, 139, 545, doi: [10.1051/aas:1999406](https://doi.org/10.1051/aas:1999406)
- Kraft, R. P., Burrows, D. N., & Nousek, J. A. 1991, *ApJ*, 374, 344, doi: [10.1086/170124](https://doi.org/10.1086/170124)
- Krauß, F., et al. 2014, *A&A*, 566, L7, doi: [10.1051/0004-6361/201424219](https://doi.org/10.1051/0004-6361/201424219)
- Kun, E., Bartos, I., Tjus, J. B., et al. 2024, *PhRvD*, 110, 123014, doi: [10.1103/PhysRevD.110.123014](https://doi.org/10.1103/PhysRevD.110.123014)
- Lacy, M., Baum, S. A., Chandler, C. J., et al. 2020, *PASP*, 132, 035001, doi: [10.1088/1538-3873/ab63eb](https://doi.org/10.1088/1538-3873/ab63eb)
- Lister, M. L., Aller, M. F., Aller, H. D., et al. 2018, *ApJS*, 234, 12, doi: [10.3847/1538-4365/aa9c44](https://doi.org/10.3847/1538-4365/aa9c44)
- Lister, M. L., Homan, D. C., Hovatta, T., et al. 2019, *ApJ*, 874, 43, doi: [10.3847/1538-4357/ab08ee](https://doi.org/10.3847/1538-4357/ab08ee)
- Mainzer, A., Bauer, J., Grav, T., et al. 2011, *ApJ*, 731, 53, doi: [10.1088/0004-637X/731/1/53](https://doi.org/10.1088/0004-637X/731/1/53)
- Mannheim, K., & Biermann, P. L. 1989, *A&A*, 221, 211
- Mannheim, K., Stanev, T., & Biermann, P. L. 1992, *A&A*, 260, L1
- Masci, F. J., Laher, R. R., Rusholme, B., et al. 2018, *PASP*, 131, 018003, doi: [10.1088/1538-3873/aae8ac](https://doi.org/10.1088/1538-3873/aae8ac)
- Massaro, E., Maselli, A., Leto, C., et al. 2015, *Ap&SS*, 357, 75, doi: [10.1007/s10509-015-2254-2](https://doi.org/10.1007/s10509-015-2254-2)
- Massaro, F., D'Abrusco, R., Tosti, G., et al. 2012, *ApJ*, 750, 138, doi: [10.1088/0004-637X/750/2/138](https://doi.org/10.1088/0004-637X/750/2/138)
- Mattox, J. R., Bertsch, D. L., Chiang, J., et al. 1996, *ApJ*, 461, 396, doi: [10.1086/177068](https://doi.org/10.1086/177068)
- Merloni, A., Lamer, G., Liu, T., et al. 2024, *A&A*, 682, A34, doi: [10.1051/0004-6361/202347165](https://doi.org/10.1051/0004-6361/202347165)

- Ott, M., Witzel, A., Quirrenbach, A., et al. 1994, *A&A*, 284, 331
- Padovani, P., Oikonomou, F., Petropoulou, M., Giommi, P., & Resconi, E. 2019, *MNRAS*, 484, L104, doi: [10.1093/mnras/slz011](https://doi.org/10.1093/mnras/slz011)
- Paliya, V. S., Böttcher, M., Olmo-García, A., et al. 2020, *ApJ*, 902, 29, doi: [10.3847/1538-4357/abb46e](https://doi.org/10.3847/1538-4357/abb46e)
- Parijskij, Y. N. 1993, *IEEE Antennas and Propagation Magazine*, 35, 7, doi: [10.1109/74.229840](https://doi.org/10.1109/74.229840)
- Pearson, T. J., & Readhead, A. C. S. 1984, *ARA&A*, 22, 97, doi: [10.1146/annurev.aa.22.090184.000525](https://doi.org/10.1146/annurev.aa.22.090184.000525)
- Perley, R. A., & Butler, B. J. 2013, *ApJS*, 204, 19, doi: [10.1088/0067-0049/204/2/19](https://doi.org/10.1088/0067-0049/204/2/19)
- 2017, *ApJS*, 230, 7, doi: [10.3847/1538-4365/aa6df9](https://doi.org/10.3847/1538-4365/aa6df9)
- Petropoulou, M., et al. 2020, *ApJ*, 891, 115, doi: [10.3847/1538-4357/ab76d0](https://doi.org/10.3847/1538-4357/ab76d0)
- Petrov, L., Kovalev, Y. Y., Fomalont, E. B., & Gordon, D. 2011, *AJ*, 142, 35, doi: [10.1088/0004-6256/142/2/35](https://doi.org/10.1088/0004-6256/142/2/35)
- Petrov, L. Y., & Kovalev, Y. Y. 2025, *ApJS*, 276, 38, doi: [10.3847/1538-4365/ad8c36](https://doi.org/10.3847/1538-4365/ad8c36)
- Plavin, A., Kovalev, Y. Y., Kovalev, Y. A., & Troitsky, S. 2020, *ApJ*, 894, 101, doi: [10.3847/1538-4357/ab86bd](https://doi.org/10.3847/1538-4357/ab86bd)
- Plavin, A. V., Burenin, R. A., Kovalev, Y. Y., et al. 2024, *JCAP*, 2024, 133, doi: [10.1088/1475-7516/2024/05/133](https://doi.org/10.1088/1475-7516/2024/05/133)
- Plavin, A. V., Kovalev, Y. Y., Kovalev, Y. A., & Troitsky, S. V. 2023, *MNRAS*, 523, 1799, doi: [10.1093/mnras/stad1467](https://doi.org/10.1093/mnras/stad1467)
- Popkov, A. V., Kovalev, Y. Y., Petrov, L. Y., & Kovalev, Y. A. 2021, *AJ*, 161, 88, doi: [10.3847/1538-3881/abd18c](https://doi.org/10.3847/1538-3881/abd18c)
- Predehl, P., Andritschke, R., Arefiev, V., et al. 2021, *A&A*, 647, A1, doi: [10.1051/0004-6361/202039313](https://doi.org/10.1051/0004-6361/202039313)
- Readhead, A. C. S., Lawrence, C. R., Myers, S. T., et al. 1989, *ApJ*, 346, 566, doi: [10.1086/168039](https://doi.org/10.1086/168039)
- Richards, J. L., Max-Moerbeck, W., Pavlidou, V., et al. 2011, *ApJS*, 194, 29, doi: [10.1088/0067-0049/194/2/29](https://doi.org/10.1088/0067-0049/194/2/29)
- Riello, M., De Angeli, F., Evans, D. W., et al. 2021, *A&A*, 649, A3, doi: [10.1051/0004-6361/202039587](https://doi.org/10.1051/0004-6361/202039587)
- Rodrigo, C., & Solano, E. 2020, in *XIV.0 Scientific Meeting (virtual) of the Spanish Astronomical Society*, 182
- Rodrigo, C., Solano, E., & Bayo, A. 2012, *SVO Filter Profile Service Version 1.0, IVOA Working Draft 15* October 2012, doi: [10.5479/ADS/bib/2012ivoa.rept.1015R](https://doi.org/10.5479/ADS/bib/2012ivoa.rept.1015R)
- Roulet, E., & Vissani, F. 2021, *JCAP*, 2021, 050, doi: [10.1088/1475-7516/2021/03/050](https://doi.org/10.1088/1475-7516/2021/03/050)
- Salvato, M., Buchner, J., Budavari, T., et al. 2018, *MNRAS*, 473, 4937, doi: [10.1093/mnras/stx2651](https://doi.org/10.1093/mnras/stx2651)
- Salvato, M., et al. 2022, *A&A*, 661, A3, doi: [10.1051/0004-6361/202141631](https://doi.org/10.1051/0004-6361/202141631)
- Sanchez Zaballa, J. M., Buson, S., & et al. 2025, in prep.
- Schlafly, E. F., & Finkbeiner, D. P. 2011, *ApJ*, 737, 103, doi: [10.1088/0004-637X/737/2/103](https://doi.org/10.1088/0004-637X/737/2/103)
- Schmitt, J. H. M. M., Fleming, T. A., & Giampapa, M. S. 1995, *ApJ*, 450, 392, doi: [10.1086/176149](https://doi.org/10.1086/176149)
- Shaw, M. S., Romani, R. W., Cotter, G., et al. 2012, *ApJ*, 748, 49, doi: [10.1088/0004-637X/748/1/49](https://doi.org/10.1088/0004-637X/748/1/49)
- Shepherd, M. C. 1997, in *Astronomical Society of the Pacific Conference Series, Vol. 125, Astronomical Data Analysis Software and Systems VI*, ed. G. Hunt & H. Payne, 77
- Simmonds, C., Buchner, J., Salvato, M., Hsu, L. T., & Bauer, F. E. 2018, *A&A*, 618, A66, doi: [10.1051/0004-6361/201833412](https://doi.org/10.1051/0004-6361/201833412)
- Smith, K. W., Smartt, S. J., Young, D. R., et al. 2020, *PASP*, 132, 085002, doi: [10.1088/1538-3873/ab936e](https://doi.org/10.1088/1538-3873/ab936e)
- Sotnikova, Y. V. 2020, in *Ground-Based Astronomy in Russia. 21st Century*, ed. I. I. Romanyuk, I. A. Yakunin, A. F. Valeev, & D. O. Kudryavtsev, 32–40, doi: [10.26119/978-5-6045062-0-2\\_2020\\_32](https://doi.org/10.26119/978-5-6045062-0-2_2020_32)
- Spitzer Science Center (SSC), & Infrared Science Archive (IRSA). 2021, *VizieR Online Data Catalog: The Spitzer (SEIP) source list (SSTSL2)* (Spitzer Science Center, 2021), *VizieR On-line Data Catalog: II/368*. Originally published in: Spitzer Science Center (SSC), IRSA (2021)
- Sunyaev, R., Arefiev, V., Babushkin, V., et al. 2021, *A&A*, 656, A132, doi: [10.1051/0004-6361/202141179](https://doi.org/10.1051/0004-6361/202141179)
- Telescope Array Collaboration, Abbasi, R. U., Allen, M. G., et al. 2023, *Science*, 382, 903, doi: [10.1126/science.abo5095](https://doi.org/10.1126/science.abo5095)
- Tonry, J. L., Denneau, L., Heinze, A. N., et al. 2018, *PASP*, 130, 064505, doi: [10.1088/1538-3873/aabadf](https://doi.org/10.1088/1538-3873/aabadf)
- Tsybulev, P. G. 2011, *Astrophysical Bulletin*, 66, 109, doi: [10.1134/S199034131101010X](https://doi.org/10.1134/S199034131101010X)
- Tsybulev, P. G., Nizhelskii, N. A., Dugin, M. V., et al. 2018, *Astrophysical Bulletin*, 73, 494, doi: [10.1134/S1990341318040132](https://doi.org/10.1134/S1990341318040132)
- Tubín-Arenas, D., Krumpke, M., Lamer, G., et al. 2024, *A&A*, 682, A35, doi: [10.1051/0004-6361/202346773](https://doi.org/10.1051/0004-6361/202346773)
- Udovitskiy, R. Y., Sotnikova, Y. V., Mingaliev, M. G., et al. 2016, *Astrophysical Bulletin*, 71, 496, doi: [10.1134/S1990341316040131](https://doi.org/10.1134/S1990341316040131)
- Voges, W., Aschenbach, B., Boller, T., et al. 1999, *A&A*, 349, 389, doi: [10.48550/arXiv.astro-ph/9909315](https://doi.org/10.48550/arXiv.astro-ph/9909315)
- 2000, *IAUC*, 7432, 3
- Wei, J., Cordier, B., Antier, S., et al. 2016, *arXiv e-prints*, arXiv:1610.06892, doi: [10.48550/arXiv.1610.06892](https://doi.org/10.48550/arXiv.1610.06892)
- Weisskopf, M. C., Tananbaum, H. D., van Speybroeck, L. P., & O'Dell, S. L. 2000, *Proc. SPIE Int. Soc. Opt. Eng.*, 4012, 2, doi: [10.1117/12.391545](https://doi.org/10.1117/12.391545)



- White, N. E., Giommi, P., & Angelini, L. 2000, VizieR Online Data Catalog: The WGACAT version of ROSAT sources (White+ 2000), VizieR On-line Data Catalog: IX/31. Originally published in: Laboratory for High Energy Astrophysics (LHEA/NASA), Greenbelt (2000)
- Winter, W., Gao, S., Rodrigues, X., et al. 2020, PoS, ICRC2019, 1032, doi: [10.22323/1.358.1032](https://doi.org/10.22323/1.358.1032)
- Wood, M., Caputo, R., Charles, E., et al. 2017, in International Cosmic Ray Conference, Vol. 301, 35th International Cosmic Ray Conference (ICRC2017), 824, doi: [10.22323/1.301.0824](https://doi.org/10.22323/1.301.0824)
- Wright, E. L., Eisenhardt, P. R. M., Mainzer, A. K., et al. 2010, AJ, 140, 1868, doi: [10.1088/0004-6256/140/6/1868](https://doi.org/10.1088/0004-6256/140/6/1868)